An Insight Into Ancient Aeolian Processes and Post-Noachian Aqueous Alteration in Gale Crater, Mars, Using ChemCam Geochemical Data From the Greenheugh Capping Unit

Candice Bedford, Steven Banham, John Bridges, Olivier Forni, Agnes Cousin, Donald Bowden, Stuart Turner, Roger Wiens, Patrick Gasda, Jens Frydenvang, et al.

An insight into ancient aeolian processes and post-Noachian aqueous alteration in Gale crater, Mars, using ChemCam geochemical data from the Greenheugh capping unit.

Candice C. Bedford[1,2], Steven G. Banham[3], John C. Bridges[4], Olivier Forni[5], Agnes Cousin[5], Donald Bowden[4], Stuart M. R. Turner[6], Roger C. Wiens[7], Patrick J. Gasda[7], Jens Frydenvang[8], Olivier Gasnault[5], Kristin Rammelkamp[5], Frances Rivera-Hernandez[9], Elizabeth B. Rampe[2], Rebecca Smith[10], Cherie Achilles[11], Erwin Dehouck[12], Alexander B. Bryk[13], Susanne P. Schwenzer[6], Horton Newsom[14].

[1]Lunar and Planetary Institute, Universities Space Research Association, Houston, Texas, USA.

[2]Astromaterials Research and Exploration Science Division, NASA Johnson Space Center, Houston, Texas, USA.

[3]Imperial College, London, UK.

[4]University of Leicester, Leicester, UK.

[5]Institut de Recherche en Astrophysique et Planétologie, Université de Toulouse, UPS, CNRS, CNES, Toulouse, France.

[6]AstrobiologyOU, School of Environment, Earth and Ecosystem Sciences,, The Open University, Milton Keynes, UK.

[7]Los Alamos National Laboratory, New Mexico, USA.

[8]Globe Institute, University of Copenhagen, Denmark.

[9]Georgia Institute of Technology, Georgia, USA.

[10]Stony Brook University, New York, USA.

[11]NASA Goddard space flight center, Maryland, USA.

[12]Universite de Lyon, Lyon, France.

[13]University of Berkeley, California, USA.

[14]University of New Mexico, Albuquerque, New Mexico, USA.

Corresponding author: Candice C. Bedford (cbedford@lpi.usra.edu)

Key Points:

- ChemCam geochemical results support that the Greenheugh pediment capping unit was deposited within the Stimson sand sea in the Hesperian.
- The Greenheugh pediment capping unit was sourced from olivine-rich sands, potentially recycled from units farther up Mt Sharp.
- Greenheugh experienced less interaction with groundwaters than Stimson at the Emerson and Naukluft plateaus, but shared diagenesis at the unconformity.

Abstract

Aeolian processes have shaped and contributed to the geological record in Gale crater, Mars, long after the fluviolacustrine system existed ~3 Ga ago. Understanding these aeolian deposits, particularly those which have been lithified and show evidence for aqueous alteration, can help to constrain the environment at their time of deposition and the role of liquid water later in Mars' history. The NASA Curiosity rover investigated a prominent outcrop of aeolian sandstone within the Stimson formation at the Greenheugh pediment as part of its investigation of the Glen Torridon area. In this study, we use geochemical data from ChemCam to constrain the effects of aeolian sedimentary processes, sediment provenance, and diagenesis of the sandstone at the Greenheugh pediment, comparing the Greenheugh data to the results from previous Stimson localities situated 2.5 km north and >200 m lower in elevation. Our results, supported by mineralogical data from CheMin, show that the Stimson formation at the Greenheugh pediment was likely sourced from an olivine-rich unit that may be present farther up the slopes of Gale crater's central mound. Our results also suggest that the Greenheugh pediment Stimson formation was cemented by surface water runoff such as that which may have formed Gediz Vallis. The lack of alteration features in the Stimson formation at the Greenheugh pediment relative to those of the Emerson and Naukluft plateaus suggests that groundwater was not as available at this locality compared to the others. However, all sites share diagenesis at the unconformity.

Plain language summary

We use geochemical data from the Curiosity rover's ChemCam instrument to investigate the geological history of the Greenheugh pediment capping unit. The Greenheugh pediment is a geologic feature that has a gently sloping top, forming a broad plain extending from the base of the valley, Gediz Vallis. The Greenheugh pediment is capped by a unit of broadly uniform thickness which represents the remains of the Stimson dune field that existed <2.5 Ga (mid- to late-Hesperian). ChemCam geochemical data shows that the sands deposited at the Greenheugh capping unit were sourced from a nearby olivine-rich unit. Surface waters then cemented the windblown sand deposits, ponding at the unconformity with the underlying mudstone unit, creating concretions towards the base. Episodes of groundwater circulation did not affect the rocks at Greenheugh as much as they did at other Stimson localities with the exception of acid-sulfate alteration that occurred along the unconformity. These results suggest that the ancient Stimson dune field was a dynamic environment, incorporating grains from the surrounding geological units on Mt Sharp. Furthermore, liquid water was stable at the surface in the Hesperian and was available for multiple diagenetic events along bedrock weaknesses.

1 Introduction

Gale crater, where the NASA Mars Science Laboratory (MSL) Curiosity rover has been exploring since August, 2012, contains a diverse geological record which has been shaped by fluviolacustrine and later aeolian processes (Banham et al., 2021; Bridges et al., 2017; Edgar et al., 2020; Grotzinger et al., 2012, 2014, 2015; Hobbs et al., 2010; Stack et al., 2019; Thomson et al., 2011). After landing, the Curiosity rover traversed across the Bradbury plains to the foothills of Gale crater's central mound, Aeolis Mons (informally known as Mt Sharp). Along the traverse, the MSL mission has investigated poorly sorted conglomerates, cross-bedded sandstones, and thinly laminated mudstones within the Bradbury group (Fig. 1 and 2), indicative

of deposition in a fluviolacustrine sedimentary system (Anderson et al., 2015; Grotzinger et al., 2014; Mangold et al., 2016; Treiman et al., 2016a; Vasavada et al., 2014). Since reaching Mt Sharp, the rover has investigated over 300 m of stratigraphy within the Mt Sharp group, consisting mainly of laminated mudstone deposits of the Murray and Carolyn Shoemaker formations, which are interpreted as evidence for a long-lived, perennial lacustrine environment (Bennett et al., *this issue*: Edgar et al., 2020; Fedo et al., 2018; Grotzinger et al., 2015; Stack et al., 2019). This long-lived river-lake system within Gale crater likely existed soon after the crater formed approximately 3.6–3.8 Ga based on crater counting (Thomson et al., 2011) with aqueous activity in the crater evidenced beyond the analyses conducted by the MSL mission by the detection from orbit of hydrated minerals (Milliken et al., 2010a; Thomson et al., 2011). However, at some point in Gale crater's geological record, the environment changed to the cold and dry conditions of today, in which geologic processes are dominated by aeolian activity.

The geological units preserved in Mt Sharp are hypothesized to have previously filled in the crater, with aeolian erosion largely responsible for the exhumation of Mt Sharp to its current topographic expression (Bennett et al., 2016; Grotzinger et al., 2015; Malin et al., 2000; Steele et al., 2018). Aeolian processes have also resulted in the formation of modern aeolian landforms including wind-ripples, sand shadows (Blake et al., 2013), transverse aeolian ridges (Zimbelman et al., 2020), and dune fields (Bridges et al., 2017, 2018; Ewing et al., 2017; Lapotre et al., 2018) using the available sediment eroded from the surrounding landscape (Day et al., 2016; Meslin et al., 2013), or transported into the crater from elsewhere (Hobbs et al., 2010).

The Curiosity rover has encountered lithified aeolian sandstone deposits unconformably overlying the Murray formation mudstones as part of the Stimson formation (Fig. 1 and 2) at the Emerson plateau (Banham et al., 2018), Naukluft plateau (Bedford et al., 2020a), and the Murray Buttes (Banham et al., 2021). Most recently, the Stimson formation has been encountered again at the Greenheugh pediment, this time overlying the Carolyn Shoemaker formation mudstone deposits (Fig. 1 and 2). The Stimson formation is currently the youngest in situ geological unit investigated by the Curiosity rover in Gale crater. In this study, we use geochemical data from the Chemistry and Camera (ChemCam) instrument suite and mineralogical data from the Chemistry and Mineralogy (CheMin) instrument to investigate the geological history of the Stimson formation at the Greenheugh pediment. Thereby providing constraints on the paleoenvironment of Gale crater beyond the time in which the river-lake system existed.

1.1 An overview of the Stimson formation and previous localities

Initially identified from orbital imagery on the basis of its high thermal inertia with respect to the surrounding units (Fraeman et al., 2016), the Stimson formation is a dark grey, cross-bedded sandstone within the Siccar Point group (Fig. 2) that unconformably overlies the Mt Sharp group (Banham et al., 2018; Watkins et al., 2016). The unconformity between the Mt Sharp group and the Stimson formation has been informally named the basal Siccar Point group unconformity and is a noticeable divide between the dark grey aeolian sandstones above, and the light-toned mudstones of the Mt Sharp group below (Banham et al., 2018; Watkins et al., 2016). Mineral veins in the Mt Sharp group mudstones are observed to terminate at this unconformity (Fig. 3) suggesting that they formed prior to the erosion of the Mt Sharp group and deposition and lithification of the Stimson formation (Kronyak, et al., 2019a).

Based on orbital mapping, the Stimson formation is exposed over a region of 20 km^2 (Kronyak et al., 2019b). Previous ground-based observations of the Stimson formation showed

that it contains well-sorted to sub-well sorted, rounded sand grains with an average grain size of medium sand with a coarse-grained skew (Banham et al., 2018). Meter-scale cross-bedding is also common across all Stimson formation outcrops so far investigated by the Curiosity rover (Banham et al., 2018, 2021, *this issue*.; Bedford et al., 2020a). The grain size characteristics are indicative of the physical attrition of grains during transportation by saltation and surface creep within migrating dune bedforms in a dry, aeolian environment (Banham et al., 2018). As such, the Stimson formation is a record of a large aeolian dune field that covered the north-west flank of Mt Sharp (Banham et al., 2018, 2021; Bedford et al., 2020a). Further evidence for this interpretation is: the presence of wind ripple strata and meter-scale cross-bedding associated with sediment transport on dune surfaces; and bounding surfaces associated with migration of superimposed dunes.

The Emerson plateau was the first locality in which the Stimson formation was investigated (Fig. 1). The Stimson formation at the Emerson plateau overlies the Murray formation mudstones of the Mt Sharp group surrounding the Pahrump Hills locality (sols 750–940) but was first investigated close-up by the rover at the Marias Pass locality (sols 992–1154). The Stimson formation at the Emerson plateau consists of ~7 m tall outcrops of blocky, dark grey sandstones, predominantly comprising simple cross sets that are usually 0.3–1.0 m thick and are themselves derived of cross-laminations with a uniform thickness of 4 mm (c.f. Banham et al., 2018 for a detailed description of this locality) (Fig. 3C). Bounding surfaces at the Emerson plateau were traced laterally to a distance of ~30 m and are hypothesized to relate to the interdune surfaces (Banham et al., 2018). Three drilled samples were acquired at the Emerson plateau (Fig. 1): the Buckskin drilled sample (sol 1053) of the underlying Murray formation at Marias Pass, the Big Sky drilled sample (sol 1119) representing parent Stimson, and the Greenhorn drilled sample (sol 1137) representing altered Stimson at a fracture-associated halo.

The Naukluft plateau is situated west of the Emerson plateau and was the second Stimson locality to be investigated by the Curiosity rover after the first Bagnold dune field campaign (Fig. 1). The Naukluft plateau is 250 km wide, with the Stimson formation at this locality varying in thickness between 0.5–10 m (Bedford et al., 2020a). The Stimson formation here is characterized by trough-cross bedded sandstones with a similar sedimentary architecture to the Stimson formation at the Emerson plateau (Bedford et al., 2020a) (Fig. 3D). Three drilled samples were also acquired at the Naukluft plateau locality: the Okoruso sample representing Stimson bedrock (sol 1332, Fig. 3d), the Lubango sample of another light-toned fracture-associated halo in the Stimson bedrock (sol 1320), and the Oudam drilled sample taken in the Murray formation just below the Siccar Point group unconformity (sol 1361). Cross-set dip directions of the Stimson formation at the Emerson plateau and Murray Buttes (Fig. 1) suggest sediment transport toward the northeast (Banham et al., 2018, 2021), which is supported by geochemical trends relating to the physical grain segregation of different basaltic materials that also extend this transport direction to the Stimson formation at the Naukluft plateau (Bedford et al., 2020a).

The Murray Buttes locality was the third locality in which the Stimson formation was investigated (Fig. 1). The Murray Buttes were encountered to the southwest of the Naukluft plateau between sols 1412 and 1482 and form a set of isolated buttes and mesas between 5 and 16 m high (Banham et al., 2021). The talus and steep slopes present at the buttes prevented contact science opportunities. As such, the Stimson formation here was only analyzed using Mastcam images, with no opportunities for in situ geochemical or mineralogical analysis (Banham et al., 2021). The Stimson formation at this locality is present as erosion resistant,

cross-bedded cap rock on the buttes and provides the thickest, three-dimensional exposure of the aeolian sandstone deposit of all locations to date (Banham et al., 2021). Once again, the sedimentary architecture at the Murray Buttes is similar to that of the Emerson and Naukluft plateaus, containing meter-scale planar and trough cross-bedding, with the cross-beds consisting of millimeter-thick pinstripe laminations that are laterally continuous for tens of centimeters (Banham et al., 2021). The results from the image analysis supports that the Stimson formation represents a large aeolian sand sea, composed of aggrading compound dunes that, at this location, migrated approximately to the north, downslope of Mt Sharp, which is a slight deviation from the northeast-southwest direction of the Emerson and Naukluft plateaus (Banham et al., 2021). Alteration halos were not observed at the Murray Buttes locality, but calcium sulfate cement and veins and nodules were present in the Murray formation mudstone and Stimson formation sandstone.

1.1.1. The Greenheugh pediment capping unit mini-campaign

The Greenheugh pediment was investigated by the Curiosity rover during the Glen Torridon campaign (Bennett et al., *this issue*; Bryk et al., 2019). The Glen Torridon locality comprises lacustrine mudstone of the Carolyn Shoemaker formation within the Mt Sharp group that has a strong phyllosilicate-signature from orbit (Bennett et al., *this issue*), and a diverse secondary mineralogy containing phyllosilicates, carbonates, and iron oxides that may be indicative of lacustrine groundwater mixing (Thorpe et al., *this issue*). The Stimson formation of the Greenheugh capping unit overlies the Mt Sharp group in the Glen Torridon area (Banham et al., *this issue*; Bryk et al., 2019). On the approach to the Greenheugh pediment capping unit in Glen Torridon, the underlying Carolyn Shoemaker formation mudstone changed in geochemistry, became visually lighter-toned in color (Dehouck et al., *this issue*), and increased in the abundance of F/MgO-rich and FeO_T/MnO-rich alteration features (Gasda et al., *this issue*: Forni et al., 2021), indicative of alteration of the mudstone just below the Basal Siccar Point group unconformity. The mudstone situated close to the Basal Siccar Point group unconformity at the Hutton drill hole (Fig. 2) shows a change in mineralogy with a lower abundance of clay minerals relative to the other drilled samples in Glen Torridon, in addition to minor cristobalite and opal-CT (Thorpe et al., *this issue*; Rampe et al., 2020).

On sol 2695, the Curiosity rover ascended the Greenheugh pediment and reached the pediment capping unit. The Stimson formation of the Greenheugh pediment capping unit can be divided into three stratigraphic intervals. The Gleann Beag interval is the lowermost interval with a thickness of ~3.6 m (Fig. 3B). The Gleann Beag interval is composed of grey, compound cross-bedded sandstones with concretions. Here, cross-bedding dip azimuths are oriented to the northeast (Banham et al., *this issue*). In total, 13 ChemCam targets (113 observation points) were measured at the Gleann Beag interval analyzing concretionary and non-concretionary bedrock. The concretions of this interval range in size between 5–20 mm diameter and preserve the sedimentary features of the sandstone (Banham et al., *this issue*). Two additional targets were measured at the base of the Gleann Beag interval that also sampled light-toned Stimson bedrock immediately above the unconformity with irregularly shaped, white clasts ~1 mm long (Banham et al., *this issue*). These clasts were interpreted as rip-up clasts derived from the Carolyn Shoemaker formation due to their similar visual appearance to the underlying mudstone and similar shape to rip-up clasts identified at the Marias Pass locality (Banham et al., *this issue*; Newsom et al., 2016).

Above the Gleann Beag interval is the Ladder interval (Fig. 3A and 3B). This interval consists of simple and concordant cross-sets with cross-laminations that dip to the south. Concretions are rare in this interval (Banham et al., *this issue*). Five ChemCam targets sampled the Ladder interval, although only three analyzing the uppermost Machir Bay outcrop (25 observation points) are of a sufficient data quality to be included in the study.

Finally, the Edinburgh interval is the uppermost stratigraphic interval that was investigated by the Curiosity rover (Fig. 3A). This interval contains trough cross-bedded sandstone with cross-set dip directions to the west (Banham et al., *this issue*). In this interval, concretions were very rare, and one drilled sample (Edinburgh, sol 2715, Fig. 3a) was delivered to the CheMin and SAM instruments (Sutter et al., 2022; Rampe et al., 2020). The Edinburgh drilled sample contained a high abundance of plagioclase feldspar (28.9 wt%), pyroxene (20.2 wt%), olivine (8.4 wt%) and magnetite (10.2 wt%), in addition to K-feldspar (3.4 wt%), phyllosilicates (7 wt%), trace fluorapatite and an X-ray amorphous component (20 wt%) (Thorpe et al., *this issue*; Rampe et al., 2020). ChemCam analyzed 30 targets in this interval (259 observation points) in addition to 1 target of a sedimentary float rock (Cheviot Hills, sol 2696) and 1 soil (Digg, sol 2710).

1.2 A geochemical and mineralogical analysis of Gale crater's ancient dunes

1.2.1. Constraining aeolian net sediment transport direction and provenance

Previous studies of aeolian dunes derived from basaltic material on Earth and Mars have shown that major element chemistry can provide information on mineral sorting processes that can in turn constrain net sediment transport direction and changes in the sediment source (Baratoux et al., 2011; Bedford, et al., 2020a; Cornwall et al., 2015; Sara, 2017; Mangold et al., 2011; Mountney et al., 2004; O'Connell-Cooper et al., 2017; Rampe et al., 2018). Basaltic sand grains can be monomineralic, composed of olivine, pyroxene, and feldspar grains, derived from volcanic or impact glass, or polymineralic, composed of a mixture of basaltic minerals and glass (Cornwall et al., 2015; Fedo et al., 2015). The minerals within each grain determine the density, shape, and resistance to physical and chemical weathering that in turn determine how they will be sorted hydrodynamically with transportation in an aeolian environment (Cornwall et al., 2015; Fedo et al., 2015; Jerolmack et al., 2006; Morrone et al., 2017; Willetts et al., 1982).

On Earth, most mature aeolian sands are dominated by quartz as this mineral is the most resistant to physical and chemical weathering (Muhs, 2004; Pettijohn, 1954). Mafic minerals in sedimentary environments on the Earth are uncommon because Earth's continental crust largely consists of felsic materials and reactive basaltic materials are easily chemically weathered under Earth's active hydrological cycle (Nesbitt et al., 1992). However, on Mars, the crust is predominantly basaltic, and the cold and arid climate of the Amazonian geological period has resulted in physical weathering being the main driver in the diminution of aeolian sediments. Physical abrasion studies by Cornwall et al (2015) show that olivine grains are rapidly abraded to a spherical shape that aides its transportation in aeolian environments. Meanwhile the cleavage planes of feldspar and pyroxene act as zones of weakness in monomineralic sand grains and hinder the sphericity of these grains. Glass and polymineralic basaltic grains show the most resilience to physical abrasion. These properties result in olivine minerals, glass, and basaltic

fragments being transported farther and concentrating in mature aeolian sands, relative to feldspar grains. Mineral sorting studies of basaltic aeolian sands in Iceland show that an increase in MgO + FeO_T with distance from the source corresponds to an increase in olivine relative to feldspar regardless of the presence of basaltic grains and glass (Baratoux et al., 2011; Sara, 2017; Mangold et al., 2011). As the mineral sorting acts on feldspar minerals and olivine, it is possible to use the variation in MgO + FeO_T relative to Al_2O_3 + Na_2O + K_2O to measure the variation in the mafic and felsic basaltic materials, respectively (Baratoux et al., 2011; Mangold et al., 2011).

In Gale crater, several studies have used the geochemical data from the ChemCam instrument to probe the geochemical variation in aeolian sediments in relation to mineralogical variations (Bedford et al., 2020a; Cousin et al., 2017; Meslin et al., 2013). ChemCam geochemical data of modern aeolian sediments from Gale crater show that locally derived sands consist of coarse feldspar grains in addition to finer mafic material (Cousin et al., 2015; Meslin et al., 2013), whereas, the mature aeolian sands of the Bagnold dune field only contain feldspar within polymineralic grains, or as fine monomineralic grains (Cousin et al., 2017; Rampe et al., 2018). A statistical geochemical analysis of ChemCam data from the Emerson and Naukluft plateaus was applied to determine trends associated with mineral sorting during transportation prior to deposition and lithification (Bedford et al., 2020a). The results showed that the Emerson plateau had a higher abundance of MgO and FeO_T relative to the Naukluft plateau, which was more felsic in chemistry and had a greater proportion of coarser feldspar grains identified in ChemCam Remote Micro-Imager (RMI) images (Bedford et al., 2020a). The geochemical variation of the Stimson formation at the Emerson and Naukluft plateaus indicated that net sediment transport direction was from southwest-to-northeast (Bedford et al., 2020a), supporting the results of Banham et al. (2018). This net sediment transport direction is opposite to that of the active Bagnold dunes, and when the geochemistry of the ancient dunes and modern dunes are directly compared to one another, they show geochemical differences indicative of different basaltic provenances (Bedford et al., 2020a). The geochemistry of the Stimson formation sandstone was more similar to that of the subalkaline basaltic sediments that are a source for the Bradbury group fluvial sandstones, suggesting that the two geological units either shared a similar sediment source, or that the Stimson sandstones may consist of recycled Bradbury group material (Bedford et al., 2020a). Due to the variation in cross-set dip directions between intervals in the Stimson formation at the Greenheugh capping unit (cf Banham et al., *this issue*), we will compare the geochemistry of each interval at the Greenheugh pediment to that of the Stimson formation at the Emerson and Naukluft plateaus using the methods of Bedford et al. (2020a) to determine if the geochemical variation supports changes in sediment transport direction and potentially sediment provenance.

1.2.2. Constraining aqueous alteration of the Stimson sandstone

The alteration features of the Stimson sandstone have been of particular interest in several studies as they can provide information on the nature of the groundwater that existed after the habitable river-lake system ended, and after the erosional moat formed within Gale crater. Although the timing of Stimson deposition and lithification on the slopes of Mt Sharp is not well constrained, it is likely that the Stimson sandstones formed in the mid- to late-Hesperian (Banham et al., 2021), making the alteration features within the Stimson formation representative

of some of the youngest aqueous alteration events observed in situ, at the time of this publication. Previous research suggests that the Stimson formation at the Emerson and Naukluft plateaus was potentially lithified by a rising capillary fringe that did not interact with the depositional surface (Banham et al., 2018). This interaction between groundwater and mafic minerals in the aeolian sediments (particularly olivine) caused the formation of an iron oxide and X-ray amorphous materials as cement, isochemical to the previous sandstone deposit, and preferentially cemented as concretions closer to the unconformity (Bedford et al., 2020a; Hausrath et al., 2018).

After lithification of the Stimson sandstone, repeated episodes of groundwater emplacement and desiccation formed the polygonal fractures and calcium sulfate hydrofracture veins in the Stimson sandstone (Frydenvang et al., 2017; Hausrath et al., 2018; Kronyak et al., 2019a, 2019b; Yen et al., 2017, 2021). Multiple alteration features occur within the Stimson formation of the Emerson and Naukluft plateaus such as concretions, mineral veins and the alteration halos which were sampled at Greenhorn and Lubango (Fig. 4). Concretions are more common towards the unconformity, similar to what is observed at the Greenheugh pediment (Banham et al., 2018, *this issue*; Bedford et al., 2020a) (Fig. 4). An analysis of concretionary versus non-concretionary Stimson bedrock at the Emerson and Naukluft plateaus by the ChemCam instrument showed that there is no statistically significant geochemical variation of these features to the surrounding bedrock (Bedford et al., 2020a). This supports the hypothesis that the concretions at these localities likely formed through in situ isochemical alteration and represent parts of the bedrock that were preferentially cemented during the lithification of the sandstone (Banham et al., 2018; Bedford et al., 2020a).

Light-toned, silica-rich Stimson bedrock surrounding large fractures, known as silica-rich alteration halos, are present in the Stimson formation at the Emerson and Naukluft plateaus (Bedford, et al., 2020a; Frydenvang et al., 2017; Yen et al., 2017). Silica-rich halos are geochemically characterized by an increase in SiO_2 abundances up to 80 wt% and a decrease in all other major element oxides except TiO_2 and K_2O whose compositions are scattered across observation points (Bedford et al., 2020a; Frydenvang et al., 2017; Yen et al., 2017). Two hypotheses exist for the formation of the halos. Either, the halo alteration occurred through the remobilization of silica from the underlying mudstones by neutral to alkaline pH fluids into the fractures in the Stimson bedrock where they precipitated to form the halos (Frydenvang et al., 2017). Alternatively, it has been hypothesized that they formed as a result of acidic fluids circulating through the fractures, interacting with the mafic minerals in the surrounding bedrock, remobilizing their cations and forming a silica-rich residue (Hausrath et al., 2018; Yen et al., 2017). The timing of the silica-enrichment that formed the light-toned halos relative to the formation of the calcium sulfate veins and cement is currently unknown, however, previous studies agree that these represent some of the latest stages of diagenesis in the Stimson formation and underlying Murray formation at these localities (Frydenvang et al., 2017; Yen et al., 2017).

Polygonal fractures with average widths of 7.5 m can also be identified by orbital images and from the surface in the Stimson formation at the Emerson plateau, Naukluft plateau, and to a lesser extent at the Greenheugh pediment (Kronyak et al., 2019b). These polygonal fractures are similar in appearance to the surrounding bedrock, only evident as they are slightly raised due to their greater erosion resistance (Kronyak et al., 2019b). Based on their geomorphology, the polygons likely formed as a result of multiple cycles of expansion and contraction of the bedrock caused by the recharge of near-surface groundwater preferentially cementing these zones

(Kronyak et al., 2019b). The polygons are not likely related to the diagenesis that formed the silica-rich halos or the calcium sulfate mineral veins as these features do not consistently correlate spatially across the Siccar Point group (Kronyak et al., 2019b).

The small sampling size of the ChemCam laser in addition to the thorough documentation of each target by RMI images before and after sample acquisition makes it possible to isolate observation points with alteration features and compare them to the bedrock, constraining alteration processes. Here, we compare alteration features and examine variations in potential sandstone cementing agents between the different Stimson formation locations in order to further constrain the spatial scale of these late-stage aqueous alteration events in Gale crater.

2 Materials and Methods

2.1 The ChemCam instrument

The ChemCam instrument suite utilizes Laser-Induced Breakdown Spectroscopy (LIBS) to obtain elemental analyses of a geological target situated over ~2 m from the rover mast, with most of the targets selected at a distance less than 5 m from the rover mast (Maurice et al., 2012, 2016; Wiens et al., 2012). LIBS spectra are pre-processed to remove ambient light background, continuum background, and noise (Wiens et al., 2013). The quantification of elemental abundances is obtained for major elements (Si, Ti, Al, Fe, Mg, Ca, Na, K) through a combination of partial least squares regression sub-models and independent component analysis using a large spectral training set (Anderson et al., 2017; Clegg et al., 2017; Forni et al., 2013). Minor and trace elements are quantified individually, often using the same spectral library. Relevant to this work, MnO quantification is described in Gasda et al. (2021). Hydrogen quantification has been shown to require special attention to the matrix (Rapin et al., 2017a; Rapin et al., 2017b; Schröder et al., 2015; Thomas et al., 2018); nevertheless it has proven useful in some specific cases (e.g., Rapin et al., 2016), and rough quantification can be used for large-scale studies (Thomas et al., 2020). The ChemCam team discovered that while F atomic emission lines are not generally detectable, F enrichments can be observed and quantified via the CaF molecular emission band, which has indicated the presence of apatite, fluorite, and mica grains (Forni et al., 2015).

The uncertainty of major elemental abundances based on ChemCam data has been presented as accuracy and precision to 1σ (Anderson et al., 2017; Clegg et al., 2017; Wiens et al., 2012) and is provided in the Supplementary information (Table S.1). Accuracy relates to the root mean square error of prediction (RMSEP) for representative geological samples that share abundance ranges similar to those in the calibration regression models (Clegg et al., 2017). The precision of the predictions is calculated as the variation observed across the 25 shots that derive the average spectrum for each observation point (Blaney et al., 2014), or across targets from a uniform unit (Mangold et al., 2016).

ChemCam targets are taken in a linear or grid raster configuration i.e., 3×3 or 1×10 (Maurice et al., 2016). Each point of the raster is known as an observation point, where each observation point consists of between 30–50 laser shots. Spectra from the first 5 laser shots are not included in the average spectrum and serve to minimize surface dust contamination (Clegg et al., 2017). The ChemCam instrument suite also contains a Remote Micro-Imager (RMI) which

takes high-resolution (60–100 μrad) images of targets pre- and post-acquisition of the LIBS spectral data in order to provide geological context for the targets in question (Le Mouélic et al., 2015).

2.2 The CheMin instrument suite

CheMin housed within the rover body and generates X-ray diffraction (XRD) patterns of drilled rock or scooped sediment samples (Blake et al., 2012; Morrison et al., 2018a). Rietveld refinement and full-pattern fitting techniques are used to quantify abundances of minerals and X-ray amorphous material and to determine unit-cell parameters of the major crystalline phases (Blake et al., 2012, Morrison et al., 2018a). Mass-balance calculations using mineral abundances and crystal chemistry from CheMin and geochemical data from APXS provide estimates of the composition of the amorphous component (e.g., Smith et al., 2018). Evolved gas analyses from the Sample Analysis at Mars (SAM) instrument suite help identify clay minerals and amorphous materials (e.g., Sutter et al., 2017). In this study, we use the CheMin-derived mineral abundances of the Stimson formation sandstone at the Emerson plateau (Big Sky, sol 1119; Morrison et al., 2018; Yen et al., 2017), Naukluft plateau (Okoruso, sol 1332; Morrison et al., 2018b; Yen et al., 2017), and Greenheugh pediment capping unit (Edinburgh, sol 2711; Rampe et al., 2020) to place the geochemical compositions from the ChemCam instrument into mineralogical context.

2.3 The on-board science cameras and target classifications

In this study, we have individually classified each ChemCam observation point using the RMI images according to whether the observation point has analyzed bedrock, secondary diagenetic features, unconsolidated sediments, or float. Where available, images from the Curiosity rover's other on-board science cameras, Mastcam (Mast camera) and MAHLI (Mars Hand Lens Imager), were used to support the classification at the scale of the outcrop and target, respectively. Mastcam includes two, fixed-focal length, multispectral, color CCD imagers situated on Curiosity's mast (Malin et al., 2017). The two Mastcam imagers are separated by 24.2 cm and positioned approximately 2 m from the surface (Malin et al., 2017). The left Mastcam (M-34) has a focal length of 34 mm, a field of view (FOV) of 20° × 15°, and a pixel scale of 0.22 mrad/pixel (Malin et al., 2017). Meanwhile, the right Mastcam (M-100) has a 100 mm focal length, a FOV of 6.8°×5.1°, and a 0.074 mrad/pixel scale of sampling (Malin et al., 2017). Data from this instrument were used to identify large-scale features, such as cross-bedding or alteration halos, and to locate the ChemCam targets with respect to the stratigraphic units. MAHLI is situated on the turret at the end of the Curiosity rover's arm and uses a 2-mega-pixel color CCD camera to analyze the textures, structures, and morphologies present at the finest grain size possible for Curiosity's cameras, 0.0042 mm (silt) (Edgett et al., 2012; Mangold et al., 2017). Data from this instrument were used to provide additional, high resolution, color data to support the classifications of the black and white images from the ChemCam RMI.

Bedrock is defined here as an indurated, lithified unit, possibly containing sedimentary structures such as bedding or laminations, and secondary structural features such as bedrock fractures. As the sedimentary units of the Bradbury group, Mt Sharp group, and Siccar Point group (Stimson formation) have undergone compaction and cementation during diagenesis, it is important to note that these analyses are not completely free of alteration as they include diagenetic cement. However, provided that the diagenesis which formed the sandstone cement was relatively isochemical, the geochemistry can be used to identify mineral sorting trends

before the units became lithified, in addition to sediment source rock characteristics. Concretions are abundant in the Stimson formation which likely formed through the preferential cementation of the Stimson sands (Banham et al., 2018; Bedford et al., 2020a; Potter-McIntyre et al., 2014; Potter et al., 2011). A previous analysis of concretions in the Stimson formation sandstone by both the Alpha Particle X-ray Spectrometer (APXS; e.g., Gellert & Clark, 2015) and ChemCam instruments showed that they have the same geochemical composition to non-concretionary Stimson (Bedford et al., 2020a; Siebach et al., 2017) and are hypothesized to relate to closed-system diagenesis that preserves the bulk rock geochemistry (Banham et al., 2018; Bedford et al., 2020a; Siebach et al., 2017). This is also true for the Greenheugh pediment capping unit for concretions smaller than 5 mm (Appendix A); as such they are included in the bedrock dataset. However, larger concretions that are greater than 5 mm (Fig. 4), with multiple ChemCam observation points directly on the concretions, and which occur closer to the unconformity have been isolated from the bedrock dataset of all Stimson localities for a more in-depth analysis on the diagenesis that formed these features. As the Stimson formation across all localities has a relatively uniform grain size (Banham et al., 2018; 2021; *this issue*), we have not classified bedrock targets according to grain size. Bedrock targets do not include analyses of drill tailings and dump piles as these samples have been modified by the rover. Furthermore, bedrock analyses have been restricted to only include observation point data with oxides that sum to between 90–105 wt% to minimize the influence of volatile elements (S, Cl, and H), or elements such as Ni which are not nominally quantified in ChemCam data. Removing the potential impact of volatile elements is important for our bedrock dataset as these elements may have been emplaced due to open-system alteration. Restricting the total sum of oxides can further remove any targets that have been contaminated with Martian soil, as these deposits also have higher concentrations of volatiles (Bish et al., 2013; Ehlmann et al., 2017; Lasue et al., 2018; Meslin et al., 2013; O'Connell-Cooper et al., 2017).

ChemCam analyses that have targeted secondary diagenetic features in the Stimson sandstone have been placed into an alteration feature dataset and subclassified according to "vein", and "halo" categories. Vein alteration targets relate to light-toned mineral veins that in-fill hydrofractures in the Stimson formation (Bedford et al., 2020a; Kronyak et al., 2019a). Halos relate to the light-toned halos that extend into the Stimson bedrock ~20 cm either side of large fractures (Fig. 4) (Bedford et al., 2020a; Frydenvang et al., 2017; Yen et al., 2017). These secondary diagenetic features have been separated from the bulk rock dataset to isolate the effects of later diagenetic alteration from geochemical trends that may relate to the sediment source characteristics of the Stimson formation across all localities, in addition to pre-lithification mineral sorting processes, and the formation of the sandstone cement.

Other classifications include float and soils. Float targets in Gale crater include pebble to boulder grain size fragments of rock that can be igneous, sedimentary, or meteoritic in nature. Soil targets are classified as unlithified deposits, with a lack of obvious cement that derive fine-grained accumulations of sand- to silt-grained particles (Bish et al., 2013; Cousin et al., 2015; Meslin et al., 2013). The Curiosity rover also encountered two large, active, aeolian dune fields, and investigated them in two phases of the Bagnold dune campaigns (Bridges et al., 2018; Lapotre et al., 2018). The aeolian dunes occur as large bedforms, ~15 m across, which are dark in color and can be considered a modern analog of the ancient Stimson formation (Achilles et al., 2017; Bedford et al., 2020a; Hausrath et al., 2018). Due to the similarities in characteristics of

the dune and soil deposits, ChemCam analyses of these deposits have been placed into the soil category.

2.4 Statistical methods and data interpretation

The ChemCam LIBS laser sampling footprint is 350–750 μm for distances 3–7 m from the rover mast (Maurice et al., 2012), which is a similar size to the average grain size of the Stimson formation (336–634 μm at the Greenheugh pediment, Banham et al., *this issue*). As such, target analyses are not likely to be representative of whole rock compositions as individual grains are more likely to be sampled (Cousin et al., 2017). However, the bedrock Stimson formation ChemCam dataset to date (August, 2021) consists of 741 data points which permits the use of a statistical approach to both estimate a bulk rock composition and detect geochemical trends that may relate to mineralogical variations in the relatively alteration-free bedrock dataset. For each locality and stratigraphic interval of the Stimson formation, we give the basic statistics (mean, median, range, and standard deviations), followed by density contour plots which will be used to estimate the bulk rock composition. Density contours display the data across two variables and represent the density of smoothed data within each pixel on the bivariate plot defined according to the bin size (Bedford et al., 2019a; Eilers et al., 2004). Data densities are smoothed according to Eilers and Goeman (2004), and contours are generated using MATLAB (2019a). This method is used to estimate the bulk rock composition which is in turn used as a comparison to the geochemical variation associated with the alteration feature datasets. By comparing the estimated whole rock composition to alteration features, we can constrain how these features formed.

After the density contour analysis, sandstone components (the minerals and amorphous materials that comprise the sand and cement) are delineated using a hierarchical, agglomerative cluster algorithm on the bedrock dataset with Minitab 19 statistical software (2020), following the methods of Bedford et al. (2020a) and Bedford (2019a). In this study, we use the complete linkage measure of association for Euclidean distances with all major oxides, now including MnO, and the total sum of oxides, as the variables. Complete linkages and Euclidean distances were used as these methods provided the best fit for the dataset showing the most defined clusters and was successfully used in a previous investigation of the Stimson formation (Bedford et al., 2020a). Clustering methods have also been successfully employed in other studies of Gale crater sediments (Rammelkamp et al., 2021; Gasnault et al., 2019, 2013). Variables were standardized in order to minimize the effect of scale differences.

3 Results

3.1. Distribution of the classified data across the Stimson formation

In total, 430 ChemCam observation points were acquired during the Greenheugh pediment mini campaign that were analyzed <4 m from the rover and were of good data quality. This included 324 bedrock analyses, two analyses of calcium sulfate veins, 10 soil analyses, 10 float analyses, 20 analyses that targeted large (>5 mm) nodules, and 15 analyses of the Edinburgh drill hole wall and tailings (Fig. 5). This is in contrast to the distribution of observation point classifications for the Emerson and Naukluft plateaus which has a much larger proportion of observation points (50% at Emerson plateau, 65% at Naukluft plateaus) that targeted alteration features such as halos, concretions, and calcium sulfate veins (Fig. 5). These

proportions are not a result of the true distribution of these features relative to bedrock as targeting bias to investigate certain features has played a role. Regardless, the diversity of alteration at the Greenheugh capping unit is significantly less than the diversity of the features seen previously, with no alteration halos were identified at the Greenheugh pediment capping unit, unlike at the Emerson and Naukluft plateaus (Fig. 5) or any obvious raised ridge features in comparison to the 15 raised ridge analyses at the Emerson plateau spanning 2 targets (Tinder Box and Duperow), and the 7 raised ridge analyses of the Uubvley and Bloedkoppie targets at the Naukluft plateau.

Calcium sulfate mineral veins are rare at the Greenheugh pediment capping unit with only two observation points targeting a very thin mineral vein (Fig. 4) and rare occurrences of veins identified in the Mastcam images. Calcium sulfate veins were also rare at the Emerson and Naukluft plateaus with 15 and 27 ChemCam targets of veins respectively, but where they did occur the veins were larger in size and extent than the vein investigated at Greenheugh (Fig. 4). Concretions are also present across all sites. All the large and small concretions at the Greenheugh locality were observed in the lowermost Gleann Beag interval in the ChemCam data and Mastcam images (Fig. 3B and 4). Consequently, there is a similar number of large concretion analyses in the Stimson formation at the Greenheugh pediment (20 points over 4 targets) and the Naukluft plateau (29 points over 6 targets). Only three observation points in the targets Dakota and Heath sampled large concretions in the Stimson formation at the Emerson plateau.

Of the 324 bedrock analyses, 220 constituted data within the 90–105 wt% total sum of oxide range. This suggests that 104 observation points on the Greenheugh capping unit contains a higher abundance of volatile elements (S, H, or Cl) or other elements which are not routinely quantified, 82% of which are within the Edinburgh interval. Due to a distinct geochemistry in two ChemCam targets situated just above the Siccar Point group unconformity, 20 observation points were placed into their own dataset for an analysis of the unconformity relative to the bulk Greenheugh pediment capping unit.

3.2. Geochemistry of the Greenheugh pediment capping unit compared to the Stimson formation at the Emerson and Naukluft plateaus

The geochemistry of the Greenheugh pediment capping unit is similar to that of the Stimson formation analyzed previously, with geochemical distributions, mean compositions, and standard deviations within family to both previous Stimson formation localities for TiO_2, FeO_T, and K_2O (Fig. 6 and Table 1). For all localities, TiO_2, FeO_T, and K_2O have unimodal distributions, with mean compositions and standard deviations of 0.9 ± 0.2 wt%, 19.5 ± 2.8 wt%, and 0.6 ± 0.4 wt%, respectively (Fig. 6). Both distributions for TiO_2 and K_2O have a heavy right tail, which is the most prominent for the Emerson plateau, though these heavy right tails do not significantly skew the median compositions from the mean. Two-way equivalence tests also support that these major element oxides are equivalent across the three Stimson localities within the upper and lower limits defined by ChemCam precision (Supplementary material) and they suggest that Na_2O can be claimed as equivalent across the three sites, despite the slight variation in distribution (Table S.2). For all three sites, Na_2O has a mean composition and standard deviation of 3.0 ± 0.8 wt%, with multimodal distributions presenting peaks at 1.8 wt%, 2.7 wt%, 3.1 wt%, and a heavy tail to the right. However, the distribution in data between these peaks differ across all sites (Fig. 6). The dominant peak for the Emerson plateau and Greenheugh

capping unit is at 2.7 wt%, with both of these localities showing fewer data extending to higher Na_2O concentrations. In comparison, the Naukluft plateau's dominant peak is at 3.1 wt%, with a greater proportion of data points situated over 4 wt% Na_2O.

The mean compositions of SiO_2, Al_2O_3, MgO, CaO, and MnO across the Stimson formation localities are all situated within 1 standard deviation of each other (Table 1), however, variations in the distribution of the data suggests that there may be statistically significant differences, supported by equivalence test results (Table S.2). The Emerson plateau and Greenheugh pediment capping unit both share unimodal SiO_2 distributions with peaks at 45 wt% (Fig. 6). However, the distribution of SiO_2 at the Emerson plateau shows a right skew to higher SiO_2 concentrations up to 57.1 wt%, whereas the Greenheugh pediment capping unit shows a skew to the left with a greater proportion of data points <44 wt% SiO_2 causing the non-equivalence between the Emerson plateau and Greenheugh pediment capping unit. The Naukluft plateau has a distinct bimodal distribution for SiO_2 sharing the peak at 45 wt% with an additional, larger peak at 48 wt%. This second larger peak for the Naukluft plateau, in addition to values up to 61.7 wt% SiO_2, results in a lack of equivalence for SiO_2 between the Naukluft plateau and other Stimson localities. The high SiO_2 observation points of the Emerson and Naukluft plateaus were cross-checked with the locations of the silica-rich alteration halos and the RMI images, and either correlate with large, light-toned mineral grains (Fig. 3d), or they were randomly interspersed within the target raster which is not consistent with the 10s of cms-scale alteration halo features (Bedford et al., 2020a; Frydenvang et al., 2017). Instead, the correlation of these high SiO_2 values with high Na_2O and/or K_2O, and low MgO and FeO_T suggest that they may relate to ChemCam analyses that have targeted a greater proportion of felsic grains (Bedford et al., 2020a). Thus, the statistically significant differences may be indicative of different proportions of minerals comprising the sand (e.g., olivine, basaltic glass, and feldspar) or differences in cement composition at each locality.

The Greenheugh capping unit shows statistically significant geochemical variation from the Emerson and Naukluft plateaus for Al_2O_3, and CaO, which is on average lower at the Greenheugh capping unit, and MnO and MgO which is higher in mean abundance (Fig. 6). Al_2O_3 compositions show a bimodal distribution for the Emerson and Naukluft plateaus, with the histograms showing peak abundances at 10 wt% and 17 wt% for the Emerson plateau, and peaks at 12 wt% and 17 wt% at the Naukluft plateau. Meanwhile, the Greenheugh pediment capping unit has a multimodal distribution with peaks at 8 wt%, 10 wt%, and 16 wt%. The additional peak of the Greenheugh capping unit at 8 wt% has resulted in lower mean (10.3 ± 0.2 wt%) and median (9.6 wt%) compositions compared to the rest of the Stimson formation localities with average compositions of 11.3 ± 0.2 wt% and 12.1 ± 0.2 wt% for the Emerson and Naukluft plateaus, respectively.

Both the Emerson and Naukluft plateaus have a unimodal distribution for MgO, with a peak at ~7.5 wt%, while the Greenheugh pediment capping unit has a bimodal distribution with peaks at 7 wt% and 9 wt%. All localities have a right tail to MgO concentrations of >17 wt%, generating a slight right skew in the datasets (Fig. 6).

The distribution in CaO is also the same between the Emerson and Naukluft plateaus in that both are unimodal with a dominant peak at 6.4 wt%. Meanwhile, the Greenheugh pediment

capping unit has a bimodal distribution with the 6.4 wt% peak shared with the other localities, in addition to a different, more dominant peak at 4.0 wt%.

MnO has a unimodal distribution for all localities with a strong peak at 0.2 wt%, however, outliers exist to high concentrations at the Emerson plateau (up to 2.6 wt%) and Greenheugh capping unit (4.0 wt% in target Aegis_post_2730). The outlying MnO values at the Greenheugh pediment capping unit are more numerous than those of the Emerson plateau, and all occur within the Edinburgh interval bedrock targets, generating a mean concentration that is ~1.6x that of the Emerson and Naukluft plateaus.

To summarize, the Stimson formation at the Greenheugh pediment capping unit is situated within the compositional range of earlier Stimson units, according to the standard deviation of the dataset. However, statistically significant variations in the geochemical distribution of the dataset exist, as is evident in the mean, equivalence test results, and the histograms of major element oxides. The Greenheugh pediment capping unit has a higher abundance of MgO and MnO, and lower abundances of SiO_2, Al_2O_3, and CaO relative to the Stimson formation at the Emerson and Naukluft plateaus that may relate to different abundances of sandstone components such as mafic minerals, felsic minerals, or sandstone cement.

3.3 Geochemical variation associated with diagenetic features and the unconformity at the Greenheugh capping unit.

Calcium sulfate veins across the Stimson formation show a decrease in all major oxide compositions and total sum of oxides, except for CaO that can reach values up to 50 wt% (Bedford et al., 2020a). The two calcium sulfate veins targeted on the Greenheugh pediment capping unit were both situated in the Edinburgh interval and as a result of both veins being very thin (<1 mm wide), the analyses of these veins only show a slight increase in CaO compared to the average of the Edinburgh interval. Calcium sulfate can also be a cement component. For Stimson analyses across all localities with total sum of oxides less than 90 wt%, 23 analyses out of 191 share a similar geochemical trend to the calcium sulfate mineral veins, suggesting that calcium sulfate cement is present in these ChemCam observation points. For the Greenheugh pediment capping unit, 11 observation points that targeted bedrock have geochemical signatures of calcium sulfate cement, suggesting that it is a small component of the sandstone and is variable in its distribution.

Large concretions (>2 cm) in the Stimson formation preserve sedimentological features such as laminations and therefore likely represent parts of the sandstone that have been preferentially cemented (Banham et al., 2018). To conduct a closer investigation of how the sandstone cement of the Stimson formation varies across the Greenheugh capping unit, we have isolated the compositions of these large concretions and plotted them alongside the geochemical abundances of the non-concretionary bedrock and small concretionary bedrock (S.5). Similar to the results of Bedford et al. (2020) for the Emerson and Naukluft plateaus, no statistically significant geochemical variation is present across concretions (Fig. S.5).

To investigate how the geochemistry of the Greenheugh pediment capping unit varies with respect to the basal Siccar Point Group unconformity, and in turn how it may vary for the immediately underlying Carolyn Shoemaker formation, we have classed the bedrock data in relation to the stratigraphic levels just above (Stimson Unconf.), and just below (CS Unconf.) the unconformity (Fig. 7 and 8). In addition to the targets closest to the unconformity, we also

compare the results of analyses acquired at the base of the pediment around the Hutton drill hole (CS Hutton) and the analyses acquired farther above the unconformity in the Stimson formation stratigraphic intervals (Glean Beag interval, Ladder interval, and Edinburgh interval). As the previous literature has suggested that the unconformity may have been a conduit for diagenetic fluids to travel and alter the underlying Carolyn Shoemaker formation (Achilles et al., 2020; Fraeman et al., 2020; Horgan et al., 2020; Rampe et al., 2020), we have not restricted the bedrock totals for this analysis, to allow for geochemical variation associated with secondary phases that formed through water-rock interactions to be more apparent. The mean compositions and their associated standard errors of the Stimson formation and Carolyn Shoemaker formation are also shown for comparison (Fig. 7). Figure 7 shows that the Carolyn Shoemaker formation leading up to the unconformity is depleted in SiO_2 and H but enriched in CaO relative to the mean composition of the Carolyn Shoemaker formation. The Stimson formation just above the unconformity (Stimson Unconf.) has a unique geochemistry that is low in MgO, Na_2O, and MnO, low in total sum of oxides, but high in CaO and H relative to the mean composition of the Stimson formation. These geochemical characteristics of the base of the Stimson formation indicate that it may have either been affected by diagenetic fluids, been derived from a different sediment provenance, or represents a complex mixture of both processes.

3.4 The distribution of halogens across the Stimson formation.

For the bulk rock dataset, all Stimson formation localities have a unimodal distribution of H peak area about 0.004, however, the Stimson formation at the Greenheugh pediment has a bimodal distribution with a second modal peak of H peak abundances at a value of 0.008 (Fig. 6). This contrasts significantly with the right-skewed unimodal distributions of the Emerson and Naukluft plateaus. Looking at the distribution of the H data in relation to the stratigraphic intervals at the Greenheugh pediment (Fig. 8A), these peak area values are divided between the Gleann Beag interval that contains concretions and is situated close to the unconformity, and the Ladder and Edinburgh intervals that do not contain notable concretions and are higher in the stratigraphy (Fig. 8). The Gleann Beag interval shares the modal H peak area with that of the Stimson formation at the Emerson and Naukluft plateaus, whereas the Ladder and Edinburgh intervals exclusively have the higher H peak area. ChemCam analyses of the non-concretionary bedrock have the highest H peak area (0.0052) compared to small concretions (0.0046) and large concretions (0.0039), however the change in surface roughness between these classifications likely impacts the H signal (Rapin et al., 2017a; Schröder et al., 2015). As such, we do not consider the H peak area to differ significantly across the concretions. H peak area is also variable among the other diagenetic features, with the calcium sulfate veins having the highest H abundances (mean of 0.01) of all features and bedrock analyzed by ChemCam. Silica-rich halos also had a slightly higher mean H abundance (0.007) than that of the average Stimson, unaltered bedrock (0.005). Only MnO has a possible positive correlation with H abundance for targets on the Edinburgh interval with MnO > 1 wt% (r^2 49%, p = 0.011).

F detections across the Stimson formation are rare. In total, there are 20 bedrock observation points (16 non-concretionary bedrock, four small concretion-rich bedrock), and two halo analyses across all Stimson localities that have F above the limit of detection. Only one observation point in the Edinburgh interval of the Greenheugh pediment capping unit has F, contrasting with the high F targets in the underlying Carolyn Shoemaker formation of the Hutton zone (Dehouck et al., *this issue*; Gasda et al., *this issue*). For the bedrock targets, F has a potential positive correlation with CaO (r^2 48%, p = 0.001; S.3) and shares no correlations with

any other major element oxide. F has the largest range in abundances for targets close to the unconformity (0.7 wt% F), compared to those situated over 1.5 m above (0.2 wt% range in F; Fig. S.4).

3.5 Stimson bedrock cluster analysis results

The results of the cluster analysis show that the Stimson formation bedrock dataset can be divided into 5 clusters (Fig. 9). Cluster 1 is defined as the cluster with the highest mean MgO content (14.7 ± 1.1 wt%), higher than average MnO (0.7 ± 0.2 wt%) and the lowest Al_2O_3 (6.9 ± 0.4 wt%), CaO (3.6 ± 0.4 wt%), Na_2O (2.3 ± 0.1 wt%), and K_2O (0.3 ± 0.1 wt%) of all clusters (Table 2). Nineteen data points have a Cluster 1 membership from across the Stimson formation with eight at the Greenheugh pediment (Fig. 9, 10). Cluster 1 is most similar to Cluster 2 and is differentiated by a similarity level of 36.3 (see Bedford (2019) for the methods to calculate similarity level). Cluster 2 has a moderately high abundance of MgO (8.6 ± 0.1 wt%) with the greatest variation in TiO_2 (standard deviation of 0.21 wt%) and the greatest maximum TiO_2 (2.18 wt%) of all clusters. Cluster 2 differs from Cluster 1 by a slightly greater mean abundance of Al_2O_3 (9.7 ± 0.1 wt%) and CaO (5.6 ± 0.1 wt%), and a lower abundance of MgO (Table 2). In total, 372 data points have a Cluster 2 membership across all localities. It is the largest cluster, comparable in size to Cluster 3 and is the most representative of the Greenheugh pediment average composition as it is situated at the focal composition for this locality (Fig. 10, 12).

The next closest cluster is Cluster 3 with a similarity to Clusters 1 and 2 of 28.3. Cluster 3 is differentiated by Clusters 1 and 2 by having on average higher abundances of SiO_2 (48.5 ± 0.2 wt%), Al_2O_3 (13.1 ± 0.1 wt%), CaO (6.0 ± 1.8 wt%), and lower abundances of FeO_T (18.7 ± 0.1 wt%) and MgO (6.5 ± 0.1 wt%). Cluster 3 has a total of 330 observation points with the majority situated on the Naukluft plateau (Fig. 10). Clusters 2 and 3 are the largest clusters in the dataset and as such are situated within the density contours of the Stimson bulk rock (Fig. 12). Similar to the results of Bedford et al. (2020a) for the main clusters 2 and 3, the standard deviations are higher than for the other clusters, which could indicate that some of the data points are not well bound to these clusters. However, the bimodal distribution of SiO_2 and Na_2O of the Naukluft plateau (Fig. 6), which contains the majority of Cluster 3 memberships, shows peak abundances of 45 wt% and 48 wt% SiO_2, and 2.7 wt% and 3.4 wt% Na_2O that align with the Clusters 2 and 3 averages, respectively. The variation of Al_2O_3 between the Emerson plateau and Greenheugh pediment localities that share a peak of 10 wt% Al_2O_3 also differs from the main peak composition for Al_2O_3 of the more Cluster 3-rich Naukluft plateau (13 wt%), suggesting a more bimodal distribution between all Stimson localities for this major element oxide. As such, this indicates that Clusters 2 and 3 are an inherent part of the dataset and accurately represent the most common sandstone components across all localities, despite the overlap of some points. Furthermore, as Clusters 2 and 3 derive from a total of 702 points, the overlap of <10 % of datapoints does not significantly skew the analysis of these two clusters.

The two most distinctive clusters are Clusters 4 and 5 (Fig. 9). Cluster 4 consists of 15 data points, distributed relatively equally between localities (four at Emerson, five at Naukluft, and six at Greenheugh, Fig. 10). Cluster 4 is defined as having the highest abundances of SiO_2 (54.50 ± 0.84 wt%), Al_2O_3 (17.97 ± 0.61 wt%), Na_2O (5.74 ± 0.34 wt%), and higher than average K_2O for the Stimson formation (0.97 ± 0.16 wt%). Cluster 5 only has five data points, one at the Emerson plateau and 4 in the Edinburgh interval of the Greenheugh capping unit and is defined by its high MnO concentration (2.92 ± 0.19 wt%) and high K_2O concentration similar

730 to Cluster 4 (1.0 ± 0.3 wt%). Aside from the MnO and K_2O concentration of Cluster 5, it is very
731 similar in composition to the MgO, FeO_T, and TiO_2-rich Clusters 1 and 2.

732 # 4 Discussion

733 ## *4.1 Geochemical variation associated with mineral sorting or sediment source*

734 The sedimentary architecture of the Stimson formation is interpreted as resembling dry
735 aeolian sand dunes (Banham et al., 2018, 2021, *this issue*). In a dry aeolian environment, the
736 coarsest and densest grains are rolled across the surface as they are transported by surface creep,
737 while the majority of sand-sized particles are temporarily lifted across the surface and
738 redeposited elsewhere as they travel via saltation. Meanwhile, grains finer than sand are
739 suspended in the wind. As such, mud to silt-sized grains and platy minerals such as
740 phyllosilicates are not likely to be deposited in a dry aeolian bedform (Kocurek et al., 2012),
741 supporting that the phyllosilicates at the Greenheugh capping unit are likely to be authigenic.
742 Sediments that are transported and deposited in dry aeolian environments are also subjected to
743 physical abrasion and less chemical weathering (Thomas et al., 2005). As such, sediment grains
744 that are less dense with a shape that is efficient at transportation by saltation or surface creep, and
745 that are resistant to physical weathering are more likely to be transported farther in a dry aeolian
746 environment and concentrated in distal deposits relative to those which do not meet these
747 criteria.

748 The geochemical trends of the majority of ChemCam data between mafic and felsic
749 minerals, and the similarity in composition between concretionary and non-concretionary
750 bedrock, also suggests that alteration was likely minimal away from the unconformity for the
751 Greenheugh pediment capping unit. Minimal alteration at Greenheugh is further supported by the
752 presence of 8 wt% olivine in the Edinburgh drilled sample (Rampe et al., 2020), which is only
753 slightly less than the olivine abundances for the active aeolian sands at the Bagnold Dunes (e.g.,
754 9.6 wt% at Ogunquit Beach) (Rampe et al., 2018). This, in addition to the low degree of
755 chemical weathering during transportation for dry aeolian systems (Jiang et al., 2019; Zhu et al.,
756 2009), suggests that the geochemistry of the Stimson formation at the Greenheugh pediment
757 capping unit is likely to be representative of the mineralogy of the dune sands at the time of
758 deposition.

759 ### *4.1.1. The relationship of the CheMin mineralogy to the ChemCam derived clusters*

760 The crystal chemistries of the Edinburgh sample are not yet available, so we will
761 compare our geochemical results to the crystal chemistries of the Big Sky drilled sample which
762 is considered the least affected by alteration of the Emerson and Naukluft bedrock samples (Yen
763 et al., 2017). As olivine is no longer present at the Emerson and Naukluft plateaus due to
764 diagenesis (Bedford et al., 2020a; Hausrath et al., 2018; Siebach et al., 2017), we use the olivine
765 crystal chemistry of the Gobabeb sample from the Bagnold dunes. (Achilles et al., 2017;
766 Morrison et al., 2018b). The primary igneous minerals present in the non-halo related drilled
767 samples Big Sky and Okoruso drilled at the Emerson and Naukluft plateaus respectively are
768 plagioclase feldspar (36.5 ± 1.8 wt% Big Sky, 27.2 ± 1.7 wt% Okoruso), K-feldspar (1.1 ± 0.6
769 wt% Big Sky, 1.9 ± 0.7 wt% Okuroso), and pyroxene (25.4 ± 2.3 wt% Big Sky, 20.7 ± 1.1 wt%
770 Okoruso) (Yen et al., 2017). The primary igneous minerals of the Edinburgh drilled sample from
771 the Greenheugh pediment capping unit also contains plagioclase feldspar (28.9 wt%), K-feldspar

(3.4 wt%), and pyroxene (20.2 wt%), in addition to olivine (8.4 wt%) (Rampe et al., 2020). On a plot of Al_2O_3 + Na_2O + K_2O versus MgO + FeO_T, all five clusters are situated along a trendline that extends from Stimson feldspar mineral endmembers (plagioclase feldspar and K-feldspar) in the top left of the plot, to mafic mineral endmembers (pyroxene and olivine) situated in the bottom right (Fig. 12A). Clusters 1 and 2, in addition to Cluster 5 are situated closer to the mafic mineral endmember of the plot. The Greenheugh pediment average composition is most similar to Cluster 2 (Fig. 11A). The geochemical composition of Cluster 2 also relates strongly to the lower SiO_2, Al_2O_3, Na_2O, and K_2O, and higher MgO dominant peak compositions of the Emerson plateau and Greenheugh capping unit compositions, and the lesser of the bimodal peak compositions for the Naukluft plateau (Fig. 6). This geochemical relationship of Cluster 2 with one of the bimodal peak compositions and greater chemical affinity to mafic minerals suggests a high proportion of mafic minerals and their diagenetic products being targeted by the ChemCam laser. Cluster 2 is most prevalent in the Greenheugh capping unit (55% total datapoints) followed by the Emerson plateau (46.2% total datapoints), with the fewest data at the Naukluft plateau (27.5% total data points; Fig. 10), supporting the greater influence of this cluster on the geochemical distribution present in the histograms.

Cluster 1 plots closer to the mafic mineral endmembers than Cluster 2 and likely represents a mixture of mafic minerals (Fig. 11A). Few observation points (n = 17) have Cluster 1 memberships suggesting that it is rare for the mafic end members to be targeted on their own, though it is present at each Stimson locality in relatively equal proportions (6 points at Emerson, 5 points at Naukluft, and 6 points at Greenheugh). An image analysis of Cluster 1 and 2 memberships (Fig. 13) show that Cluster 1 and 2 points likely relate to ChemCam targets that have sampled dark-toned and fine-grained parts of the sandstone. As such, the fine grain size and association of mafic minerals with the formation of the sandstone cement may have decreased the likelihood of a mafic endmember being targeted with the ChemCam laser, instead preferring the more mixed composition of Cluster 2.

The five ChemCam observation points with a Cluster 5 membership also show a geochemical composition which is closer towards the mafic mineral endmembers (Fig. 12A), but with high abundances of MnO (Fig. 11B). MnO can be present as a trace element in mafic minerals such as olivine and pyroxene, though not at the high abundances present in Cluster 5, suggesting that this cluster may relate to the local remobilization of Mn and Fe from mafic minerals that contain trace amounts of MnO in their crystal structure. As such, we interpret Clusters 1 and 2 as being indicative of the relative abundance of mafic minerals initially present within the deposited aeolian sands, a proportion of which was later altered to sandstone cement during early diagenesis, creating Cluster 5.

Clusters 3 and 4 are, in turn, situated closer to the feldspar mineralogical endmember, with Cluster 3 more representative of the geochemistries of the Emerson and Naukluft plateaus (Fig. 12A). Our Clusters 3 and 4 are geochemically similar to Clusters 3 and 5 of Bedford et al. (2020a) that were interpreted to represent more felsic minerals relative to mafic minerals and cement targeted by the ChemCam laser. The ChemCam RMIs show that the LIBS spots with Cluster 3 and 4 memberships have preferentially targeted light-toned mineral grains in the sandstone, further supporting a felsic nature for these clusters (Fig. 12B). Cluster 3 more strongly influences the bulk composition of the Emerson and Naukluft Stimson formation, skewing the focal composition away from Cluster 2 and causing a greater number of contour intervals to extend around the Cluster 3 composition (Fig. 11A). Looking at how the Cluster memberships

vary with location (Fig. 10), Cluster 3 is most abundant at the Naukluft plateau (n = 173), followed by the Emerson plateau (n = 101), with the lowest abundance of Cluster 3 present at the Greenheugh pediment capping unit (n = 56). The average composition of Cluster 3 also correlates to the peak composition of the Stimson formation that is situated at higher SiO_2, Al_2O_3, and Na_2O, and lower MgO and FeO_T, particularly at the Emerson plateau where Cluster 3 is most abundant (Fig. 6). As such, we interpret Clusters 3 and 4 as being representative of the proportion of felsic minerals that were present in the initially deposited Stimson aeolian sand dunes.

4.1.2. Implications for sediment sorting and provenance of the Stimson dune sands

Basaltic sediments transported in aeolian environments on Earth in localities such as the Dyngjusandur sand sheet, Iceland, are largely derived of volcanic glass, olivine, pyroxene, feldspar, and lithic grains (Baratoux et al., 2011; Cornwall et al., 2015; Mangold et al., 2011). These basaltic components are also present in the active aeolian sands on Mars, including those of the active Bagnold dune fields in Gale crater (Achilles et al., 2017; Lapotre et al., 2018; Rampe et al., 2018). Of these basaltic components, feldspar and augite are the least likely to be transported far as their cleavage planes and more tabular/elongate shapes make them both vulnerable to physical abrasion and less efficient at transportation by saltation and surface creep in aeolian environments (Baratoux et al., 2011; Cornwall et al., 2015; Mangold et al., 2011; Mountney et al., 2004). Olivine has a higher density (from forsterite at 3.29 g/cm^3 to fayalite at 4.39 g/cm^3) than most basaltic materials which could decrease the efficacy in which it can be transported far in aeolian settings, particularly at low wind speeds (Fedo et al., 2015). However, its similar Mohs hardness to quartz and concoidal fractures promoting rapid rounding of the olivine grains can make it more likely to persist in the aeolian transport of basaltic sands relative to feldspar and pyroxene, provided the sands are heterogeneous (Cornwall et al., 2015). The most resilient basaltic components in aeolian sediments are volcanic glass and polycrystalline basalt grains. Hence, if pyroxene and feldspar are present in distal aeolian sands they are likely entrained within polycrystalline basaltic grains (Cornwall et al., 2015). Geochemical trends relating to an increase in MgO downwind in the Dyngusandur sand sheet, Iceland, supports an increase in olivine minerals (Baratoux et al., 2011; Sara, 2017; Mangold et al., 2011).

The previous cluster analysis by Bedford et al. (2020a) hypothesized that physical grain segregation was the main cause of geochemical variation between the Emerson and Naukluft plateaus. In addition to the geochemical variation that related to mineralogical variation, a more local sand source for the Naukluft plateau was further supported by the presence of coarse feldspar grains which are less abundant at the Emerson plateau (Bedford et al., 2020a; Fig. 3d), and the geochemical results supported the interpretation of a southwest-northeast net sediment transport direction determined through cross-bed dip directions (Banham et al., 2018). The Greenheugh pediment capping unit has more MgO relative to the other Stimson localities (Fig. 6, 11), in addition to a greater abundance of Clusters 2 and 5 (Fig. 11), indicative of higher abundances of mafic minerals. This is supported by the mineralogical results from CheMin that show a relatively high concentration of olivine (Rampe et al., 2020), indicating that the Greenheugh capping unit may be enriched in mafic components as a result of mineral sorting during transportation assuming that the sands were derived from the same sediment source. If this is the case, the Greenheugh capping unit would have been deposited farther from the source than the Stimson formation at the Emerson and Naukluft plateaus that respectively show an increase in the felsic Clusters 3 and 4 (Fig. 10). Cross-set dip directions of the Stimson formation

at the Gleann Beag interval of the Greenheugh pediment shares the northeast dip direction of the cross-sets examined at the Emerson and Naukluft plateaus. However, the cross-set dip directions of the olivine-rich Edinburgh interval are indicative of an east-west net sediment transport direction, different to the southwest-northeast transport direction of the earlier Stimson localities and Gleann Beag interval (Banham et al., *this issue*). Cross-set dip directions in the Ladder interval show dip directions to the south, which indicates a sediment transport direction to the south. These variable dip directions show that the wind regime driving transportation at the time of deposition of the Greenheugh pediment was also variable (Banham et al., *this issue*), making the possibility of detecting geochemical variation relating to physical grain segregation with transportation more complex.

It is possible that sediment had accumulated down slope of the present-day pediment and was then remobilized after the sediment transport ratio changed, resulting in the reversal of the dune at the Ladder interval and the change in net sediment transport direction for the Edinburgh interval. This would maintain that the sediments at the pediment were transported farther from their source than those at the Emerson and Naukluft plateaus. Despite the variations in net sediment transport directions across the Greenheugh pediment intervals, the ChemCam data do not show a statistically significant difference in geochemistry for the major element oxides in these different stratigraphic intervals of the Greenheugh pediment capping unit away from the unconformity (Fig. 7). However, the grain size of the Stimson sandstone at the Greenheugh pediment capping unit is approximately the same as that of the Emerson plateau (Banham et al., *this issue*) which is not anticipated for a more distal deposit. Furthermore, the presence of pyroxene and feldspar within the Stimson sandstone of the Greenheugh capping unit suggests a relatively immature aeolian sandstone (Cornwall et al., 2015), supporting that the higher abundance of olivine at the Greenheugh pediment likely relates to an olivine-rich local sediment source, not transportation. In the ~10 km long Dyngjusandur sand sheet of Iceland, the mineralogy of the aeolian sediments show strong contributions from the source rocks of the surrounding volcanoes (Baratoux et al., 2011; Sara, 2017; Mountney et al., 2004). Feldspar grains are diverse in this sand sheet, representing several volcanic source rocks (Sara, 2017), and the incorporation of pumice into the northeast portion of the sand sheet from the 1875 eruptives of the nearby Askja volcano shows how readily aeolian processes can incorporate local bedrock materials (Baratoux et al., 2011; Sara, 2017; Mountney et al., 2004). As such, it is possible that the ~2.5 km distance that separates the Greenheugh pediment from the Emerson and Naukluft plateaus and the different wind regimes at the Greenheugh pediment were sufficient to result in a change in the main sediment source at that locality. We favor the hypothesis that a more olivine-rich sediment source is responsible for the geochemical difference of the Greenheugh pediment capping unit from that of the Emerson and Naukluft plateaus.

It is widely accepted that the present topographic expression of Mt Sharp formed as a result of aeolian erosion after the deposition and lithification of the Mt Sharp group (Day et al., 2016; Grotzinger et al., 2015; Steele et al., 2018). Orbital investigations of the units farther up the slopes of Mt Sharp show several olivine-bearing marker beds to the south and southeast of the Greenheugh capping unit (Rudolph et al., 2019). These marker beds could provide an adequate source for the olivine-rich sandstones preserved in the Greenheugh pediment capping unit, with the Stimson formation at the Emerson and Naukluft plateaus likely derived more from a Bradbury sandstone source (Bedford et al., 2020a).

4.2 The contribution of sediment recycling to the Stimson formation at the Greenheugh pediment

Sedimentological evidence for sediment recycling has been identified at several locations in Gale crater (Edgett et al., 2020) including the basal Stimson formation at the Marias Pass locality (Newsom et al., 2018). Several angular clasts are present in the basal Stimson formation at Marias Pass <4 mm wide, and decrease in abundance with stratigraphic height in the outcrop (Newsom et al., 2018). These angular clasts were interpreted as either a mixture of Murray mudstone intraclasts and calcium sulfate vein fragments or Murray clasts coated in calcium sulfate according to their largely CaO-rich geochemistry and light tonation (Newsom et al., 2018). Away from the unconformity, the geochemistry of the Stimson sandstone shared similarities to that of the basaltic sandstone from the Bradbury group, suggesting that they may either have been derived from a similar regional sediment source, or have been recycled from Bradbury group sandstones to the southwest of the Naukluft plateau (Bedford et al., 2020a).

Like the basal Stimson Missoula outcrop at Marias Pass, the basal Stimson targets of the Greenheugh pediment capping unit have a relatively lighter color compared to the overlying dark grey Stimson sandstone, and they contain some intraclasts (Fig. 13). However, there are some important differences in the physical and chemical properties between these units. First, the intraclasts are not as bright as those of the Missoula outcrop of Marias Pass, indicating that they may not have been overprinted by calcium sulfates to the same extent (Fig. 13D). Second, the underlying Carolyn Shoemaker formation is actually SiO_2-poor relative to average (Fig. 8) indicative of silica-remobilization, not precipitation like that which formed the silica-rich halos of the Emerson and Naukluft plateaus.

Although ChemCam did not directly analyze a mudstone intraclast at the Greenheugh pediment, it is possible that smaller grains of the Carolyn Shoemaker formation may have been recycled into the aeolian Stimson deposits (Fig. 13D; Banham et al., *this issue*), in addition to any diagenesis that could be the cause of the lighter color of the basal Stimson targets, complicating the geochemistry (Fig. 13A and 13B). To delineate the geochemical trends of diagenesis from those of sediment recycling of the underlying Murray formation into the aeolian deposits preserved at the Greenheugh pediment, we have generated mixing lines between the Carolyn Shoemaker formation and Stimson formation. Results show that at least four observation points from basal Stimson targets are situated within 1 standard deviation of the trendline indicative of mixing with between 50% to 90% of Carolyn Shoemaker bedrock (Fig. 13A and 13B). Looking at the post-ChemCam LIBS MAHLI image, the points with a more Shoemaker-like chemistry appear to have hit a greater proportion of light-toned angular grains. Four basal Stimson observation points have pure Stimson chemistries, and the rest of the basal Stimson observation points show geochemical signatures indicative of calcium sulfates. For the observation points that largely lie along the mixing line, they do show some depletions in Na_2O and K_2O relative to the trendline indicating that these points are not completely free of diagenetic overprint (see supplementary material S6). H is also elevated in these unconformity targets but is present at average Stimson values for the other Gleann Beag interval ChemCam targets above the basal Stimson targets (Fig. 9). This indicates that Carolyn Shoemaker grains were incorporated into the basal Stimson formation at the Greenheugh pediment which was later subjected to diagenetic fluids that remobilized the alkali elements, and precipitated calcium sulfate cement and iron oxides.

Mt Sharp group mudstone intraclasts preserved at the base of the Stimson formation at Marias Pass and the Greenheugh pediment supports that sediment recycling of the immediately underlying bedrock occurred. Due to grains finer than fine sand being winnowed away in dry aeolian environments and transported in suspension, it is possible that the lacustrine mudstone of the Mt Sharp group was rapidly abraded and transported away from the Stimson sand dunes which is why geochemical signatures of the Mt Sharp group are not preserved far from the unconformity. The sorting of fine-grained volcaniclastic material from basaltic sand grains in aeolian bedforms is seen in fluvio-aeolian sedimentary systems in Iceland, where fine-grained palagonite tuff is not preserved in the well-sorted aeolian ripples, but is present in the proximal fluvial deposits (Bedford et al., 2020b), supporting the hypothesis that grain size is likely a factor in the Mt Sharp group mudstone's preservation in the Stimson formation.

4.3 Aqueous alteration and cementation of the Stimson formation at the Greenheugh pediment.

4.3.1 Lithification of the Stimson formation and early diagenesis

The Stimson sand sea was likely a dry aeolian deposit (Banham et al., 2021), so the first measurable instance of water-sediment interaction would have occurred after deposition of the dune sands, during the interaction of the sediments with the cementing fluid which lithified the formation in what we define as the early stage diagenesis. In this section, we will discuss whether this cement-forming diagenesis occurred at the same time under the same conditions across all localities through a comparison of the mineralogy of Thorpe et al. (*this issue*) and ChemCam geochemistry.

The secondary minerals present in the non-halo Big Sky and Okoruso drill samples, drilled at the Emerson and Naukluft plateaus respectively, include iron oxides magnetite (10.3 ± 0.6 wt% in Big Sky, 11.2 ± 0.7 wt% in Okoruso) and hematite (3.0 ± 0.5 wt% in Big Sky, 0.7 ± 0.4 wt% in Okoruso), and minor (<2 wt%) abundances of calcium sulfates, quartz, and fluorapatite (Morrison et al., 2018; Yen et al., 2017). Both the Emerson and Naukluft plateaus also contain 15-20 wt% of an X-ray amorphous component with a moderate SiO_2 and FeO_T composition for Gale crater which likely formed from the aqueous alteration of basaltic sediments (Smith et al., 2021). Secondary minerals at the Greenheugh pediment capping unit include magnetite (10 wt%), hematite (0.4 wt%) and phyllosilicates (7 ± 3 wt%), and 20 wt% amorphous component (Rampe et al., 2020). When comparing the mineralogy of these sandstones to the ChemCam data, the secondary minerals and amorphous component that derive the diagenetic cement were hypothesized in Bedford et al. (2020a) to have contributed to the FeO_T- and MgO-rich Clusters 1 and 2, and the TiO_2-rich Cluster 4 of that study. As the MgO geochemistry of the Stimson formation at these sites is similar to that of the olivine-bearing active Bagnold dune sands and the chemistry of the bedrock comprised of small concretions is indistinguishable from non-concretionary bedrock, it was hypothesized that the cement forming diagenesis at these Stimson localities was extensive enough to convert all olivine to diagenetic cement, but was relatively isochemical, preserving the geochemical trends that related to mineral sorting in the ancient dune field and sediment source characteristics (Fig. 11; Bedford et al., 2020a). Similar to the results of Bedford et al. (2020a), our cluster analysis, which now includes the Greenheugh capping unit and MnO data, shows MgO- and FeO_T-rich Clusters 1 and 2, respectively. These clusters are compositionally equivalent to Clusters 1 and 2 of Bedford et al. (2020a) with the exception of SiO_2 that is on-average ~4 wt% lower and Al_2O_3 which is ~2 wt%

lower in the new clusters, likely a result of the higher abundance of mafic minerals at the Stimson formation at the Greenheugh capping unit, but not at the Emerson and Naukluft plateaus. This similarity in composition of the new Stimson Clusters 1 and 2 to the old ones maintains that Clusters 1 and 2 are compositionally representative of the primary igneous mineralogy of the pre-lithified sands that is present across all localities, even though the secondary alteration minerals and amorphous component composition varies.

Hydrous alteration modelling of the Stimson formation at the Emerson and Naukluft plateaus suggests that the sandstone cement which contains the secondary minerals and amorphous component primarily formed through the dissolution of olivine under slightly acidic to near neutral pH conditions (pH 6–8) during burial diagenesis (Hausrath et al., 2018). The pH was largely constrained by the presence of abundant magnetite (10.3 wt%) as a lower pH would inhibit the precipitation of authigenic magnetite (Hausrath et al., 2018). The similar abundance of magnetite to the Emerson and Naukluft plateaus further suggests that olivine at the Greenheugh capping unit also underwent dissolution at a pH > 6 to precipitate magnetite, which given that 8 wt% olivine is still present at the Greenheugh pediment, indicates a much higher abundance of olivine in the originally deposited aeolian sands (Rampe et al., 2020). Furthermore, as olivine is one of the most reactive basaltic minerals, particularly in aqueous fluids with a pH <8 (Babechuk et al., 2014; Eggleton et al., 1987; Nesbitt et al., 1992; Pokrovsky et al., 2000), the high abundance of olivine in the sandstone of the Greenheugh pediment capping suggests that this sandstone has undergone less interaction with diagenetic fluids than the Stimson formation at the Emerson and Naukluft plateaus.

The presence of 7 wt% phyllosilicates at the Greenheugh pediment and none detected at the Emerson and Naukluft plateaus further suggests that the early diagenetic conditions may have been slightly different at this locality even though the clusters are compositionally equivalent. Magnetite (4.3–11.3 wt%), phyllosilicates (10–22 wt%), and olivine (1.8–4.9 wt%) have been detected in the Bradbury group basaltic fluviolacustrine deposits, the John Klein and Cumberland drilled samples of the Yellowknife Bay mudstones (Vaniman et al., 2014), and the Windjana drilled sample of the Kimberley formation (Treiman et al., 2016). Hydrous alteration modelling of the formation conditions of the phyllosilicates at Yellowknife Bay by Bridges et al. (2015) suggests that these phyllosilicates formed through an inhomogeneous dissolution of ~70 wt% amorphous component, ~20 wt% olivine, and 10 wt% host rock in an open-system with a neutral to alkaline fluid at a pH 7.5–12. A comparison of the Stimson formation sandstone geochemistry to that of the Yellowknife Bay mudstone and sandstone showed that they are both basaltic and likely derived from a similar sediment provenance (Bedford et al., 2020a), as such, the modelling results of Bridges et al. (2015) are applicable to the Stimson formation. Thereby, the formation of the phyllosilicates at the Greenheugh capping unit likely occurred under more alkaline conditions (pH 7.5–12) compared to the early diagenetic conditions of the Emerson and Naukluft plateaus (pH 6–8; Hausrath et al., 2018).

In the ChemCam data, H can be used to trace the abundance of hydrated phases such as phyllosilicates across sedimentary units (Thomas et al., 2020). H at the Greenheugh capping unit is notably bimodal at H peak abundances of 0.003 and 0.005 (Fig. 6, 7). The Edinburgh and Ladder intervals of the Greenheugh pediment capping derive the higher H values (0.005), supporting the presence of phyllosilicates in these stratigraphic units. Meanwhile, the lower H value at the Greenheugh capping unit consists of data solely within the Glean Beag interval and is equivalent to the peak H value at the Emerson and Naukluft plateaus (0.003), suggesting

minimal phyllosilicates. This indicates that the phyllosilicates are stratigraphically confined to the Edinburgh and Ladder intervals (Fig. 8) which could result from spatial diagenetic variability in the Stimson formation at the Greenheugh capping unit relative to the unconformity. This spatial variability in phyllosilicate abundances with the unconformity is also present in the underlying Carolyn Shoemaker formation, which has less phyllosilicates in the Hutton drilled sample compared to other drill holes away from the unconformity (Thorpe et al., *this issue*).

Evidence to support spatial diagenetic variability in the Stimson formation is present with the distribution of the concretions. On average, concretions are more abundant and greater in size with proximity to the unconformity for the Stimson formation at the Greenheugh pediment (Fig. 5), and elsewhere (Banham et al., 2018, *this issue*). This relationship of the concretions with the unconformity suggests that their formation may relate to the presence of a perched aquifer at the base of the Stimson formation, or that it could indicate a greater abundance of minerals that acted as a nucleus for concretion formation (Banham et al., 2018; Chan et al., 2012; Potter-McIntyre et al., 2014). With the exception of the basal Stimson formation that includes mixing of mudstone intraclasts and alteration by a later diagenetic fluid, the Stimson formation is relatively geochemically uniform (Bedford et al., 2020a; Siebach et al., 2017; Thompson et al., *this issue*), with large-scale variations only relating to late-stage diagenetic features (Bedford et al., 2020a; Yen et al., 2017). As such, a greater concentration of minerals at the unconformity for which these concretions could have nucleated seems unlikely. However, the Mt Sharp group units that underly the Stimson formation are well-cemented, phyllosilicate-bearing mudstones which makes them more likely to act as an aquiclude and promote the formation of a perched aquifer which in turn promoted the formation of the concretions. If the perched aquifer is the cause of the concretion formation, this would in turn support that the diagenetic fluids responsible for cementing the Stimson formation were derived from near-surface waters that accumulated towards the unconformity. The Greenheugh pediment is fan shaped and extends from Gediz Vallis whose morphology suggests that it may have formed from fluvial processes (Anderson et al., 2010; Thomson et al., 2011; Wiens et al., 2020), providing a potential source for the surficial water that lithified the Stimson formation at the Greenheugh pediment and potentially further downslope.

With the addition of MnO data to the Stimson formation and, therefore, the cluster analysis, there is now a MnO-rich Cluster 5 that consists of high-MnO observation points (mean of 2.9 wt%) from three host rock ChemCam targets from the Edinburgh interval of the Greenheugh pediment capping unit (Fig. 13B). Additional MnO-rich host rock targets in the Edinburgh interval are also present for observation points that have ChemCam totals <90 wt% that are excluded from the cluster analysis. The ChemCam observation points with high-MnO concentrations targeted fine grained, dark-toned sandstone that is not associated with any obvious feature and are sporadically distributed spatially across the sandstone. MnO concentrations are >1 wt% for these data points and there are no correlations with other major element oxides. Similar observations of sporadic enrichments in MnO were detected in the Glenelg and Gillespie Lake sandstones of the aforementioned Yellowknife Bay formation (Lanza et al., 2014); note that these Mn abundances were later recalibrated (Gasda et al., 2021). The cause of these high MnO-points were hypothesized to be either detrital, from a sediment source that experienced oxidizing aqueous conditions, or diagenetic, either forming during rapidly oxidizing, but localized conditions during lithification of the sandstones, or from later diagenetic fluids moving through the sandstones (Lanza et al., 2014). As the Greenheugh capping unit has

minimal evidence for late diagenesis, unlike the older sedimentary units of Yellowknife Bay, it is most likely to be detrital or formed during cementation. Mn is a common trace element in olivine, substituting for Fe^{2+}. As such, the dissolution of olivine and formation of magnetite under isochemical conditions may have precipitated a late-stage Mn-bearing mineral or amorphous component if aqueous fluids were minimal and the system was closed at the scale of the stratigraphic interval.

4.3.2. The formation of alteration features across the Stimson formation

Based on the Mastcam and Navcam images of the Stimson formation at the Greenheugh capping unit (Fig. 3, 4), in addition to the plots of data classifications across all Stimson localities (Fig. 5), it is evident that the Stimson formation at the Greenheugh pediment has not experienced the same later diagenetic events as those at the Emerson and Naukluft plateaus. The Greenheugh pediment lacks silica-rich halos, raised ridges, and has very few occurrences of calcium sulfate mineral veins which are much thinner than those sampled and studied at the Emerson and Naukluft plateaus (Fig. 4). Erosionally resistant polygons - polygonal diagenetic features associated with preferential cementation around fractures as a result of groundwater recharge - are also present to a lesser degree at the Greenheugh capping unit compared to the other Stimson localities and with a different morphology (Kronyak et al., 2019b).

The lack of fractures and their associated diagenetic features, in addition to the different morphology of erosion resistant polygonal ridges at the Greenheugh pediment capping unit suggests different potential scenarios: 1) that at this location, groundwater flow was not as pervasive (Kronyak et al., 2019b), 2) that the Stimson formation at the Greenheugh capping unit experienced less compaction compared to that at the Emerson and Naukluft plateaus, or 3) that the Greenheugh pediment exhibits different material properties such as rock hardness and grain size. The Greenheugh pediment is situated at an elevation of -4150 m, which is 200 m higher in elevation than the Stimson formation at the Emerson and Naukluft plateaus (Fig. 1,2). As water is most likely to collect at topographical lows, it is possible that there was less groundwater available to the Greenheugh pediment to either create the well-formed, large polygons of the Emerson and Naukluft plateaus, or to generate sufficient fluid overpressure and hydrofracturing, providing support to scenario 1.

Another factor which may have impacted the amount of groundwater available to the Greenheugh pediment capping unit is the time in which it was deposited and lithified. Although the Stimson formation at the pediment shares the common sedimentary architecture of the Stimson formation investigated earlier in the mission, and all outcrops are situated above the basal Siccar Point group unconformity, it is not clear whether these outcrops were lithified at the same time. While the sedimentary architecture indicates sediment accumulation under arid conditions (hence the absence of damp interdunes), water would have percolated through the sediments post-deposition to cement the strata. This could have happened at depth where subsurface water could not interact with the depositional surface (sensu Kocurek and Haveholm. 1993) or could have happened after the terminal phase of the dune field's evolution. The sources of cementing fluid are likely to be different between the earlier Stimson localities and the Greenheugh pediment based on the different secondary minerals. The fan-shaped morphology of the Greenheugh pediment itself at the base of Gediz Vallis suggests that it may relate to surface waters flowing down and eroding the slope of Mt Sharp (Bryk et al., 2019). Meanwhile, the Stimson formation at the Emerson and Naukluft plateaus may have been cemented by rising

groundwaters (Banham et al., 2018). Hence, the Greenheugh pediment capping unit may have been cemented at a different time, potentially one in which there was less groundwater availability in Gale crater.

Alternatively, the difference in elevation could have resulted in less overburden to compact the sediments at the Greenheugh pediment capping unit, supporting scenario 2, however, it is not known to what extent the Stimson formation was buried at either location. Several sedimentary float are present on top of and close the Stimson formation at the Emerson and Naukluft plateaus (Wiens et al., 2020). Some of these float potentially include clasts of Stimson bedrock and their location on top of the Stimson formation itself suggests that additional sedimentary units did at some time overlie the Stimson formation at these localities in the past (Wiens et al., 2020). But as these deposits exist as float and not as a coherent outcrop, we cannot constrain with any certainty how much burial, and therefore compaction, occurred for the Stimson formation at the Emerson and Naukluft plateaus relative to the Greenheugh capping unit.

4.3.3. Diagenesis at the unconformity

Changes in geochemistry and mineralogy in the underlying Mt Sharp group and immediately overlying Stimson formation have been detected along the basal Siccar Point group unconformity indicating that this geological boundary may have provided a conduit for later diagenetic fluids (Achilles et al., 2020; Horgan et al., 2020; Newsom et al., 2018; Rudolph et al., *this issue*; Thomson et al., *this issue*; Yen et al., 2021). At the Greenheugh pediment, Stimson and Carolyn Shoemaker bedrock close to the unconformity exhibit differences in geochemistry, and for the Carolyn Shoemaker formation mineralogy (Dehouck et al., *this issue*; Thompson et al., *this issue*; Thorpe et al., *this issue*). The basal Stimson formation is lower in MgO, Na_2O, and MnO relative to the mean composition of the Stimson formation, low in total sum of oxides, but high in CaO and H relative to the average Stimson formation (Fig. 7). The high CaO, H, and low totals are indicative of calcium sulfate addition, which is also supported by the mixing plots (Fig. 13, S.6), and the high abundance of sulfates detected by APXS (Thompson et al., *this issue*). As this unique Stimson geochemistry is only observed for targets that are approximately 10 cm and 50 cm from the unconformity surface, it suggests that this diagenesis did not permeate far into the overlying Stimson formation, indicating that it was lithified prior to the alteration.

Calcium sulfate cements were also identified in the basal Stimson outcrop of the Marias Pass locality according to a lighter coloration of the bedrock and geochemical compositions that are high in CaO and low for all other major element oxides and totals (Newsom et al., 2018). At the Naukluft plateau, rover images also showed evidence of either silica-halo alteration or calcium sulfates concentrated at the Murray formation immediately below the unconformity (Fig. 14). This indicates that the diagenesis that occurred at the unconformity between the Greenheugh pediment capping unit was widespread and also occurred along the unconformity at other Stimson localities.

A possible scenario that could result in the precipitation of calcium sulfates and a decrease in MgO and alkali abundances includes acid-sulfate alteration, such as that which is hypothesized for the Murray formation of Marias Pass, the Oudam drilled sample in the Murray formation at the Naukluft plateau (Achilles et al., 2020), the alteration halos of the Emerson and Naukluft Plateaus (Hausrath et al., 2018; Yen et al., 2017, 2021), and in some places on Vera

Rubin ridge (Rampe et al., 2020b). Acid-sulfate alteration can preferentially alter phenocrysts such as olivine, pyroxene, and feldspars over volcanic glass, leaving behind a silica residue, iron oxides, and sulfates and remobilizing MgO and the alkali elements (McCollom, et al., 2013a; McCollom et al., 2013b; Tosca et al., 2004). However, unlike the potentially acid-sulfate altered mudstones and sandstones of Marias Pass, the basal Stimson formation at the Greenheugh capping unit does not have an enrichment in SiO_2 and TiO_2 (Fig. 7), indicating that any acid-sulfate alteration at this locality may have been less extensive than that which modified the geochemistry and mineralogy of the rocks at the Emerson and Naukluft plateaus.

vThe alteration of Stimson sandstones at the unconformity suggests that either a weakly oxic, sulfate-bearing fluid or fewer resurgences of late diagenetic sulfate-bearing groundwater fluids may have migrated along the unconformity, permeating the lithified sandstone directly above and the mudstone below. These fluids may have not been able to permeate as extensively into the upper Stimson formation at the Greenheugh capping unit and create polygonal fractures due to the greater elevation resulting in less groundwater availability. The difference in sandstone cement between the Emerson and Naukluft plateaus and the Greenheugh pediment capping unit may have also been a factor in impeding the formation of polygons and decreasing the permeability of the Stimson sandstone at the Greenheugh capping unit. The Big Sky and Okoruso drilled samples of the Emerson and Naukluft plateaus both contain iron oxides (magnetite and hematite), some calcium sulfates (bassanite), and an amorphous component within the sandstone cement (Yen et al., 2017). The Edinburgh drilled sample from the Edinburgh interval of the Greenheugh pediment capping unit contains phyllosilicates in addition to magnetite and an amorphous component (Rampe et al., 2020). Phyllosilicates decrease the permeability of a sandstone, which may have further impacted fluid migration at this locality and the material properties of the Stimson formation at the Edinburgh interval compared to that at the Emerson and Naukluft plateaus.

The Carolyn Shoemaker formation that underlies the unconformity at the Greenheugh pediment shows geochemical differences relative to the average Carolyn Shoemaker formation that are indicative of alteration (Fig. 7, 13; Dehouck et al., *this issue*; Gasda et al., *this issue*). Furthermore, the Hutton drill location in the Carolyn Shoemaker formation contains 8.7 wt% iron oxides, 4.7 wt% cristobalite and 5.2 wt% Opal-CT, silica polymorphs that can form as a result of the dissolution of mafic minerals (Thorpe et al., *this issue*). The immediately underlying Carolyn Shoemaker bedrock around the Hutton drill site is lower in oxide totals (94.9 wt% compared to 97.3 wt%), and higher in CaO compared to average Carolyn Shoemaker bedrock (Fig. 7). This can be indicative of calcium sulfate cement which has been largely detected by the ChemCam instrument and correlated to light-toned cements in MAHLI images acquired in the traverse leading up to the Greenheugh pediment (Gasda et al., *this issue*; Nellesson et al., 2021). However, the mineralogy of the Hutton drilled sample acquired below the capping unit only contains 0.6 wt% anhydrite (Thorpe et al., *this issue*), which is some of the lowest abundances of crystalline calcium sulfate detected in the Carolyn Shoemaker formation since the drilled samples of the Pahrump Hills (Rampe et al., 2017), and sulfur is not detected here with APXS (Thompson et al., *this issue*). F abundances also increase in the Carolyn Shoemaker formation below the unconformity at the Hutton drill site (Dehouck et al., *this issue*; Fig. 8B), including for alteration features such as veins and raised ridges (Gasda et al., *this issue*). This correlated with the increase in CaO concentrations suggesting the presence of fluorapatite which is confirmed in the CheMin results of the Hutton drilled sample (Thorpe et al., *this issue*).

The current hypothesis for the distinctive geochemistry and mineralogy of the Hutton drill hole and surrounding sediments is that warm or acidic diagenetic fluids circulated here and concentrated below the capping unit (Dehouck et al., *this issue*; Gasda et al., *this issue*; Forni et al., 2021; 2016). However, these F-rich diagenetic fluids do not appear to have permeated into the overlying Stimson formation. Fluorine is a fluid-mobile element which is in high abundance in the Murray formation bedrock and diagenetic features below the Stimson formation at the Marias Pass locality and in the Carolyn Shoemaker formation's Hutton Zone of Glen Torridon (Forni et al., 2021; 2016). However, above the unconformity, fluorine detections are sparse in the Stimson formation, with only one detection in the pediment capping unit (Fig. 8B; Forni et al., 2021). Meanwhile, the rare detections of fluorine in the Stimson sandstone instead suggests that these may instead relate to detrital phases, similar to what is hypothesized for the fluorine phases detected in the Bradbury group sandstones (Forni et al., 2013). The lack of fluorine detected in the basal Stimson that also contains intraclasts of the underlying mudstones further supports that the alteration of the Carolyn Shoemaker formation around the Hutton drill hole occurred after the formation of the overlying Stimson formation.

5 Conclusions

The ChemCam geochemical data of the Greenheugh pediment capping unit suggests that this unit is a part of the Stimson formation investigated at the Emerson plateau, Naukluft plateau, and Murray Buttes localities. However, minor but statistically significant geochemical variations exist for SiO_2, MgO, MnO, Al_2O_3, and Na_2O. These slight geochemical differences are indicative of higher abundances of mafic minerals and their diagenetic products at the Stimson formation of the Greenheugh capping unit, which is supported by mineralogical data from CheMin. The higher abundance of mafic minerals preserved at the Greenheugh pediment capping unit is unlikely to relate to physical grain segregation with transportation across all Stimson localities due to variable cross-set dip directions indicative of seasonal wind variations which complicate the geochemical record of net sediment transport at this locality. Similarities in grain size and the high abundances of pyroxene and plagioclase feldspar in addition to olivine is also indicative that this aeolian sandstone has not undergone significant transport from its source (Cornwall et al., 2015). Instead, we hypothesize that the sediments of the Stimson formation at the Greenheugh pediment capping unit are predominately sourced from a nearby olivine-rich unit which may relate to the olivine-bearing marker beds that have been detected close to the pediment, farther up the slopes of Mt Sharp (Rudolph et al., 2019).

While the Stimson aeolian sand dunes migrated in the Hesperian, they were also able to erode and incorporate clasts from the underlying Mt Sharp group into the base of the sand dunes, evidenced by the ChemCam geochemical data and images of the basal Stimson unit at the Greenheugh pediment. However, due to the fine-grained nature of the Mt Sharp group mudstones, it is unlikely that mudstones were preserved for long in the Stimson sand dunes and were instead winnowed away into suspension during dune migration. Alternatively, the intraclasts within the basal Stimson formation may relate to the onset of aeolian deposition as a buried lag deposit, similar to what is hypothesized for the Murray intraclasts preserved in the Stimson formation at Marias Pass (Newsom et al., 2018). Either scenario provides additional evidence for sediment recycling in Gale crater by aeolian processes.

After the deposition of the Stimson sand dunes, their sediments interacted with surface waters forming a sandstone cement through the dissolution of the most reactive components,

likely volcanic glass and olivine. These fluids formed a perched acquifer at the base of the aeolian sandstone at all localities, forming the concretionary bedrock. Geochemically, the sandstone cement of the Stimson formation is difficult to distinguish from that of the Emerson and Naukluft plateaus with the exception of MnO, however, differences in secondary mineralogy and the persistence of olivine in the Greenheugh pediment capping unit suggest that the early diagenetic fluid was more alkaline than that which cemented the Stimson formation at other localities. This difference in early diagenetic fluid chemistry could relate to the Greenheugh pediment capping unit having a different fluid source, and/or being cemented at a different time in the geological record of the Stimson sand sea.

Once the Stimson formation was lithified, several diagenetic events likely relating to upwelling groundwater occurred to form erosion resistant polygons, silica-rich halos, calcium sulfate veins, and alteration along the unconformity. These later diagenetic events were more prevalent in the Stimson formation preserved at the Emerson and Naukluft plateaus, suggesting a greater availability of groundwater fluids at these sites than the Greenheugh pediment. This greater availability of groundwater at the Emerson and Naukluft plateaus could relate to their lower elevation in Gale crater, greater burial, or a difference in age between these Stimson deposits (i.e., Emerson and Naukluft Stimson are older than the Greenheugh capping unit and were cemented at a time when there was more groundwater present in Gale crater). One of the last episodes of diagenesis to occur likely relates to the unconformity, which is shared across all localities. The diagenesis below the unconformity involved fluorine-rich, potentially warm fluids that did not permeate into the overlying Stimson formation. The diagenesis along the unconformity suggests that acidic, sulfate-bearing fluids migrated along the unconformity and altered the basal Stimson formation, supporting the hypotheses of previous studies.

Overall, the ancient aeolian environment under which these Stimson sandstones were deposited was dynamic, recycling nearby material as the dunes migrated across the surface. These results support that liquid water was stable at the surface in the Hesperian and was available as groundwater for multiple diagenetic events after deposition along bedrock weaknesses and the basal Stimson formation in Gale crater.

Acknowledgments, Samples, and Data

CCB acknowledges support from the LPI. JCB, SPS, and SMRT acknowledge funding from UKSA. JF acknowledges the support from the Carlsberg Foundation. The MSL engineering, ChemCam, CheMin, and science teams are gratefully acknowledged for the acquisition of the data used in this paper. Support for this work in the US is provided by the NASA Mars Exploration Program and in France by CNES. Mastcam mosaics were processed by the Mastcam team at Malin Space Science Systems.

The ChemCam major element oxide data and RMI data presented in this paper are archived in the Planetary Data System (PDS). The geochemical data can be found at Wiens (2013a). RMI mosaics can be found at Wiens (2013b). The derived data which includes the ChemCam targets used in the study, target classifications, and clustering results, can be found at Bedford (2022).

References

Achilles, C. N., Downs, R. T., Ming, D. W., Rampe, E. B., Morris, R. V., Treiman, A. H., et al. (2017). Mineralogy of an active eolian sediment from the Namib dune, Gale crater, Mars. *Journal of Geophysical Research: Planets*, *122*(11), 2344–2361. https://doi.org/10.1002/2017JE005262

Achilles, C. N., Rampe, E. B., Downs, R. T., Bristow, T. F., Ming, D. W., Morris, R. V., et al. (2020). Evidence for Multiple Diagenetic Episodes in Ancient Fluvial-Lacustrine Sedimentary Rocks in Gale Crater, Mars. *Journal of Geophysical Research: Planets*, *125*(8). https://doi.org/10.1029/2019JE006295

Anderson, R. B., & Bell III, J. F. (2010). Geologic mapping and characterization of Gale crater and implications for its potential as a Mars Science Laboratory landing site. *The Mars Journal*, *5*, 76–128. https://doi.org/10.1555/mars.2010.0004

Anderson, R. B., Bridges, J. C., Williams, A., Edgar, L., Ollila, A., Williams, J., et al. (2015). ChemCam results from the Shaler outcrop in Gale crater, Mars. *Icarus*, *249*, 2–21. https://doi.org/10.1016/j.icarus.2014.07.025

Anderson, R. B., Clegg, S. M., Frydenvang, J., Wiens, R. C., McLennan, S., Morris, R. V., et al. (2017). Improved accuracy in quantitative laser-induced breakdown spectroscopy using sub-models. *Spectrochimica Acta Part B: Atomic Spectroscopy*, *129*, 49–57. https://doi.org/10.1016/J.SAB.2016.12.002

Anderson, R. B., Edgar, L. A., Rubin, D. M., Lewis, K. W., & Newman, C. (2018). Complex bedding geometry in the upper portion of Aeolis Mons, Gale crater, Mars. *Icarus*, *314*, 246–264. https://doi.org/10.1016/j.icarus.2018.06.009

Babechuk, M. G., Widdowson, M., & Kamber, B. S. (2014). Quantifying chemical weathering intensity and trace element release from two contrasting basalt profiles, Deccan Traps, India. *Chemical Geology*, *363*, 56–75. https://doi.org/https://doi.org/10.1016/j.chemgeo.2013.10.027

Banham, S. G., Gupta, S., Rubin, D. M., Edgett, K. S., Bryk, A. B., Dietrich, W. E., et al. (this issue). Reconstructing ancient sedimentary environments of the Greenheugh pediment capping unit (Stimson formation) and its implications for Gale crater evolution. *JGR: Planets*.

Banham, S. G., Gupta, S., Rubin, D. M., Watkins, J. A., Sumner, D. Y., Edgett, K. S., et al. (2018). Ancient Martian aeolian processes and palaeomorphology reconstructed from the Stimson formation on the lower slope of Aeolis Mons, Gale crater, Mars. *Sedimentology*, *65*(4), 993–1042. https://doi.org/10.1111/sed.12469

Banham, S. G., Gupta, S., Rubin, D. M., Edgett, K. S., Barnes, R., Van Beek, J., et al. (2021). A Rock Record of Complex Aeolian Bedforms in a Hesperian Desert Landscape: the Stimson formation as exposed in the Murray buttes, Gale crater, Mars. *Journal of Geophysical Research: Planets*, *126*(4), e2020JE006554. https://doi.org/10.1029/2020je006554

Baratoux, D., Mangold, N., Arnalds, O., Bardintzeff, J.-M., Platevoët, B., Grégoire, M., & Pinet, P. (2011). Volcanic sands of Iceland - Diverse origins of aeolian sand deposits revealed at Dyngjusandur and Lambahraun. *Earth Surface Processes and Landforms*, *36*(13), 1789–1808. https://doi.org/10.1002/esp.2201

1343 Bedford, C. C. (2019, July 28). *Distinguishing The Geochemical Effects Of Sedimentary*
1344 *Processes And Source Region Characteristics In Gale Crater, Mars.*

1345 Bedford, C. C., Bridges, J. C., Schwenzer, S. P., Wiens, R. C., Rampe, E. B., Frydenvang, J., &
1346 Gasda, P. J. (2019). Alteration trends and geochemical source region characteristics
1347 preserved in the fluviolacustrine sedimentary record of Gale crater, Mars. *Geochimica et*
1348 *Cosmochimica Acta*, *246*. https://doi.org/10.1016/j.gca.2018.11.031

1349 Bedford, C. C., Schwenzer, S. P., Bridges, J. C., Banham, S. G., Wiens, R. C., Frydenvang, J., et
1350 al. (2019). Using ChemCam derived geochemistry to identify the paleonet sediment
1351 transport direction and source region characteristics of the Stimson formation in Gale crater,
1352 Mars. Retrieved from
1353 https%3A%2F%2Fwww.hou.usra.edu%2Fmeetings%2Flpsc2019%2F

1354 Bedford, C. C., Schwenzer, S. P., Bridges, J. C., Banham, S., Wiens, R. C., Gasnault, O., et al.
1355 (2020a). Geochemical variation in the Stimson formation of Gale crater: Provenance,
1356 mineral sorting, and a comparison with modern Martian dunes. *Icarus*, *341*, 113622.
1357 https://doi.org/10.1016/j.icarus.2020.113622

1358 Bedford, C. C., Rampe, E. B., Thorpe, M., Ewing, R. C., Horgan, B., Nachon, M., et al. (2020b).
1359 Identifying the products of volcano-ice interaction in basaltic sediments in Iceland and their
1360 implications for Mars. In *51st Lunar and Planetary Science Conference* (p. 2478). Houston.

1361 Bedford, C. (2022). Greenheugh capping unit ChemCam derived data products [Data set].
1362 Zenodo. https://doi.org/10.5281/ZENODO.5889318

1363 Bennett, K. A., & Bell, J. F. (2016). A global survey of martian central mounds: Central mounds
1364 as remnants of previously more extensive large-scale sedimentary deposits. *Icarus*, *264*,
1365 331–341. https://doi.org/10.1016/j.icarus.2015.09.041

1366 Bennett, K. A., Fox, V. Bryk, A. Dietrich, W. Fedo, C. Dehouck, E. Cousin, A. Thorpe, M.
1367 Rudolph, A. Horgan, B. Gasda, P. Bristow, T. Sutter, B. McAdam, A. O'Connell-Cooper, C.
1368 Thompson, L. Fraeman, A. Vasavada, A. Wong, G. Banham, S. Arvidson, R. Stack, K.
1369 Frydenvang, J. Edgar, L. Treiman, A. Eigenbrode, J. Grotzinger, J. (this issue). An
1370 overview of the Curiosity rover's Campaign in Glan Torridon, Gale crater, Mars. *JGR:*
1371 *Planets.*

1372 Bish, D. L., Blake, D. F., Vaniman, D. T., Chipera, S. J., Morris, R. V., Ming, D. W., et al.
1373 (2013). X-ray Diffraction Results from Mars Science Laboratory: Mineralogy of Rocknest
1374 at Gale Crater. *Science*, *341*(6153), 1238932–1238932.
1375 https://doi.org/10.1126/science.1238932

1376 Blake, D., Vaniman, D., Achilles, C., Anderson, R., Bish, D., Bristow, T., et al. (2012).
1377 Characterization and Calibration of the CheMin Mineralogical Instrument on Mars Science
1378 Laboratory. *Space Science Reviews*, *170*(1–4), 341–399. https://doi.org/10.1007/s11214-
1379 012-9905-1

1380 Blake, D. F., Morris, R. V., Kocurek, G., Morrison, S. M., Downs, R. T., Bish, D., et al. (2013).
1381 Curiosity at Gale Crater, Mars: Characterization and Analysis of the Rocknest Sand
1382 Shadow. *Science*, *341*(6153), 1239505–1239505. https://doi.org/10.1126/science.1239505

1383 Blaney, D. L., Wiens, R. C., Maurice, S., Clegg, S. M., Anderson, R. B., Kah, L. C., et al.
1384 (2014). Chemistry and texture of the rocks at Rocknest, Gale Crater: Evidence for

1385 sedimentary origin and diagenetic alteration. *Journal of Geophysical Research: Planets*,
1386 *119*(9), 2109–2131. https://doi.org/10.1002/2013JE004590

1387 Bridges, J. C., Schwenzer, S. P., Leveille, R., Westall, F., Wiens, R. C., Mangold, N., et al.
1388 (2015). Diagenesis and clay mineral formation at Gale Crater, Mars. *Journal of Geophysical*
1389 *Research: Planets*, *120*(1), 1–19. https://doi.org/10.1002/2014JE004757

1390 Bridges, N. T., & Ehlmann, B. L. (2018). The Mars Science Laboratory (MSL) Bagnold Dunes
1391 Campaign, Phase I: Overview and introduction to the special issue. *Journal of Geophysical*
1392 *Research: Planets*, *123*(1), 3–19. https://doi.org/10.1002/2017JE005401

1393 Bridges, N. T., Geissler, P. E., McEwen, A. S., Thomson, B. J., Chuang, F. C., Herkenhoff, K.
1394 E., et al. (2007). Windy Mars: A dynamic planet as seen by the HiRISE camera.
1395 *Geophysical Research Letters*, *34*(23).
1396 https://doi.org/https://doi.org/10.1029/2007GL031445

1397 Bridges, N. T., Sullivan, R., Newman, C. E., Navarro, S., van Beek, J., Ewing, R. C., et al.
1398 (2017). Martian aeolian activity at the Bagnold Dunes, Gale Crater: The view from the
1399 surface and orbit. *Journal of Geophysical Research: Planets*, *122*(10), 2077–2110.
1400 https://doi.org/10.1002/2017JE005263

1401 Bristow, T. F., Rampe, E. B., Achilles, C. N., Blake, D. F., Chipera, S. J., Craig, P., et al. (2018).
1402 Clay mineral diversity and abundance in sedimentary rocks of Gale crater, Mars. *Science*
1403 *Advances*, *4*(6), eaar3330. https://doi.org/10.1126/sciadv.aar3330

1404 Bryk, A. A., Dientrich, W. E., Lamb, M. P., Grotzinger, J. P., Vasavada, A. R., Stack, K. M.,
1405 Arvidson, A. (2019). What was the original extent of the Greenheugh pediment and Gediz
1406 Vallis ridge deposits in Gale crater, Mars. In *Ninth International Conference on Mars.*
1407 vol:2089, p.6296.

1408 Carr, M. H., & Head, J. W. (2010). Geologic history of Mars. *Earth and Planetary Science*
1409 *Letters*, *294*(3–4), 185–203. https://doi.org/10.1016/J.EPSL.2009.06.042

1410 Chan, M., Potter, S., Peterson, E., Parry, W., Bowman, J., Grotzinger, J., & Milliken, R. (2012).
1411 Characteristics of terrestrial ferric oxide concretions and implications for Mars. *Sedimentary*
1412 *Geology of Mars*, *102*, 253–270. Retrieved from
1413 https://pdfs.semanticscholar.org/b238/8ccb9b302d832316a3f17cb561868cd9391c.pdf

1414 Clegg, S. M., Wiens, R. C., Anderson, R., Forni, O., Frydenvang, J., Lasue, J., et al. (2017).
1415 Recalibration of the Mars Science Laboratory ChemCam instrument with an expanded
1416 geochemical database. *Spectrochimica Acta Part B: Atomic Spectroscopy*, *129*, 64–85.
1417 https://doi.org/10.1016/J.SAB.2016.12.003

1418 Cornwall, C., Bandfield, J. L., Titus, T. N., Schreiber, B. C., & Montgomery, D. R. (2015).
1419 Physical abrasion of mafic minerals and basalt grains: Application to martian aeolian
1420 deposits. *Icarus*, *256*, 13–21. https://doi.org/10.1016/j.icarus.2015.04.020

1421 Cousin, A., Meslin, P. Y., Wiens, R. C., Rapin, W., Mangold, N., Fabre, C., et al. (2015).
1422 Compositions of coarse and fine particles in martian soils at gale: A window into the
1423 production of soils. *Icarus*, *249*, 22–42. https://doi.org/10.1016/J.ICARUS.2014.04.052

1424 Cousin, A., Dehouck, E., Meslin, P. -Y., Forni, O., Williams, A. J., Stein, N., et al. (2017).
1425 Geochemistry of the Bagnold dune field as observed by ChemCam and comparison with

other aeolian deposits at Gale Crater. *Journal of Geophysical Research: Planets*, *122*(10), 2144–2162. https://doi.org/10.1002/2017JE005261

Czarnecki, S., Hardgrove, C., Gasda, P. J., Gabriel, T. S. J., Starr, M., Rice, M. S., et al. (2020). Identification and Description of a Silicic Volcaniclastic Layer in Gale Crater, Mars, Using Active Neutron Interrogation. *Journal of Geophysical Research: Planets*, *125*(3), 2019–006180. https://doi.org/10.1029/2019JE006180

Day, M., Anderson, W., Kocurek, G., & Mohrig, D. (2016). Carving intracrater layered deposits with wind on Mars. *Geophysical Research Letters*, *43*(6), 2473–2479. https://doi.org/10.1002/2016GL068011@10.1002/(ISSN)1944-8007.2016GRLEDHIGH

Day, Mackenzie, & Kocurek, G. (2016). Observations of an aeolian landscape: From surface to orbit in Gale Crater. *Icarus*, *280*, 37–71. https://doi.org/10.1016/j.icarus.2015.09.042

Dehouck, E., Cousin, A., Mangold, N., Frydenvang, J., Gasnault, O., Forni, O., Rapin, W., Gasda, P. J., Bedford, C. C., Caravaca, G., David, G., Lasue, J., Meslin, P.-Y., Rammelkamp, K., Le Mouelic, S., Fox, V. K., Bennett, K. A., Bryk, A. A., Lanza, N. L., Maurice, S., Wiens, R. (this issue). In situ geochemical characterization of the clay-bearing Glen Torridon region of Gale crater, Mars, using the ChemCam instrument. *JGR: Planets.*

Edgar, L. A., Fedo, C. M., Gupta, S., Banham, S., Fraeman, A. A., Grotzinger, J., et al. (2020). A lacustrine paleoenvironment recorded at Vera Rubin ridge, Gale crater: Overview of the sedimentology and stratigraphy observed by the Mars Science Laboratory Curiosity rover. *Earth and Space Science Open Archive*. https://doi.org/10.1002/essoar.10501350.1

Edgett, K. S., Yingst, R. A., Ravine, M. A., Caplinger, M. A., Maki, J. N., Ghaemi, F. T., et al. (2012). Curiosity's Mars Hand Lens Imager (MAHLI) Investigation. *Space Science Reviews*, *170*(1–4), 259–317. https://doi.org/10.1007/s11214-012-9910-4

Edgett, K. S., Banham, S. G., Bennett, K. A., Edgar, L. A., Edwards, C. S., Fairén, A. G., et al. (2020). Extraformational sediment recycling on Mars. *Geosphere*, *16*(6), 1508–1537. https://doi.org/10.1130/GES02244.1

Eggleton, R. A., Foudoulis, C., & Varkevisser, D. (1987). Weathering of Basalt: Changes in Rock Chemistry and Mineralogy. *Clays and Clay Minerals*, *35*(3), 161–169. https://doi.org/10.1346/CCMN.1987.0350301

Ehlmann, B. L., Edgett, K. S., Sutter, B., Achilles, C. N., Litvak, M. L., Lapotre, M. G. A., et al. (2017). Chemistry, mineralogy, and grain properties at Namib and High dunes, Bagnold dune field, Gale crater, Mars: A synthesis of Curiosity rover observations. *Journal of Geophysical Research: Planets*, *122*(12), 2510–2543. https://doi.org/10.1002/2017JE005267

Eilers, P. H. C., & Goeman, J. J. (2004). Enhancing scatterplots with smoothed densities. *Bioinformatics (Oxford, England)*, *20*(5), 623–8. https://doi.org/10.1093/bioinformatics/btg454

Ewing, R. C., Lapotre, M. G. A., Lewis, K. W., Day, M., Stein, N., Rubin, D. M., et al. (2017). Sedimentary processes of the Bagnold Dunes: Implications for the eolian rock record of Mars. *Journal of Geophysical Research: Planets*, *122*(12), 2544–2573. https://doi.org/10.1002/2017JE005324

1467 Fedo, C. M., McGlynn, I. O., & McSween, H. Y. (2015). Grain size and hydrodynamic sorting
1468 controls on the composition of basaltic sediments: Implications for interpreting martian
1469 soils. *Earth and Planetary Science Letters*, *423*, 67–77.
1470 https://doi.org/10.1016/j.epsl.2015.03.052

1471 Fedo, C. M., Grotzinger, J. P., Gupta, S., Fraeman, A., Edgar, L., Edgett, K., et al. (2018).
1472 Sedimentology and Stratigraphy of the Murray Formation, Gale Crater, Mars. *49th Lunar*
1473 *and Planetary Science Conference 19-23 March, 2018, Held at The Woodlands, Texas LPI*
1474 *Contribution No. 2083, Id.2078*, *49*. Retrieved from
1475 http://adsabs.harvard.edu/abs/2018LPI....49.2078F

1476 Fenton, L. K., Gullikson, A. L., Hayward, R. K., Charles, H., & Titus, T. N. (2019). The Mars
1477 Global Digital Dune Database (MGD3): Global patterns of mineral composition and
1478 bedform stability. *Icarus*, *330*, 189–203. https://doi.org/10.1016/J.ICARUS.2019.04.025

1479 Forni, O., Maurice, S., Gasnault, O., Wiens, R. C., Cousin, A., Clegg, S. M., et al. (2013).
1480 Independent component analysis classification of laser induced breakdown spectroscopy
1481 spectra. *Spectrochimica Acta Part B: Atomic Spectroscopy*, *86*, 31–41.
1482 https://doi.org/10.1016/j.sab.2013.05.003

1483 Forni, O., Gaft, M., Toplis, M. J., Clegg, S. M., Maurice, S., Wiens, R. C., et al. (2015). First
1484 detection of fluorine on Mars: Implications for Gale Crater's geochemistry. *Geophysical*
1485 *Research Letters*, *42*(4), 1020–1028. https://doi.org/https://doi.org/10.1002/2014GL062742

1486 Forni, O., E. Dehouck, A. Cousin, C. C. Bedford, G. David, S. P. Schwenzer, J. C. Bridges et al.
1487 "Elevated Fluorine Abundances Below the Siccar Point Unconformity: Implications for
1488 Fluid Circulation in Gale Crater." In *Lunar and Planetary Science Conference*, no. 2548, p.
1489 1503. 2021.

1490 Fraeman, A. A., Ehlmann, B. L., Arvidson, R. E., Edwards, C. S., Grotzinger, J. P., Milliken, R.
1491 E., et al. (2016). The stratigraphy and evolution of lower Mount Sharp from spectral,
1492 morphological, and thermophysical orbital data sets. *Journal of Geophysical Research:*
1493 *Planets*, *121*(9), 1713–1736. https://doi.org/10.1002/2016JE005095

1494 Fraeman, A. A., Edgar, L. A., Rampe, E. B., Thompson, L. M., Frydenvang, J., Fedo, C. M., et
1495 al. (2020). Evidence for a Diagenetic Origin of Vera Rubin Ridge, Gale Crater, Mars:
1496 Summary and Synthesis of Curiosity's Exploration Campaign. *Journal of Geophysical*
1497 *Research: Planets*, *125*(12), 2020–006527. https://doi.org/10.1029/2020JE006527

1498 Frydenvang, J., Gasda, P. J., Hurowitz, J. A., Grotzinger, J. P., Wiens, R. C., Newsom, H. E., et
1499 al. (2017). Diagenetic silica enrichment and late-stage groundwater activity in Gale crater,
1500 Mars. *Geophysical Research Letters*, *44*(10), 4716–4724.
1501 https://doi.org/10.1002/2017GL073323

1502 Gasda, P. J., Anderson, R. B., Cousin, A., Forni, O., Clegg, S. M., Ollila, A., et al. (2021).
1503 Quantification of manganese for ChemCam Mars and laboratory spectra using a
1504 multivariate model. *Spectrochimica Acta Part B: Atomic Spectroscopy*, *181*, 106223.
1505 https://doi.org/10.1016/j.sab.2021.106223

1506 Gasda, P. J., Comellas, J., Essunfeld, A., Das, D., Bryk, A. B., Dehouck, E., Schwenzer, S. P.,
1507 Crossey, L., Herkenhoff, K., Johnson, J. R., Newsom, H., Lanza, N. L., Rapin, W., Goetz,
1508 W., Meslin, P.-Y., Bridges, J. C., Anderson, R., David, G., Turner, S. M. R., Thorpe, M. T.,

Kah, L., Frydenvang, J., Kronyak, R., Caravaca, G., Ollila, A., Le Mouelic, S., Nellessen, M., Hoffman, M., Fey, D., Cousin, A., Wiens, R. C., Clegg, S. M., Maurice, S., Gasnault, O., Delapp, D., Reyes-Newell, A. (this issue), Overview of the Morphology and Chemistry of Diagenetic features in the clay-rich Glen Torridon unit of Gale crater, Mars. *JGR: Planets.*

Gellert, R., & Clark, B. C. (2015). In Situ Compositional Measurements of Rocks and Soils with the Alpha Particle X-ray Spectrometer on NASA's Mars Rovers. *Elements*, *11*(1), 39–44. https://doi.org/10.2113/gselements.11.1.39

Greeley, R., Lancaster, N., Lee, S., & Thomas, P. (1992). Martian aeolian processes, sediments, and features. *Mars*, 730–766.

Grotzinger, J. P., Crisp, J., Vasavada, A. R., Anderson, R. C., Baker, C. J., Barry, R., et al. (2012). Mars Science Laboratory Mission and Science Investigation. *Space Science Reviews*, *170*(1), 5–56. https://doi.org/10.1007/s11214-012-9892-2

Grotzinger, J. P., Sumner, D. Y., Kah, L. C., Stack, K., Gupta, S., Edgar, L., et al. (2014). A habitable fluvio-lacustrine environment at Yellowknife Bay, Gale crater, Mars. *Science*, *343*(6169), 1242777. https://doi.org/10.1126/science.1242777

Grotzinger, J. P., Gupta, S., Malin, M. C., Rubin, D. M., Schieber, J., Siebach, K., et al. (2015). Deposition, exhumation, and paleoclimate of an ancient lake deposit, Gale crater, Mars. *Science*, *350*(6257), aac7575–aac7575. https://doi.org/10.1126/science.aac7575

Hausrath, E. M., Ming, D. W., Peretyazhko, T. S., & Rampe, E. B. (2018). Reactive transport and mass balance modeling of the Stimson sedimentary formation and altered fracture zones constrain diagenetic conditions at Gale crater, Mars. *Earth and Planetary Science Letters*, *491*, 1–10. https://doi.org/10.1016/J.EPSL.2018.02.037

Hobbs, S. W., Paull, D. J., & Bourke, M. C. (2010). Aeolian processes and dune morphology in Gale Crater. *Icarus*, *210*(1), 102–115. https://doi.org/10.1016/J.ICARUS.2010.06.006

Horgan, B. H. N., Johnson, J. R., Fraeman, A. A., Rice, M. S., Seeger, C., Bell III, J. F., et al. (2020). Diagenesis of Vera Rubin Ridge, Gale Crater, Mars, From Mastcam Multispectral Images. *Journal of Geophysical Research: Planets*, *125*(11), e2019JE006322. https://doi.org/https://doi.org/10.1029/2019JE006322

James Sara, M. (2017). Dyngjusandur sand sheet, Iceland, as a depositional analog to the Stimson Fm. in Gale Crater, Mars. *Theses and Dissertations*. https://doi.org/10.17077/etd.25rc5gg2

Jerolmack, D. J., Mohrig, D., Grotzinger, J. P., Fike, D. A., & Watters, W. A. (2006). Spatial grain size sorting in eolian ripples and estimation of wind conditions on planetary surfaces: Application to Meridiani Planum, Mars. *Journal of Geophysical Research E: Planets*, *111*(12), 12–14. https://doi.org/10.1029/2005JE002544

Jia, C., Wu, L., Chen, Q., Ke, P., Yoreo, J. J. De, & Guan, B. (2020). Structural evolution of amorphous calcium sulfate nanoparticles into crystalline gypsum phase. *CrystEngComm*, *22*(41), 6805–6810. https://doi.org/10.1039/D0CE01173H

Jiang, Q., & Yang, X. (2019). Sedimentological and Geochemical Composition of Aeolian Sediments in the Taklamakan Desert: Implications for Provenance and Sediment Supply

Mechanisms. *Journal of Geophysical Research: Earth Surface*, *124*(5), 1217–1237. https://doi.org/10.1029/2018JF004990

Kocurek, G., & Havholm, K. G. (1993) Eolian Sequence Stratigraphy -- A Conceptual Framework: Chapter 16: Recent Developments in Siliciclastic Sequence Stratigraphy. *AAPG Special Volumes*, *169,* 393–409.

Kocurek, G., & Ewing, R. C. (2012). Source-to-sink: An earth/mars comparison of boundary conditions for Eolian dune systems. *SEPM Special Publications*, *102*, 151–168. https://doi.org/10.2110/pec.12.102.0151

Kronyak, R. E., Kah, L. C., Miklusicak, N. B., Edgett, K. S., Sun, V. Z., Bryk, A. B., & Williams, R. M. E. (2019b). Extensive Polygonal Fracture Network in Siccar Point group Strata: Fracture Mechanisms and Implications for Fluid Circulation in Gale Crater, Mars. *Journal of Geophysical Research: Planets*, *0*(0). https://doi.org/10.1029/2019JE006125

Kronyak, R. E., Kah, L. C., Edgett, K. S., VanBommel, S. J., Thompson, L. M., Wiens, R. C., et al. (2019a). Mineral-Filled Fractures as Indicators of Multigenerational Fluid Flow in the Pahrump Hills Member of the Murray Formation, Gale Crater, Mars. *Earth and Space Science*, *6*(2), 238–265. https://doi.org/10.1029/2018EA000482

Lapotre, M. G. A., & Rampe, E. B. (2018). Curiosity's Investigation of the Bagnold Dunes, Gale Crater: Overview of the Two-Phase Scientific Campaign and Introduction to the Special Collection. *Geophysical Research Letters*, *45*(19), 10,200-10,210. https://doi.org/10.1029/2018GL079032

Lasue, J., Cousin, A., Meslin, P. -Y., Mangold, N., Wiens, R. C., Berger, G., et al. (2018). Martian Eolian Dust Probed by ChemCam. *Geophysical Research Letters*, *45*(20), 10,968-10,977. https://doi.org/10.1029/2018GL079210

Malin, M. C., Edgett, K. S., Dietrich, W. E., Gupta, S., Sumner, D. Y., Wiens, R. C., et al. (2000). Sedimentary Rocks of Early Mars. *Science*, *290*(5498), 1927–1937. https://doi.org/10.1126/science.290.5498.1927

Malin, M. C., Ravine, M. A., Caplinger, M. A., Ghaemi, F. T., Schaffner, J. A., Maki, J. N., et al. (2017). The Mars Science Laboratory (MSL) Mast cameras and Descent imager: Investigation and instrument descriptions. *Earth and Space Science*, *4*(8), 506–539. https://doi.org/10.1002/2016EA000252

Mangold, N., Baratoux, D., Arnalds, O., Bardintzeff, J.-M., Platevoet, B., Grégoire, M., & Pinet, P. (2011). Segregation of olivine grains in volcanic sands in Iceland and implications for Mars. *Earth and Planetary Science Letters*, *310*(3–4), 233–243. https://doi.org/10.1016/J.EPSL.2011.07.025

Mangold, N., Thompson, L. M., Forni, O., Williams, A. J., Fabre, C., Le Deit, L., et al. (2016). Composition of conglomerates analyzed by the Curiosity rover: Implications for Gale Crater crust and sediment sources. *Journal of Geophysical Research: Planets*, *121*(3), 353–387. https://doi.org/10.1002/2015JE004977

Mangold, N., Schmidt, M. E., Fisk, M. R., Forni, O., McLennan, S. M., Ming, D. W., et al. (2017). Classification scheme for sedimentary and igneous rocks in Gale crater, Mars. *Icarus*, *284*, 1–17. https://doi.org/10.1016/J.ICARUS.2016.11.005

1591 Maurice, S., Wiens, R. C., Saccoccio, M., Barraclough, B., Gasnault, O., Forni, O., et al. (2012).
1592 The ChemCam instrument suite on the Mars Science Laboratory (MSL) rover: Science
1593 objectives and mast unit description. *Space Science Reviews*, *170*(1–4), 95–166.
1594 https://doi.org/10.1007/s11214-012-9912-2

1595 Maurice, S., Clegg, S. M., Wiens, R. C., Gasnault, O., Rapin, W., Forni, O., et al. (2016).
1596 ChemCam activities and discoveries during the nominal mission of the Mars Science
1597 Laboratory in Gale crater, Mars. *Journal of Analytical Atomic Spectrometry*, *31*(4), 863–
1598 889. https://doi.org/10.1039/C5JA00417A

1599 McCollom, T. M., Hynek, B. M., Rogers, K., Moskowitz, B., & Berquó, T. S. (2013). Chemical
1600 and mineralogical trends during acid-sulfate alteration of pyroclastic basalt at Cerro Negro
1601 volcano and implications for early Mars. *Journal of Geophysical Research: Planets*, *118*(9),
1602 1719–1751. https://doi.org/10.1002/jgre.20114

1603 McCollom, T. M., Robbins, M., Moskowitz, B., Berquõ, T. S., Jöns, N., & Hynek, B. M. (2013).
1604 Experimental study of acid-sulfate alteration of basalt and implications for sulfate deposits
1605 on Mars. *Journal of Geophysical Research E: Planets*, *118*(4), 577–614.
1606 https://doi.org/10.1002/jgre.20044

1607 Meslin, P.-Y., Gasnault, O., Forni, O., Schröder, S., Cousin, A., Berger, G., et al. (2013). Soil
1608 diversity and hydration as observed by ChemCam at Gale crater, Mars. *Science (New York,*
1609 *N.Y.)*, *341*(6153), 1238670. https://doi.org/10.1126/science.1238670

1610 Milliken, R. E., Grotzinger, J. P., & Thomson, B. J. (2010a). Paleoclimate of Mars as captured
1611 by the stratigraphic record in Gale Crater. *Geophysical Research Letters*, *37*(4).
1612 https://doi.org/10.1029/2009GL041870

1613 Milliken, R. E., Grotzinger, J. P., & Thomson, B. J. (2010b). Paleoclimate of Mars as captured
1614 by the stratigraphic record in Gale Crater. *Geophysical Research Letters*, *37*(4).
1615 https://doi.org/10.1029/2009GL041870

1616 Morris, R. V., Vaniman, D. T., Blake, D. F., Gellert, R., Chipera, S. J., Rampe, E. B., et al.
1617 (2016). Silicic volcanism on Mars evidenced by tridymite in high-SiO_2 sedimentary rock at
1618 Gale crater. *Proceedings of the National Academy of Sciences*, *113*(26), 7071–7076.
1619 https://doi.org/10.1073/pnas.1607098113

1620 Morrison, S. M., Downs, R. T., Blake, D. F., Vaniman, D. T., Ming, D. W., Hazen, R. M., et al.
1621 (2018b). Crystal chemistry of martian minerals from Bradbury Landing through Naukluft
1622 Plateau, Gale crater, Mars. *American Mineralogist*, *103*(6), 857–871.
1623 https://doi.org/10.2138/am-2018-6124

1624 Morrison, S. M., Downs, R. T., Blake, D. F., Prabhu, A., Eleish, A., Vaniman, D. T., et al.
1625 (2018a). Relationships between unit-cell parameters and composition for rock-forming
1626 minerals on Earth, Mars, and other extraterrestrial bodies. *American Mineralogist*, *103*(6),
1627 848–856. https://doi.org/10.2138/am-2018-6123

1628 Morrone, C., De Rosa, R., Le Pera, E., & Marsaglia, K. M. (2017). Provenance of volcaniclastic
1629 beach sand in a magmatic-arc setting: An example from Lipari island (Aeolian archipelago,
1630 Tyrrhenian Sea). *Geological Magazine*, *154*(4), 804–828.
1631 https://doi.org/10.1017/S001675681600042X

1632 Le Mouélic, S., Gasnault, O., Herkenhoff, K. E., Bridges, N. T., Langevin, Y., Mangold, N., et

al. (2015). The ChemCam Remote Micro-Imager at Gale crater: Review of the first year of operations on Mars. *Icarus*, *249*, 93–107. https://doi.org/10.1016/J.ICARUS.2014.05.030

Mountney, N. P., & Russell, A. J. (2004). Sedimentology of cold-climate aeolian sandsheet deposits in the Askja region of northeast Iceland. *Sedimentary Geology*, *166*(3–4), 223–244. https://doi.org/10.1016/J.SEDGEO.2003.12.007

Muhs, D. R. (2004). Mineralogical maturity in dunefields of North America, Africa and Australia. *Geomorphology*, *59*(1–4), 247–269. https://doi.org/10.1016/j.geomorph.2003.07.020

Nesbitt, H. W., & Wilson, R. E. (1992). Recent chemical weathering of basalts. *American Journal of Science*, *292*(10), 740–777.

Newsom, H. E., Edgett, K. S., Fey, D. M., Wiens, R. C., Frydenvang, J., Banham, S. G., et al. (2018). A Buried Aeolian Lag Deposit at an Unconformity Between the Murray and Stimson Formations at Marias Pass, Gale Crater, Mars. *49th Lunar and Planetary Science Conference 19-23 March, 2018, Held at The Woodlands, Texas LPI Contribution No. 2083, Id.2263*, *49*. Retrieved from http://adsabs.harvard.edu/abs/2018LPI....49.2263N

O'Connell-Cooper, C. D., Spray, J. G., Thompson, L. M., Gellert, R., Berger, J. A., Boyd, N. I., et al. (2017). APXS-derived chemistry of the Bagnold dune sands: Comparisons with Gale Crater soils and the global Martian average. *Journal of Geophysical Research: Planets*, *122*(12), 2623–2643. https://doi.org/10.1002/2017JE005268

Pettijohn, F. J. (1954). Classification of Sandstones. *The Journal of Geology*, *62*(4), 360–365. https://doi.org/10.1086/626172

Pokrovsky, O. S., & Schott, J. (2000). Kinetics and mechanism of forsterite dissolution at 25°C and pH from 1 to 12. *Geochimica et Cosmochimica Acta*, *64*(19), 3313–3325. https://doi.org/10.1016/S0016-7037(00)00434-8

Potter-McIntyre, S. L., Chan, M. A., & McPherson, B. J. (2014). Concretion Formation In Volcaniclastic Host Rocks: Evaluating the Role of Organics, Mineralogy, and Geochemistry On Early Diagenesis. *Journal of Sedimentary Research*, *84*(10), 875–892. https://doi.org/10.2110/jsr.2014.58

Potter, S. L., Chan, M. A., Petersen, E. U., Dyar, M. D., & Sklute, E. (2011). Characterization of Navajo Sandstone concretions: Mars comparison and criteria for distinguishing diagenetic origins. *Earth and Planetary Science Letters*, *301*(3–4), 444–456. https://doi.org/10.1016/J.EPSL.2010.11.027

Rampe, E. B., Ming, D. W., Blake, D. F., Bristow, T. F., Chipera, S. J., Grotzinger, J. P., et al. (2017). *Mineralogy of an ancient lacustrine mudstone succession from the Murray formation, Gale crater, Mars*. *Earth and Planetary Science Letters* (Vol. 471). https://doi.org/10.1016/j.epsl.2017.04.021

Rampe, E. B., Lapotre, M. G. A., Bristow, T. F., Arvidson, R. E., Morris, R. V., Achilles, C. N., et al. (2018). Sand Mineralogy Within the Bagnold Dunes, Gale Crater, as Observed In Situ and From Orbit. *Geophysical Research Letters*, *45*(18), 9488–9497. https://doi.org/10.1029/2018GL079073

Rampe, E. B., Bristow, T. F., Morris, R. V., Morrison, S. M., Achilles, C. N., Ming, D. W., et al.

(2020a). Mineralogy of Vera Rubin Ridge From the Mars Science Laboratory CheMin Instrument. *Journal of Geophysical Research: Planets*, *125*(9), e2019JE006306. https://doi.org/10.1029/2019JE006306

Rampe, E.B., Yen, A., Bristow, T., Blake, D.F., Vaniman, D., Achilles, C., Chipera, S., Downs, R.T., Ming, D.W., Morris, R.V. and Morrison, S.M., 2020b, December. Mineralogy of the Greenheugh Pediment and Underlying Murray Formation from the Mars Science Laboratory CheMin Instrument. In *AGU Fall Meeting Abstracts* (Vol. 2020, pp. P070-09).

Rapin, W., Meslin, P.-Y., Maurice, S., Vaniman, D., Nachon, M., Mangold, N., et al. (2016). Hydration state of calcium sulfates in Gale crater, Mars: Identification of bassanite veins. *Earth and Planetary Science Letters*, *452*, 197–205. https://doi.org/10.1016/J.EPSL.2016.07.045

Rapin, W., Meslin, P. Y., Maurice, S., Wiens, R. C., Laporte, D., Chauviré, B., et al. (2017b). Quantification of water content by laser induced breakdown spectroscopy on Mars. *Spectrochimica Acta Part B: Atomic Spectroscopy*, *130*, 82–100. https://doi.org/10.1016/J.SAB.2017.02.007

Rapin, W., Bousquet, B., Lasue, J., Meslin, P. Y., Lacour, J. L., Fabre, C., et al. (2017a). Roughness effects on the hydrogen signal in laser-induced breakdown spectroscopy. *Spectrochimica Acta Part B: Atomic Spectroscopy*, *137*, 13–22. https://doi.org/10.1016/J.SAB.2017.09.003

Rudolph, B., K. Bennett, and M. Rice. "Sources of sand in Mt Sharp: Possible volcanic layers in Gale crater, Mars." *Planets* 122 (2019): 2489-2509.

Schröder, S., Meslin, P. Y., Gasnault, O., Maurice, S., Cousin, A., Wiens, R. C., et al. (2015). Hydrogen detection with ChemCam at Gale crater. *Icarus*, *249*, 43–61. https://doi.org/10.1016/J.ICARUS.2014.08.029

Siebach, K. L., McLennan, S. M., & Fedo, C. M. (2017). Geochemistry of the Stimson Sandstone, Gale Crater, Mars. *48th Lunar and Planetary Science Conference, Held 20-24 March 2017, at The Woodlands, Texas. LPI Contribution No. 1964, Id.2499*, *48*. Retrieved from http://adsabs.harvard.edu/abs/2017LPI....48.2499S

Smith, R. J., Rampe, E. B., Horgan, B. H. N., & Dehouck, E. (2018). Deriving Amorphous Component Abundance and Composition of Rocks and Sediments on Earth and Mars. *Journal of Geophysical Research: Planets*, *123*(10), 2485–2505. https://doi.org/10.1029/2018JE005612

Stack, K. M., Grotzinger, J. P., Lamb, M. P., Gupta, S., Rubin, D. M., Kah, L. C., et al. (2019). Evidence for plunging river plume deposits in the Pahrump Hills member of the Murray formation, Gale crater, Mars. *Sedimentology*, *66*(5), 1768–1802. https://doi.org/10.1111/sed.12558

Steele, L. J., Kite, E. S., & Michaels, T. I. (2018). Crater Mound Formation by Wind Erosion on Mars. *Journal of Geophysical Research: Planets*, *123*(1), 113–130. https://doi.org/https://doi.org/10.1002/2017JE005459

Sutter, B., McAdam, A. C., Mahaffy, P. R., Ming, D. W., Edgett, K. S., Rampe, E. B., et al.

(2017). Evolved gas analyses of sedimentary rocks and eolian sediment in Gale Crater, Mars: Results of the Curiosity rover's sample analysis at Mars instrument from Yellowknife Bay to the Namib Dune. *Journal of Geophysical Research: Planets*, *122*(12), 2574–2609. https://doi.org/10.1002/2016JE005225

Sutter, B., McAdam, A. C., Ming, D. W., Archer, P. D., Thompson, L. M., Stern, J. C., Eigenbrode, J. L., Mahaffy, P. R. (2022) "Constraining alteration processes along the Siccar Point Unconformity, Gale crater: Results from the Sample Analysis at Mars instrument", 53rd Lunar and Planetary Science Conference, Woodlands, TX, USA.

Thomas, M., Clarke, J. D. A., & Pain, C. F. (2005). Weathering, erosion and landscape processes on Mars identified from recent rover imagery, and possible Earth analogues. *Australian Journal of Earth Sciences*, *52*(3), 365–378. https://doi.org/10.1080/08120090500134597

Thomas, N. H., Ehlmann, B. L., Anderson, D. E., Clegg, S. M., Forni, O., Schröder, S., et al. (2018). Characterization of Hydrogen in Basaltic Materials With Laser-Induced Breakdown Spectroscopy (LIBS) for Application to MSL ChemCam Data. *Journal of Geophysical Research: Planets*, *123*(8), 1996–2021. https://doi.org/https://doi.org/10.1029/2017JE005467

Thomas, N. H., Ehlmann, B. L., Rapin, W., Rivera-Hernández, F., Stein, N. T., Frydenvang, J., et al. (2020). Hydrogen Variability in the Murray Formation, Gale Crater, Mars. *Journal of Geophysical Research: Planets*, *125*(9), e2019JE006289. https://doi.org/10.1029/2019JE006289

Thomson, B. J., Bridges, N. T., Milliken, R., Baldridge, A., Hook, S. J., Crowley, J. K., et al. (2011). Constraints on the origin and evolution of the layered mound in Gale Crater, Mars using Mars Reconnaissance Orbiter data. *Icarus*, *214*(2), 413–432. https://doi.org/10.1016/J.ICARUS.2011.05.002

Thompson, L. M., O'Connell-Cooper, C., Berger, J. A., Yen, A., APXS Team. (this issue). Widespread alteration at the base of the Siccar Point unconformity and evidence for a regional potassic source rock at Gale crater: Exploration of the Murray formation-Greenheugh pediment cap rock contact with the Alpha Particle X-ray spectrometer. *JGR: Planets*.

Thorpe, M. T., Bristow, T. F., Rampe, E. B., Tosca, N. J., Grotzinger J. P., Fedo, C. M., Chipera, S. J., Downs, G., Achilles, C. N., Blake, D. F., Castle, N., Craig, P., Des Marais, D. J., Downs, R. T., Hazen, R. M., Ming, D. W., Morris, R. V., Morrison, S. M., Treiman, A. H., Tu, V., Vaniman, D. T., Yen, A. S., Bryk, A. B., Bennett, K. A., Fox, V. K., Siebach, K. L., Fraeman, A. A., Vasavada, A. R. (this issue). The Mineralogy an dSedimentary History of the Glen Torridon Region, as detailed by the Mars Science Laboratory CheMin Instrument. *JGR: Planets.*

Tosca, N. J., McLennan, S. M., Lindsley, D. H., & Schoonen, M. A. A. (2004). Acid-sulfate weathering of synthetic Martian basalt: The acid fog model revisited. *Journal of Geophysical Research E: Planets*, *109*(5), 5003. https://doi.org/10.1029/2003JE002218

Treiman, A. H., Bish, D. L., Vaniman, D. T., Chipera, S. J., Blake, D. F., Ming, D. W., et al. (2016a). Mineralogy, provenance, and diagenesis of a potassic basaltic sandstone on Mars: CheMin X-ray diffraction of the Windjana sample (Kimberley area, Gale Crater). *Journal of Geophysical Research. Planets*, *121*(1), 75–106. https://doi.org/10.1002/2015JE004932

Treiman, A. H., Bish, D. L., Vaniman, D. T., Chipera, S. J., Blake, D. F., Ming, D. W., et al. (2016b). Mineralogy, provenance, and diagenesis of a potassic basaltic sandstone on Mars: CheMin X-ray diffraction of the Windjana sample (Kimberley area, Gale Crater). *Journal of Geophysical Research: Planets*, *121*(1), 75–106. https://doi.org/10.1002/2015JE004932

Vaniman, D. T., Bish, D. L., Ming, D. W., Bristow, T. F., Morris, R. V., Blake, D. F., et al. (2014). Mineralogy of a Mudstone at Yellowknife Bay, Gale Crater, Mars. *Science*, *343*(6169), 1243480–1243480. https://doi.org/10.1126/science.1243480

Vasavada, A. R., Grotzinger, J. P., Arvidson, R. E., Calef, F. J., Crisp, J. A., Gupta, S., et al. (2014). Overview of the Mars Science Laboratory mission: Bradbury Landing to Yellowknife Bay and beyond. *Journal of Geophysical Research: Planets*, *119*(6), 1134–1161. https://doi.org/10.1002/2014JE004622

Watkins, J. A., Grotzinger, J., Stein, N., Banham, S. G., Gupta, S., Rubin, D., et al. (2016). Paleotopography of Erosional Unconformity, Base of Stimson Formation, Gale Crater, Mars. *47th Lunar and Planetary Science Conference, Held March 21-25, 2016 at The Woodlands, Texas. LPI Contribution No. 1903, p.2939*, *47*, 2939. Retrieved from http://adsabs.harvard.edu/abs/2016LPI....47.2939W

Wiens, R. C., Maurice, S., Barraclough, B., Saccoccio, M., Barkley, W. C., Bell III, J. F., et al. (2012). The ChemCam Instrument Suite on the Mars Science Laboratory (MSL) Rover: Body Unit and Combined System Tests. *Space Science Reviews*, *170*(1–4), 167–227. https://doi.org/10.1007/s11214-012-9902-4

Wiens, R. C., Maurice, S., Lasue, J., Forni, O., Anderson, R. B., Clegg, S., et al. (2013). Pre-flight calibration and initial data processing for the ChemCam laser-induced breakdown spectroscopy instrument on the Mars Science Laboratory rover. *Spectrochimica Acta Part B: Atomic Spectroscopy*, *82*, 1–27. https://doi.org/10.1016/j.sab.2013.02.003

Wiens, R. C. (2013a) MSL MARS CHEMCAM LIBS SPECTRA 4/5 RDR V1.0 [Data set]. NASA Planetary Data System. https://doi.org/10.17189/1519485

Wiens, R. C. (2013b) MSL MARS CHEMCAM REMOTE MICRO-IMAGER CAMERA 5 RDR V1.0 [Data set]. NASA Planetary Data System. https://doi.org/10.17189/1519494

Wiens, R. C., Edgett, K. S., Stack, K. M., Dietrich, W. E., Bryk, A. B., Mangold, N., et al. (2020). Origin and composition of three heterolithic boulder- and cobble-bearing deposits overlying the Murray and Stimson formations, Gale Crater, Mars. *Icarus*, *350*, 113897. https://doi.org/10.1016/j.icarus.2020.113897

Willetts, B. B., Rice, M. A., & Swaine, S. E. (1982). Shape effects in aeolian grain transport. *Sedimentology*, *29*(3), 409–417. https://doi.org/10.1111/j.1365-3091.1982.tb01803.x

Yen, A. S., Ming, D. W., Vaniman, D. T., Gellert, R., Blake, D. F., Morris, R. V., et al. (2017). Multiple stages of aqueous alteration along fractures in mudstone and sandstone strata in Gale Crater, Mars. *Earth and Planetary Science Letters*, *471*, 186–198. https://doi.org/10.1016/J.EPSL.2017.04.033

Yen, A. S., Morris, R. V., Ming, D. W., Schwenzer, S. P., Sutter, B., Vaniman, D. T., et al. (2021). Formation of Tridymite and Evidence for a Hydrothermal History at Gale Crater, Mars. *Journal of Geophysical Research: Planets*, *126*(3), e2020JE006569. https://doi.org/10.1029/2020JE006569

1800 Zhu, B., & Yang, X. (2009). Chemical Weathering of Detrital Sediments in the Taklamakan
1801 Desert, Northwestern China. *Geographical Research*, *47*(1), 57–70.
1802 https://doi.org/10.1111/J.1745-5871.2008.00555.X

1803 Zimbelman, J. R., & Foroutan, M. (2020). Dingo Gap: Curiosity Went Up a Small Transverse
1804 Aeolian Ridge and Came Down a Megaripple. *Journal of Geophysical Research: Planets*,
1805 *125*(12), e2020JE006489. https://doi.org/10.1029/2020JE006489

1806

Figure Headings

Figure 1. Map of the Stimson formation localities investigated to date along the Curiosity rover's traverse. The labelled, colored units show the present-day extent of the Stimson formation (Siccar Point group) at the Emerson Plateau (blue), Naukluft Plateau (green), Murray Buttes (yellow), and Greenheugh pediment capping unit (orange). The solid white line shows the traverse, and the yellow waypoints mark key drill sites in the Mt Sharp group mudstones and Siccar Point group Stimson formation sandstones. The black streaks oriented from the NE to the SW derive the active Bagnold dune field.

Figure 2. Stratigraphic column of the geological units investigated by the MSL Curiosity rover in Gale crater, Mars. The Stimson formation sandstones are represented as tan-colored blocks. Dots are drill hole samples with those discussed in this paper labelled as BK (Buckskin), Big Sky (BS), Greenhorn (GH), Lubango (LB), Okoruso (OK), Oudam (OU), Hutton (HU), Edinburgh (EB). Mt Sharp group drill samples are labelled purple, Stimson formation drills are labelled red. Image credit is courtesy of the MSL sedimentology and stratigraphy group.

Figure 3. Mastcam mosaics of the Stimson formation at A) the top of the Greenheugh pediment (mcam14517, sol 2702), B) side view of the Greenheugh pediment (mcam14007, sol 2683), C) Williams outcrop at the Emerson plateau showing cross-bedding and a vertical light-toned halo (mcam004777, sol 1087), D) Naukluft plateau at the unconformity (dashed white line) of the Murray formation and the Stimson formation (mcam0597, sol 1275). MAHLI images of the bedrock drill targets for the Stimson formation at each locality are also provided in the insets: a) is of the Edinburgh target of the Edinburgh interval (sol 2703, after DRT), b) The Machir Bay target of the Ladder interval (sol 2699, after DRT), c) The target Big Sky (sol 1114, after DRT), and d) the target Okoruso (sol 1330, after DRT). Image credits for the Mastcam mosaics: NASA/JPL-Caltech/MSSS.

Figure 4. ChemCam RMI image mosaics, MAHLI images, and Navcam images showing the diversity of alteration features within the Stimson formation at each locality.

Figure 5. A. Distribution of ChemCam classifications between each Stimson locality where each count equals to one ChemCam observation point. Bedrock low totals is the number of bedrock observation points that had total sum of oxides <90 wt%. **B.** Distribution of ChemCam classifications between each Greenheugh stratigraphic interval (excluding the basal Stimson unit). Observation points that targeted float rocks and soils at these localities were not included. Sampling bias will have affected the number of ChemCam points on alteration features relative to those of bedrock, particularly for the silica-rich halos, as they were intentionally prioritized in the Emerson and Naukluft plateaus.

Figure 6. Histograms of ChemCam major element oxides for the bulk rock dataset at each Stimson locality. These data exclude those outside the 90-105 wt% range for total sum of oxides. Binning was selected based on the Minitab default setting which defines the histogram intervals according to the number of observations and the maximum and minimum values in the dataset. For our dataset, the number of intervals range between 21 and 34. The black vertical line shows the mean value of the major element oxide at each locality. The y-axis shows the number of data

points in each bin (frequency). The histogram for MnO was restricted to 1 wt% but has outliers to higher values which skews the mean, particularly for Greenheugh.

Figure 7. Boxplots of geochemical variation associated with the unconformity for the bedrock datasets of the underlying Carolyn Shoemaker formation and overlying Stimson formation. FeO_T and TiO_2 showed little variation and were not included in the plots. Dashed lines show the mean composition of the Stimson formation at Greenheugh (red) and the Carolyn Shoemaker formation (blue). Dotted lines show the uncertainty around the respective sample means through 2x the standard error.

Figure 8. A. H peak area data distribution for the Greenheugh pediment capping unit according to the different stratigraphic intervals. The concretion-rich Hutton interval has the lowest peak H abundance while the non-concretionary Edinburgh and Ladder Intervals have the higher H abundance. **B**. F variation with distance from the unconformity for the Stimson formation and the underlying Mt Sharp group. Alteration features (halos, concretions, raised ridges, veins) and alteration-free bedrock are shown. **C.** Annotated Mastcam image (mcam_14083) of the side of the Greenheugh pediment showing the division between the concretionary Glean Beag Interval and the Edinburgh Interval that has fewer concretions concentrated towards the base. Image credit for the Mastcam mosaic used in C: NASA/JPL-Caltech/MSSS.

Figure 9. Dendrogram of the Cluster analysis results for Stimson across all localities.

Figure 10. Pie charts showing the distribution of the clusters across Stimson localities. The red and blue wedges correspond to the relative abundances of mafic minerals present at each locality.

Figure 11. Biplots showing the geochemistry of the Stimson formation at the Greenheugh pediment capping unit compared to that of the earlier Stimson formations, the geochemical compositions of the clusters, and the chemical compositions of the primary igneous minerals identified in the Big Sky drilled sample of the Stimson sandstone (Yen et al., 2017), and the Gobabeb scooped sample of the active aeolian Bagnold dunes (Achilles et al., 2017). Bulk Stimson compositions are shown as density contours in addition to a linear regression model (dashed black line). Cluster compositions also show 1 standard deviation. **A.** A $Al_2O_3+Na_2O+K_2O$ vs $MgO + FeO_T$ plot to show the variation in chemistry that relates to mafic and felsic minerals. **B**. A MnO vs MgO plot to show the unusual chemistry of Cluster 5

Figure 12. Annotated ChemCam RMI mosaics of targets **A**. Mowry (sol 1080) of the Emerson Plateau, **B**. Bentiaba (sol 1320) of the Naukluft plateau, **C**. Lowther Hills (sol 2697) of the Gleann Beag interval, and **D**. Dunedin (sol 2720) of the Edinburgh Interval. Colored circles show the cluster memberships of the associated ChemCam observation points.

Figure 13: A. and **B**. show geochemical plots of the ChemCam targets immediately above and below the unconformity. Each point is an observation point composition with green points related to the Carolyn Shoemaker formation (target names are Ariundle, Shannochie, Corriecravie, Hutton), and orange and gray points related to the Stimson formation (target names are Huttons section and Gleann Beag). Black arrow shows the geochemical trend relating to Ca-sulfates. The solid line represents a mixing line between the average composition of the Stimson formation at the Greenheugh pediment and the bulk Carolyn Shoemaker formation (Dehouck et

al*., this issue*). Percentages along the mixing line show the percentage of Stimson (e.g., 25% is 25% Stimson, 75% Murray). Dashed lines represent 1 standard deviation of this mixing line. **C.** and **D.** show the MAHLI images of Stimson targets near the unconformity at the Greenheugh pediment capping unit. Yellow arrows point to angular mudstone clasts in the Stimson formation. White arrows point to light-toned, spherical grains that may also relate to rounded mudstone clasts (Banham et al., *this issue*).

Figure 14. Mastcam image of light-toned alteration features in the underlying Murray formation pooling at the unconformity with the Stimson formation and breaching through the fractures. Image was taken at the Naukluft plateau (mcam05931, sol 1267). Image credit: NASA/JPL-Caltech/MSSS.

Table 1. Basic statistics (mean, standard error of the mean (SE Mean), standard deviation (StDev), minimum (Min), median (Med), and maximum (Max)) for the bulk rock data at each locality. Mean and median values are highlighted based on whether they represent the largest value (red) or the lowest value (blue), taking into consideration the standard error of the mean. Both standard deviation and error are provided as standard deviation is representative of the dispersion of the individual data values to the mean, while the standard error of the mean considers the number of points in the dataset and measures how far the sample mean of the data is from the true population.

Table 2. Mean composition, standard error of the mean (+/-), and standard deviation (std) of the derived clusters. Colors highlight the highest abundances (red), the lowest (blue), and the gradation in between for each of the five clusters.

Figure 1.

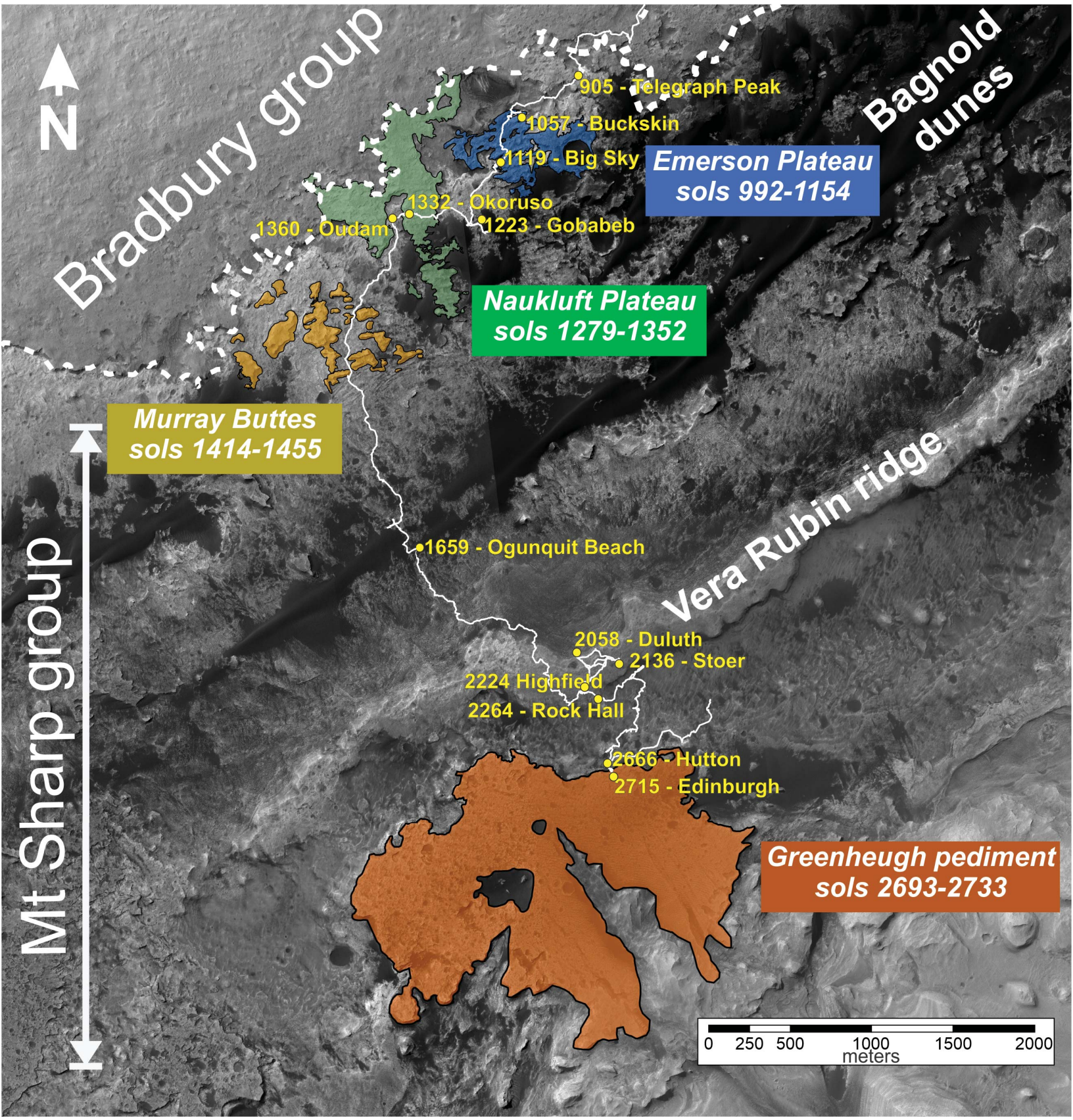
N
Bradbury group
905 - Telegraph Peak
1057 - Buckskin
1119 - Big Sky
Emerson Plateau
sols 992-1154
Bagnold
dunes
1332 - Okoruso
1360 - Oudam
1223 - Gobabeb
Naukluft Plateau
sols 1279-1352
Murray Buttes
sols 1414-1455
Mt Sharp group
Vera Rubin ridge
1659 - Ogunquit Beach
2058 - Duluth
2136 - Stoer
2224 Highfield
2264 - Rock Hall
2666 - Hutton
2715 - Edinburgh
Greenheugh pediment
sols 2693-2733
0 250 500 1000 1500 2000
meters

Figure 2.

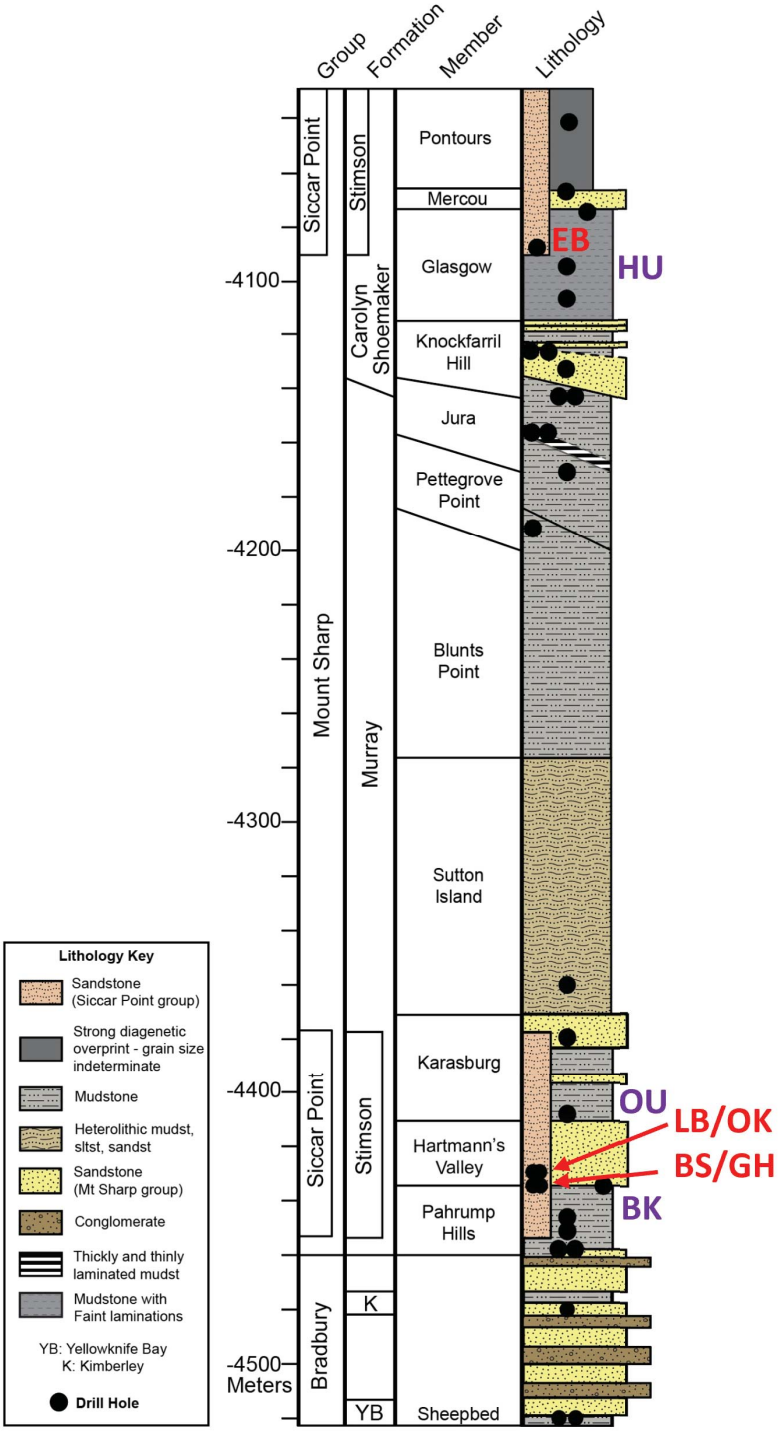
Group
Formation
Member
Lithology
Siccar Point
Stimson
Pontours
Mercou
Glasgow
Carolyn Shoemaker
Knockfarril Hill
Jura
Pettegrove Point
Blunts Point
Mount Sharp
Murray
Sutton Island
Karasburg
Hartmann's Valley
Pahrump Hills
Siccar Point
Stimson
Bradbury
K
YB
Sheepbed
-4100
-4200
-4300
-4400
-4500
Meters
EB
HU
OU
LB/OK
BS/GH
BK
Lithology Key
Sandstone (Siccar Point group)
Strong diagenetic overprint - grain size indeterminate
Mudstone
Heterolithic mudst, sltst, sandst
Sandstone (Mt Sharp group)
Conglomerate
Thickly and thinly laminated mudst
Mudstone with Faint laminations
YB: Yellowknife Bay
K: Kimberley
Drill Hole

Figure 3.

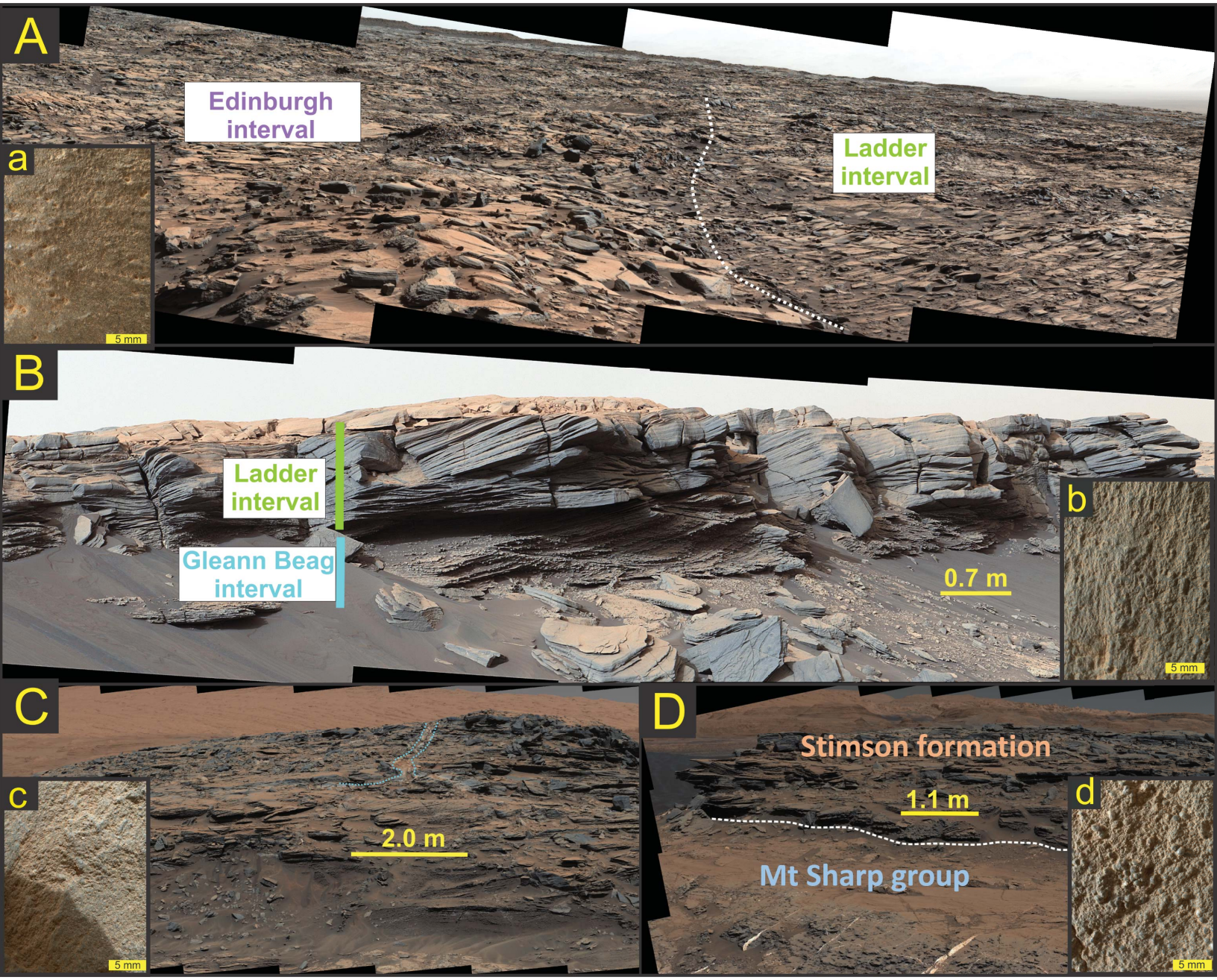
A
Edinburgh interval
Ladder interval
a
5 mm
B
Ladder interval
Gleann Beag interval
0.7 m
b
5 mm
C
2.0 m
c
5 mm
D
Stimson formation
1.1 m
Mt Sharp group
d
5 mm

Figure 4.

	Emerson plateau	Naukluft plateau	Greenheugh
Concretions	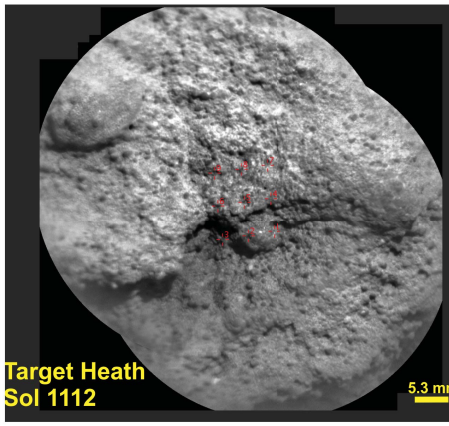		
Veins	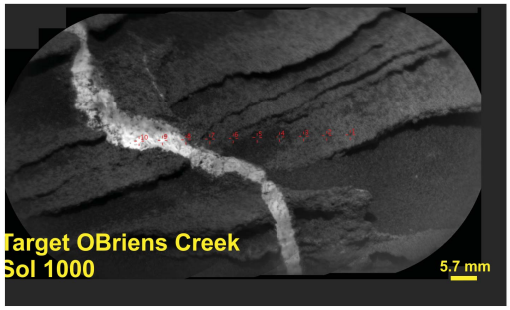	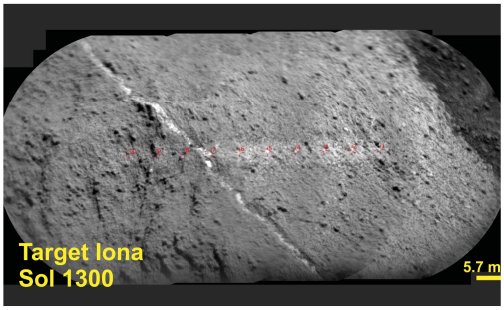	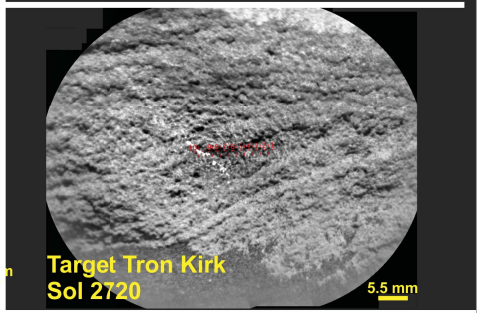
Halos	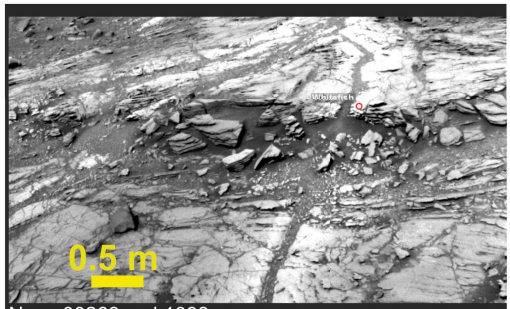 Ncam00263, sol 1093	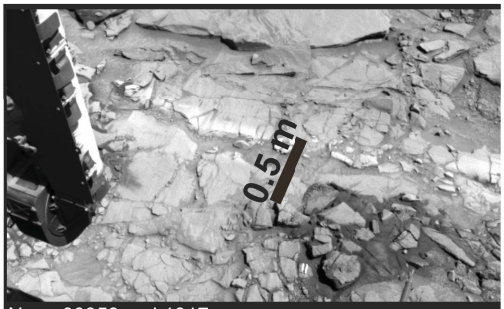 Ncam00353, sol 1317	No halos detected

Figure 5.

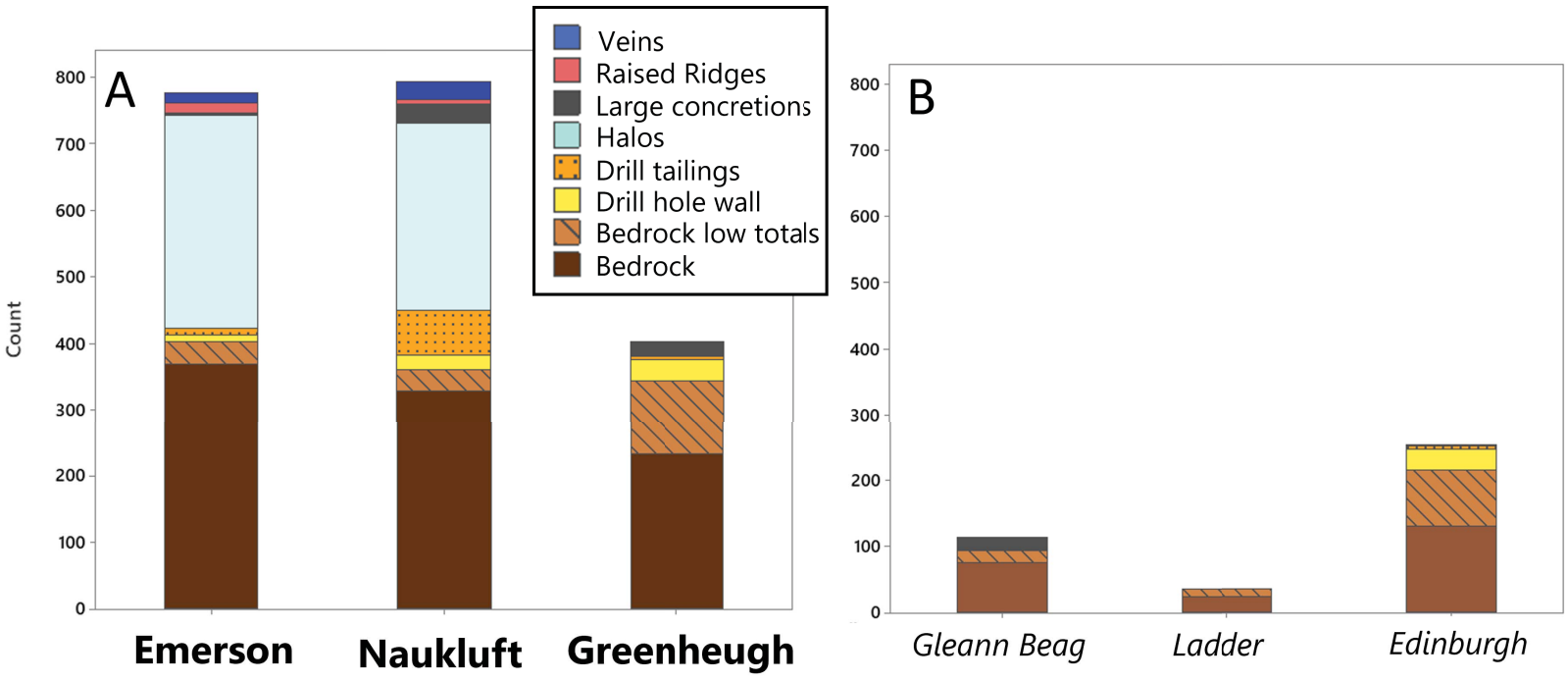
A
B
Count
800
700
600
500
400
300
200
100
0
Veins
Raised Ridges
Large concretions
Halos
Drill tailings
Drill hole wall
Bedrock low totals
Bedrock
Emerson
Naukluft
Greenheugh
Gleann Beag
Ladder
Edinburgh

Figure 6.

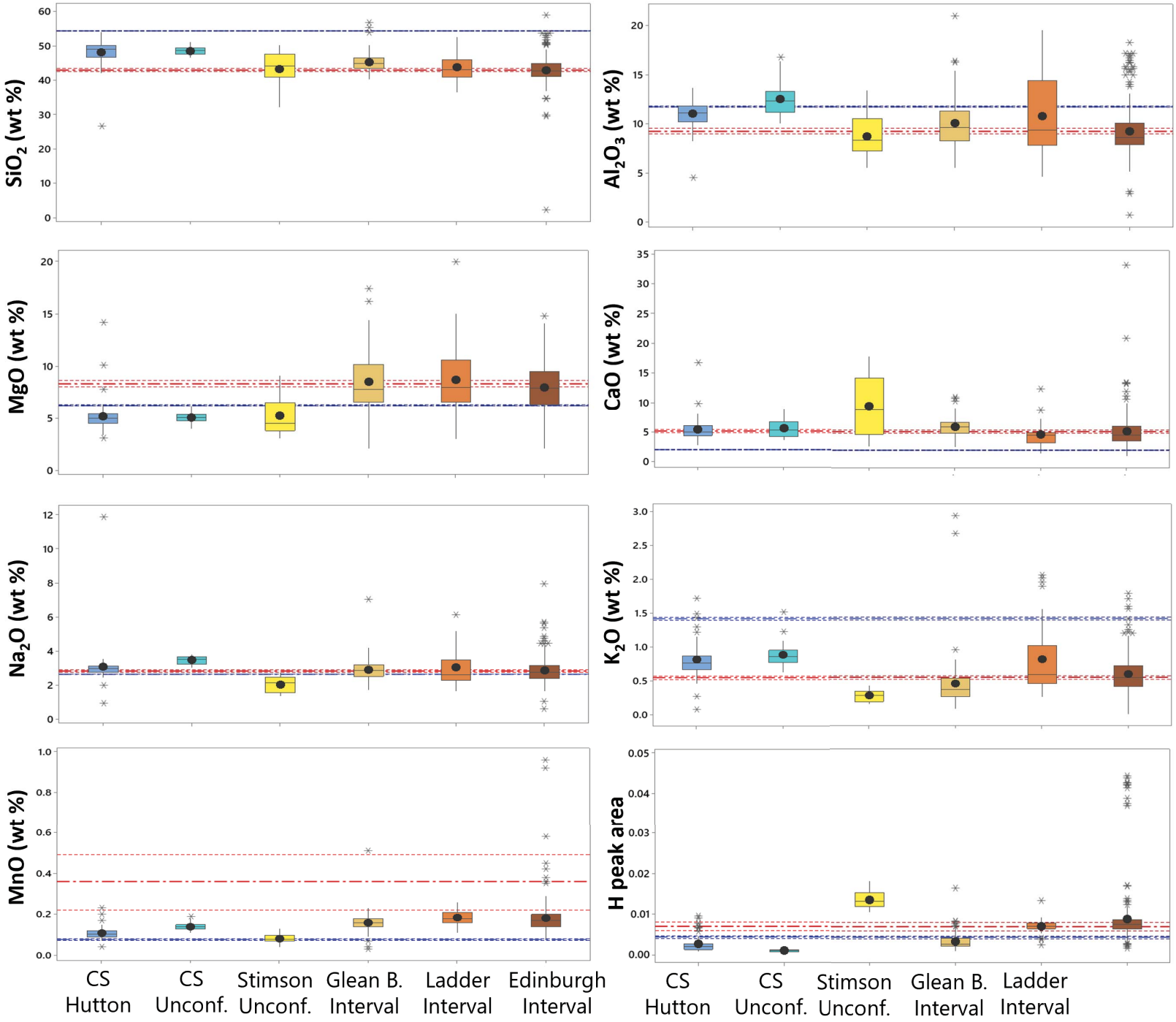
SiO2 (wt %)
Al2O3 (wt %)
MgO (wt %)
CaO (wt %)
Na2O (wt %)
K2O (wt %)
MnO (wt %)
H peak area
CS Hutton
CS Unconf.
Stimson Unconf.
Glean B. Interval
Ladder Interval
Edinburgh Interval

Figure 7.

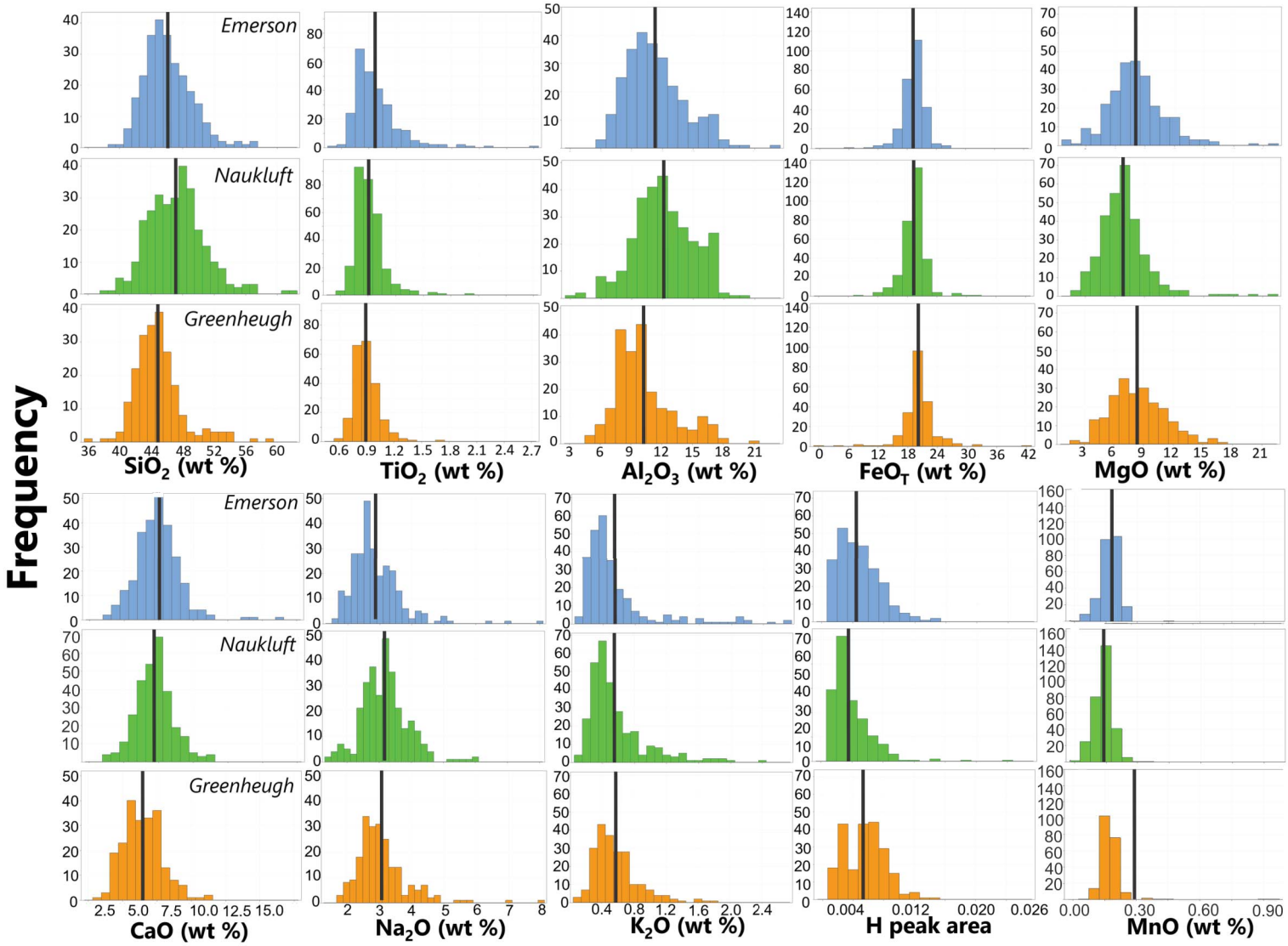
Frequency
Emerson
Naukluft
Greenheugh
SiO2 (wt %)
TiO2 (wt %)
Al2O3 (wt %)
FeOT (wt %)
MgO (wt %)
CaO (wt %)
Na2O (wt %)
K2O (wt %)
H peak area
MnO (wt %)

Figure 8.

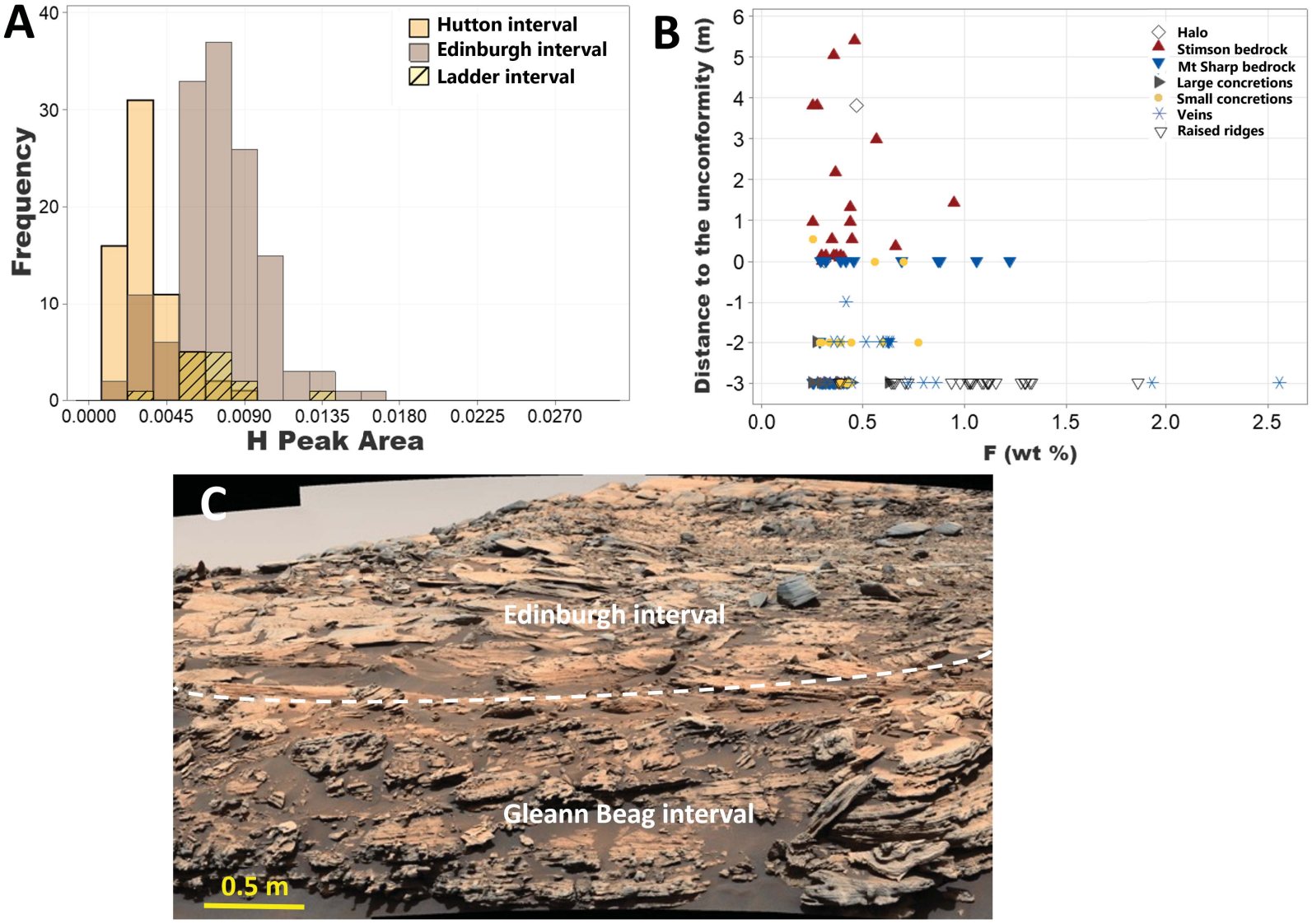
A
Hutton interval
Edinburgh interval
Ladder interval
Frequency
H Peak Area
B
Halo
Stimson bedrock
Mt Sharp bedrock
Large concretions
Small concretions
Veins
Raised ridges
Distance to the unconformity (m)
F (wt %)
C
Edinburgh interval
Gleann Beag interval
0.5 m

Figure 9.

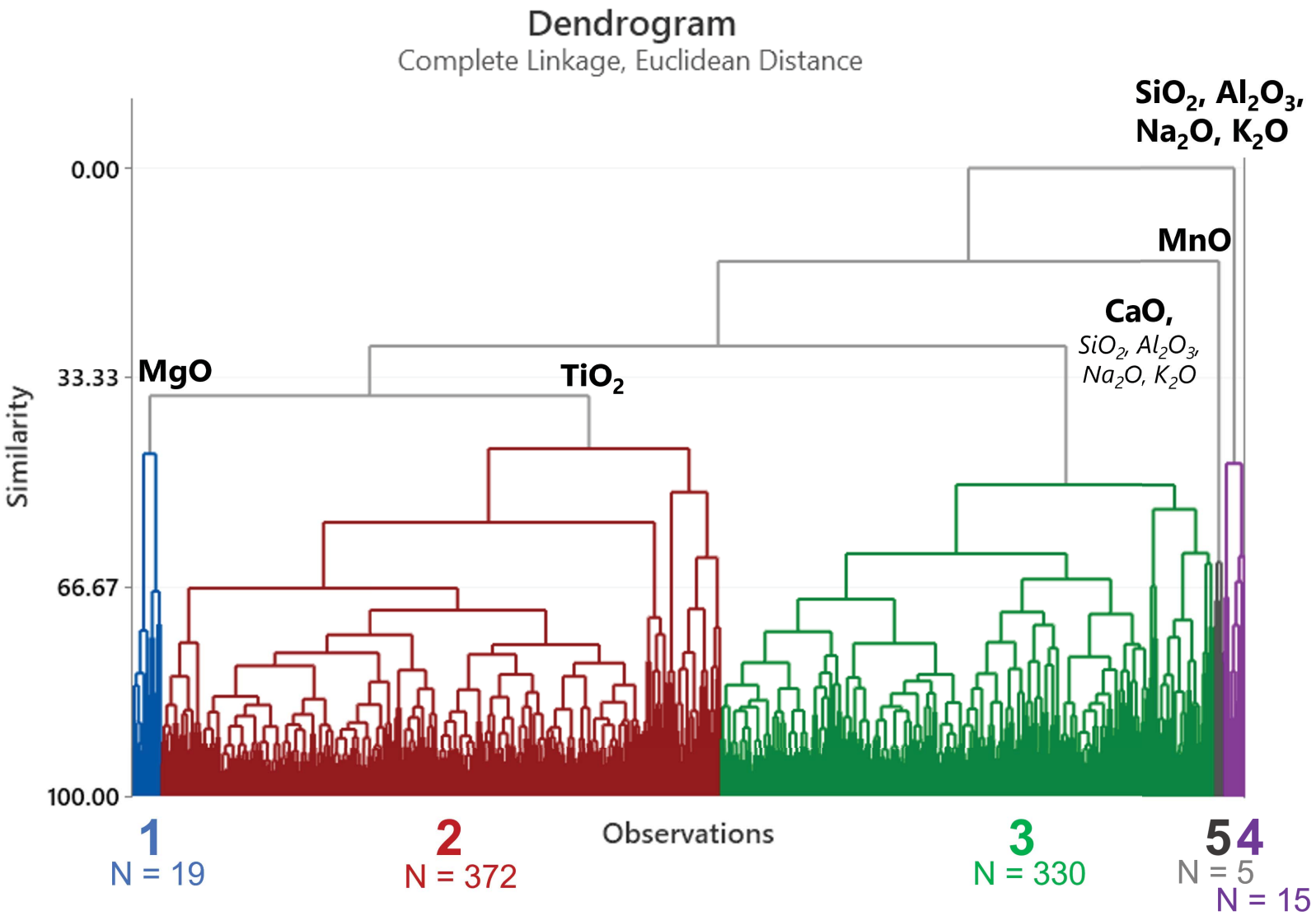
Dendrogram
Complete Linkage, Euclidean Distance
SiO_2, Al_2O_3, Na_2O, K_2O
MnO
CaO,
SiO_2, Al_2O_3, Na_2O, K_2O
MgO
TiO_2
0.00
33.33
66.67
100.00
Similarity
1
N = 19
2
N = 372
Observations
3
N = 330
5 4
N = 5
N = 15

Figure 10.

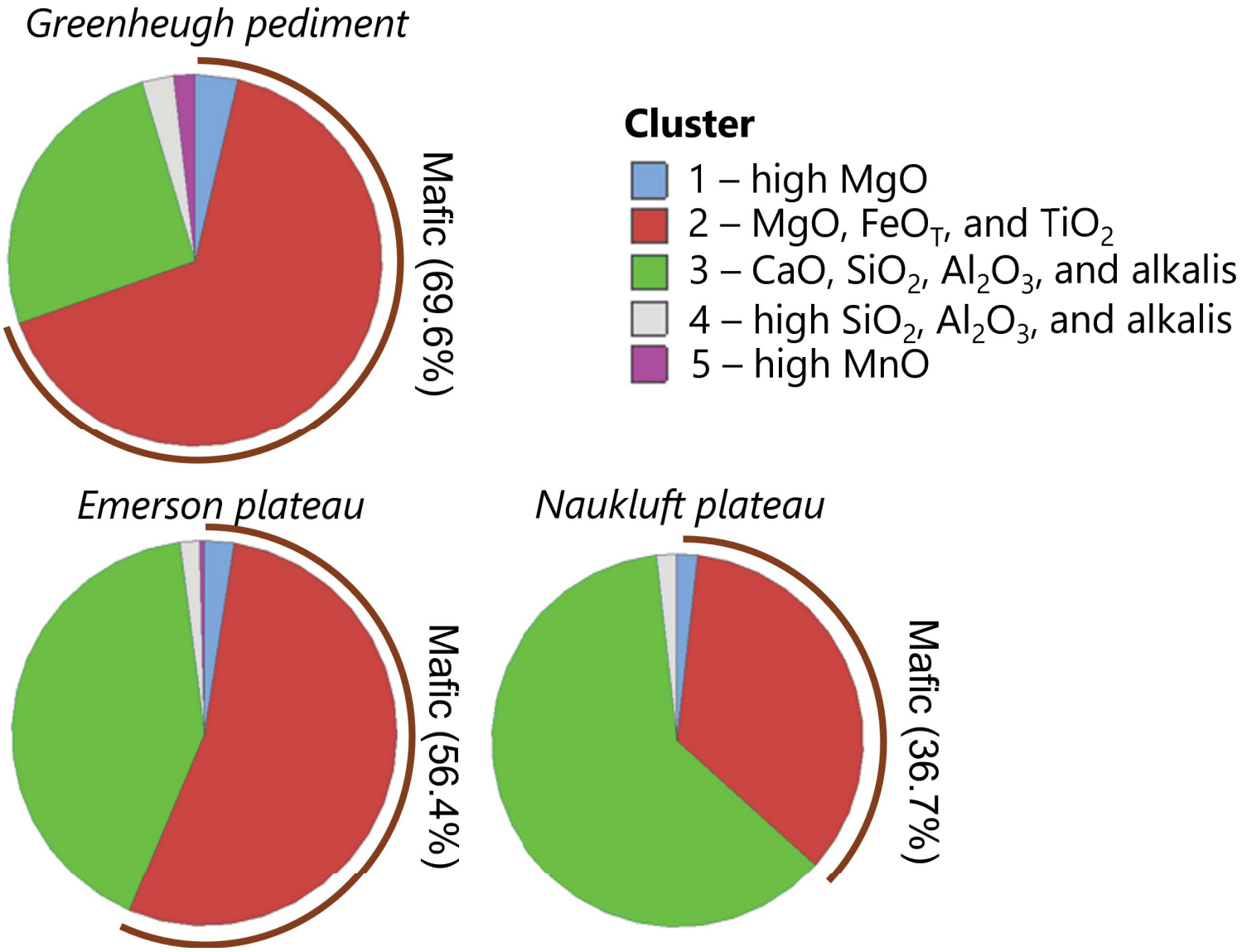
Greenheugh pediment
Mafic (69.6%)
Cluster
1 – high MgO
2 – MgO, FeO$_T$, and TiO$_2$
3 – CaO, SiO$_2$, Al$_2$O$_3$, and alkalis
4 – high SiO$_2$, Al$_2$O$_3$, and alkalis
5 – high MnO
Emerson plateau
Mafic (56.4%)
Naukluft plateau
Mafic (36.7%)

Figure 11.

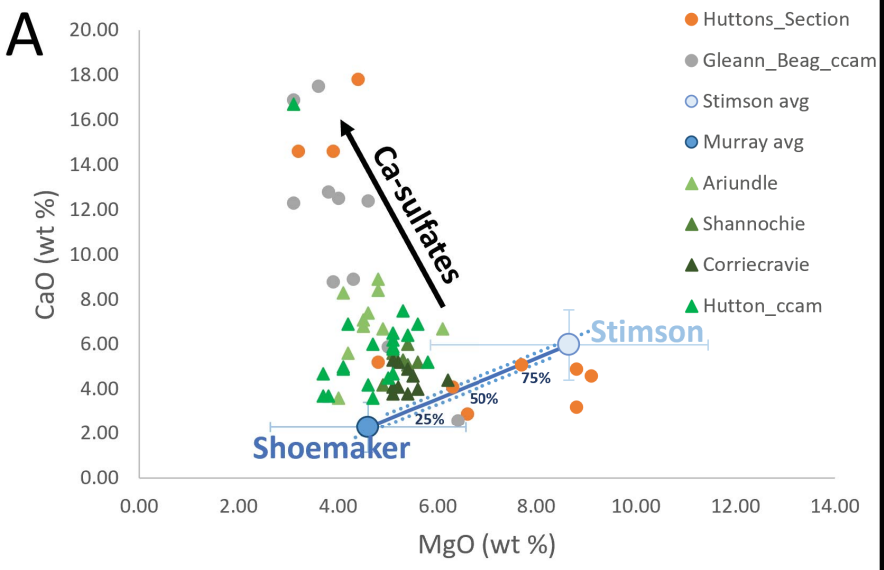
A
CaO (wt %)
MgO (wt %)
Huttons_Section
Gleann_Beag_ccam
Stimson avg
Murray avg
Ariundle
Shannochie
Corriecravie
Hutton_ccam
Ca-sulfates
Stimson
Shoemaker
25%
50%
75%

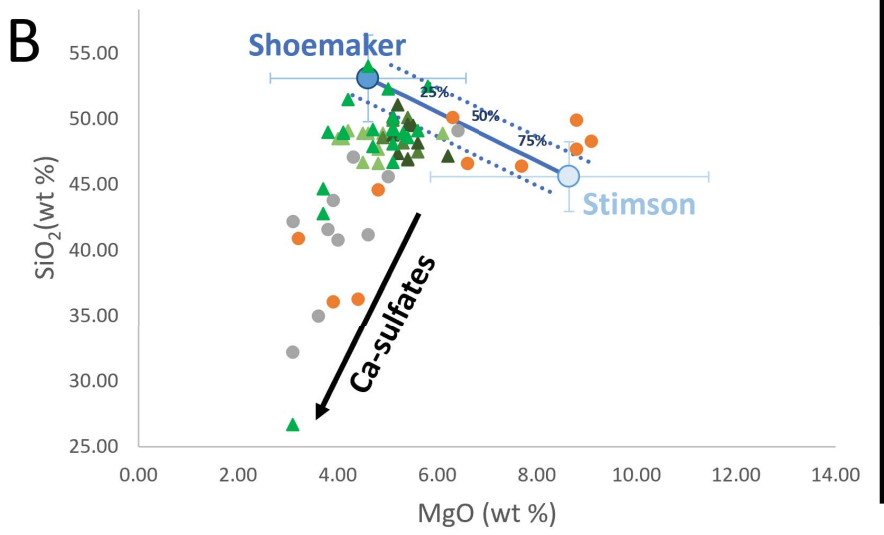
B
SiO2(wt %)
MgO (wt %)
Shoemaker
Stimson
25%
50%
75%
Ca-sulfates

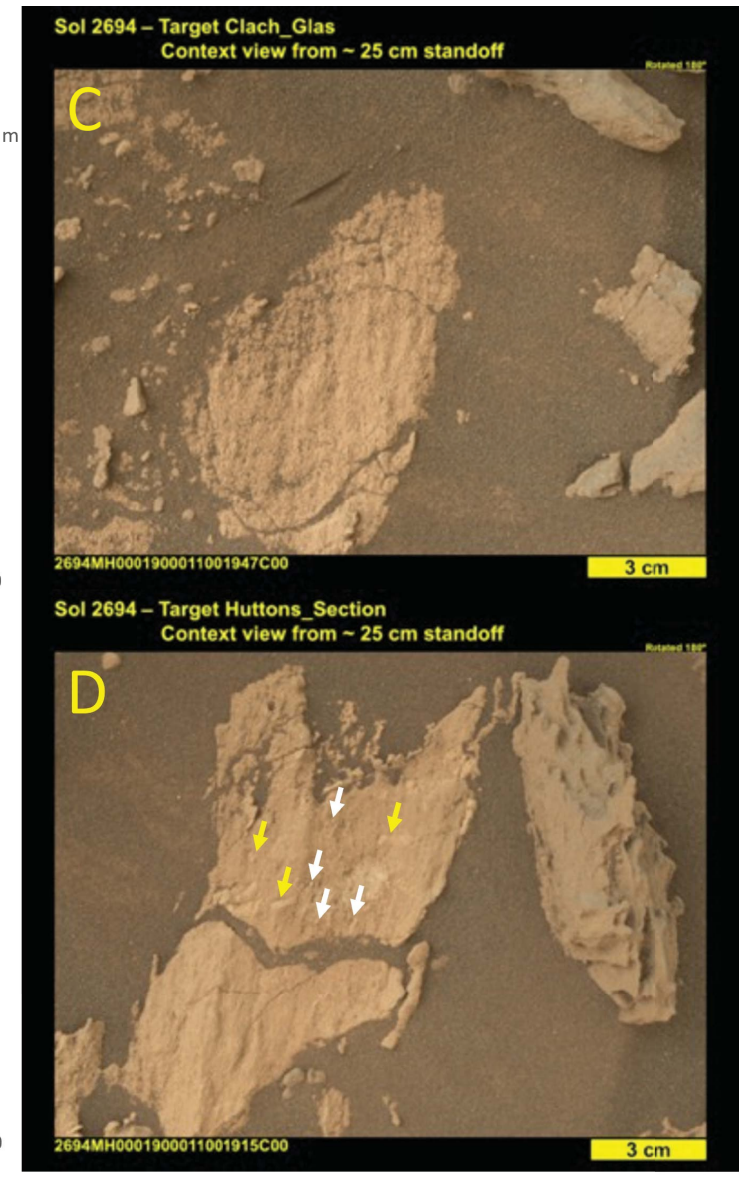
Sol 2694 – Target Clach_Glas
Context view from ~ 25 cm standoff
C
2694MH0001900011001947C00
3 cm
Sol 2694 – Target Huttons_Section
Context view from ~ 25 cm standoff
D
2694MH0001900011001915C00
3 cm

Figure 12.

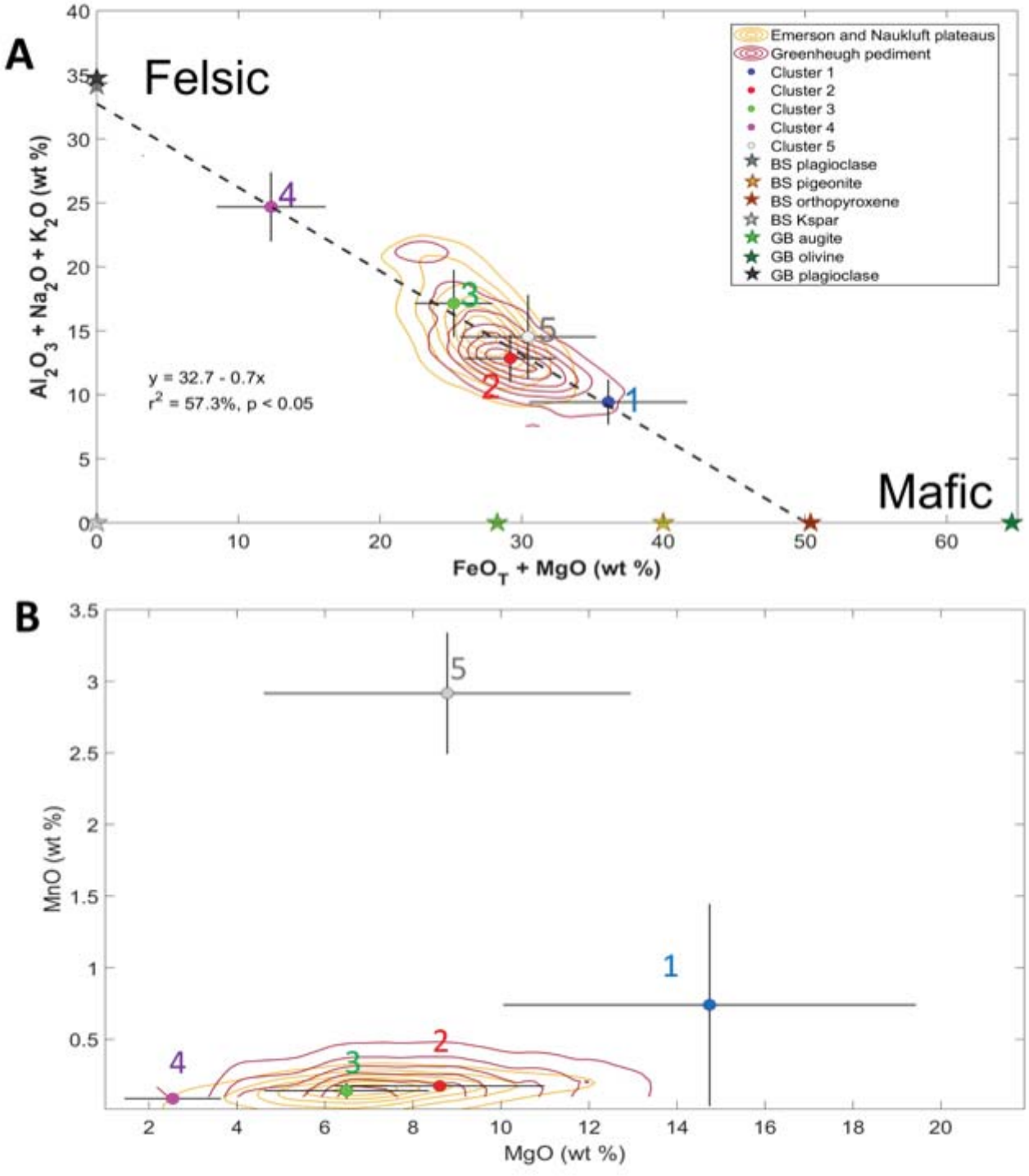
A
Felsic
Mafic
Emerson and Naukluft plateaus
Greenheugh pediment
Cluster 1
Cluster 2
Cluster 3
Cluster 4
Cluster 5
BS plagioclase
BS pigeonite
BS orthopyroxene
BS Kspar
GB augite
GB olivine
GB plagioclase
y = 32.7 - 0.7x
r² = 57.3%, p < 0.05
Al2O3 + Na2O + K2O (wt %)
FeOT + MgO (wt %)
B
MnO (wt %)
MgO (wt %)

Figure 13.

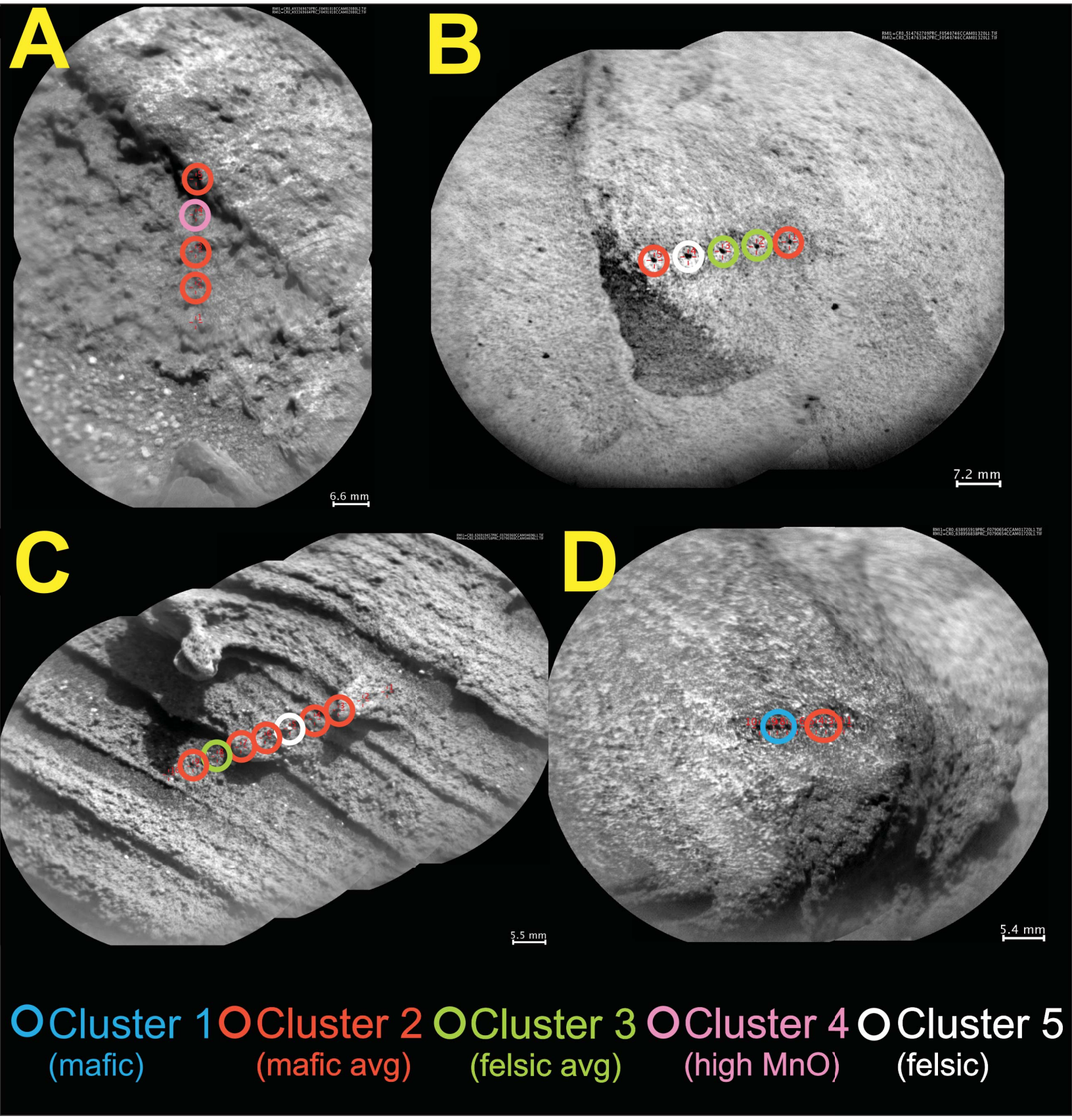
A
B
C
D
6.6 mm
7.2 mm
5.5 mm
5.4 mm
Cluster 1
(mafic)
Cluster 2
(mafic avg)
Cluster 3
(felsic avg)
Cluster 4
(high MnO)
Cluster 5
(felsic)

Figure 14.

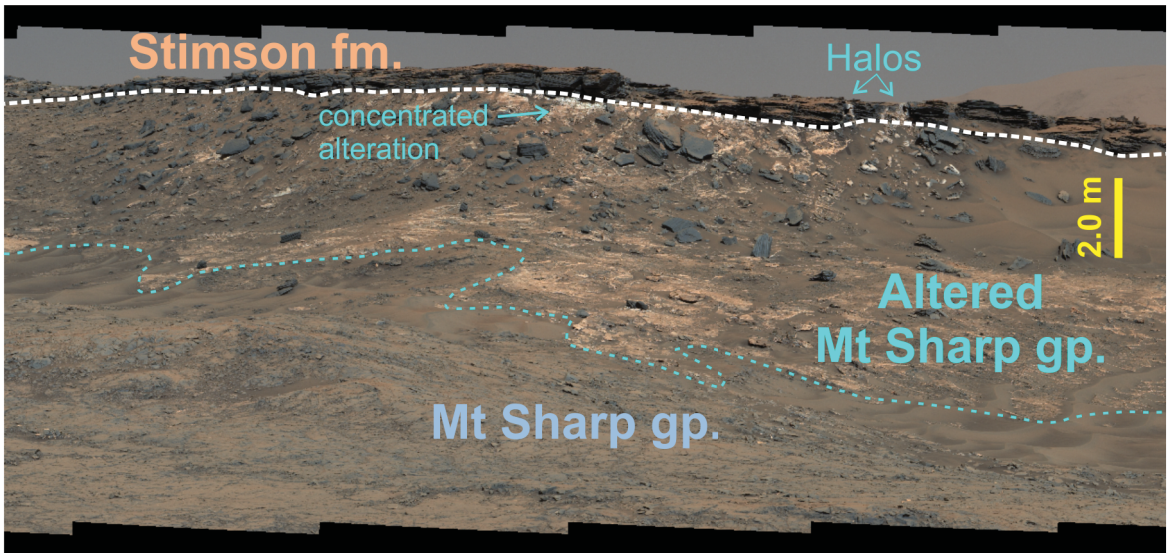
Stimson fm.
Halos
concentrated
alteration
2.0 m
Altered
Mt Sharp gp.
Mt Sharp gp.

Variables	Locality	90-105 wt% totals					
		Mean	SE Mean	StDev	Min	Med	Max
SiO_2	Emerson	46. 1	0.2	3.0	38.9	45.6	57.1
	Naukluft	47.2	0.2	3.6	37.6	47.3	61.7
	Greenheugh	44.9	0.2	3.1	35.6	44.5	59.0
TiO_2	Emerson	1.0	0.0	0.3	0.5	0.9	2.7
	Naukluft	0.9	0.0	0.2	0.6	0.9	2.0
	Greenheugh	0.9	0.0	0.1	0.6	0.9	1.7
Al_2O_3	Emerson	11.3	0.2	2.9	5.7	10.8	22.5
	Naukluft	12.1	0.2	2.9	3.3	12.0	19.6
	Greenheugh	10.3	0.2	2.9	4.6	9.6	21.0
FeO_T	Emerson	19.2	0.1	2.3	6.6	19.5	26.0
	Naukluft	19.3	0.1	2.4	7.8	19.4	32.1
	Greenheugh	20.12	0.3	3.7	0.9	20.3	41.2
MgO	Emerson	8.1	0.2	2.9	0.9	7.7	21.6
	Naukluft	6.8	0.2	2.5	2.0	6.7	22.0
	Greenheugh	8.4	0.2	2.8	2.1	8.1	17.4
CaO	Emerson	6.2	0.1	2.0	1.6	6.2	17.2
	Naukluft	6.0	0.1	1.7	1.5	6.0	11.5
	Greenheugh	5.0	0.1	1.8	1.0	4.9	11.1
Na_2O	Emerson	2.9	0.1	0.8	1.5	2.7	8.1
	Naukluft	3.8	0.0	0.7	1.5	3.2	6.0
	Greenheugh	3.1	0.1	0.8	1.7	2.9	8.0
K_2O	Emerson	0.6	0.0	0.5	0.1	0.4	2.7
	Naukluft	0.6	0.0	0.4	0.1	0.4	2.4
	Greenheugh	0.6	0.0	0.3	0.1	0.5	1.8
MnO	Emerson	0.2	0.0	0.2	0.0	0.2	2.6

	Naukluft	0.1	0.0	0.1	0.0	0.1	0.3
	Greenheugh	0.3	0.0	0.6	0.1	0.2	5.5
Sum of Oxides	Emerson	95.4	0.2	3.5	90.0	95.1	104.2
	Naukluft	96.1	0.2	3.6	90.0	95.6	104.8
	Greenheugh	93.5	0.2	2.8	90.0	92.8	102.2

Cluster	SiO_2	+/-	std	TiO_2	+/-	Std	Al_2O_3	+/-	std	FeO_T	+/-	std	MgO	+/-	std	CaO	+/-	std	Na_2O	+/-	std	K_2O	+/-	std	MnO	+/-	std
1	43.9	0.7	2.8	0.8	0.0	0.1	6.9	0.4	1.7	21.4	0.7	3.0	14.7	1.1	4.7	3.6	0.4	1.6	2.3	0.1	0.6	0.3	0.1	0.2	0.7	0.2	0.7
2	43.9	0.1	1.8	1.0	0.0	0.2	9.7	0.1	1.8	20.6	0.1	2.1	8.6	0.1	2.4	5.6	0.1	1.8	2.7	0.0	0.4	0.4	0.0	0.2	0.2	0.0	0.0
3	48.5	0.2	2.8	0.9	0.0	0.2	13.1	0.1	2.5	18.7	0.1	2.0	6.5	0.1	1.9	6.0	0.1	1.8	3.4	0.0	0.7	0.7	0.0	0.4	0.1	0.0	0.1
4	54.5	0.8	3.2	0.9	0.1	0.2	18.0	0.6	2.4	9.8	1.0	3.7	2.5	0.3	1.1	5.7	0.7	2.6	5.7	0.3	1.3	1.0	0.2	0.6	0.1	0.0	0.0
5	42.8	1.2	2.6	0.8	0.0	0.1	10.3	1.4	3.2	21.7	1.1	2.4	8.8	1.9	4.2	4.0	0.9	2.0	3.3	0.3	0.7	1.0	0.3	0.6	2.9	0.2	0.4